DYNAMICS OF BRANCHED POLYMERS STUDIED WITH MD SIMULATIONS AND NEUTRON SCATTERING

STEFAN HOLLER

SIGILL: UNIVERSITAT: LUDOVIC: MAXIM:

München 2018

DYNAMIK VON VERZWEIGTEN POLYMEREN UNTERSUCHT MITTELS MD SIMULATIONEN UND NEUTRONENSTREUUNG

2018

Dissertation
an der Fakultät für Physik
der Ludwig-Maximulian-Universität
München

vorgelegt von
Stefan Holler
aus Regensburg

München, den 21.03.2018

Erster Gutachter: Prof. Dr. Joachim Rädler
Zweiter Gutachter: Prof. Dr. Dieter Richter
Tag der Mündlichen Prüfung: 18.06.2018

ZUSAMMENFASSUNG

Die vorliegende Arbeit ist eine Untersuchung des Einflusses von Anzahl und Länge von Armen auf die Dynamik von symmetrischen und asymmetrischen Polymersternen. Das Hauptaugenmerk liegt dabei auf der Beweglichkeit des Verzweigungspunktes der jeweiligen Sterne. Die vorwiegend verwendeten Methoden sind die computergestützte Molekulardynamik Simulation (MD) und die Neutronen Spin Echo Spektroskopie (NSE). In den Experimenten wurden symmetrische 3- und 4-Arm Polymer (Polyethylen) Sterne mit zwei verschiedenen Längen verwendet. Des weiteren wurden asymmetrische Sterne unterschiedlicher Länge mit einem kurzen unverschlauften (unentangled) Seitenarm untersucht. In den Simulationen wurde ein einfaches Kugel - Feder Modell unter Ausschluss von Kettenüberkreuzung verwendet um 3-, 4- und 5-Arm symmetrische sowie asymmetrische Sterne mit variabler Länge des kurzen Seitenarms zu modellieren. Indem die jeweiligen Armenden an Ihrer Position festgehalten wurden konnten Sterne simuliert werden, die die Eigenschaften von sehr langen Ketten teilen. Zum Kombination der beiden Methoden und zur Untersuchung der Dynamik wurden der dynamische Strukturfaktor der zentral markierten Polymere aus Simulation und Experiment verglichen, dies wurde getan um die Abhängigkeit der Dynamik von der Anzahl der Sternarme zu untersuchen. Um diese Abhängigkeit zu bestätigen und um den Beitrag zur Reibung des kurzen Seitenarms bei asymmetrischen Sternen zu ermitteln wurde die jeweilige mittlere quadratische Verschiebung (mean square displacement MSD) der Verzweigungspunte analysiert. Des weiteren wurden Rheologie Messungen durchgeführt um die Dynamik in einem größeren Zeitfenster zu untersuchen. Der Beitrag der dynamischen Röhrenerweiterung (dynamic tube dilation DTD) zur Beweglichkeit des Verzweigungspunktes wurde erforscht und eine starke Abhängigkeit von der Anzahl der Sternarme festgestellt die durch das aktuelle Modell der DTD nicht vollständig zu erklären ist. Simulationen und experimentelle Messungen zeigten übereinstimmend dass mit einer größeren Anzahl an Seitenarmen in den Sternen die Mobilität des Verzweigungspunktes zunehmend eingeschränkt wird.

ABSTRACT

The present work is an investigation of the influence of number of arms and length on the dynamics in symmetric and asymmetric polymer stars. The main focus lies on the dynamics of the branch point of each star. The main techniques used are molecular dynamics (MD) simulations and neutron spin echo spectroscopy (NSE). The experimentally studied stars were 3- and 4-arm polymer (polyethylene) symmetric stars of two different lengths and asymmetric stars with one short unentangled side arm. The simulations performed used a simple bead-spring model without chain crossing to model 3- 4- and 5-arm symmetric and asymmetric stars with variable short side arm lengths. By fixing the arm ends of the symmetric stars in place the equivalent of very large star was modeled. The dynamic structure factors of the specifically center labeled polymer stars from simulations and experiments were compared to elucidate the functionality dependence of the dynamics of star polymers. A mean square displacement analysis was performed to confirm the supposed functionality dependence and the side arm friction contribution. Rheological measurements were conducted to obtain a wide time scale analysis of the polymers. The contribution of dynamic tube dilation (DTD) to the mobility of the star branch points was investigated and a strong functionality dependence was determined, which was not explained by the current DTD model. The branch point mobility showed a strong increase in confinement for higher arm counts which was found with good agreement between simulations and experiments.

CONTENTS

1

INTRODUCTION

Plastic is one of the most ubiquitous materials that we interact with every day. It is to varying degree part of almost every item we use, from the chairs we sit on, to the clothing we wear, to the cars we drive. All these materials have different characteristics, but one thing they have in common is that they are composed of polymers. The individual properties of the materials are not only defined by the type of material but also by the geometric structure of the polymer chains. One of the biggest factors is the length of these chains. However, changing the structure from a linear to a branched one with additional arms in e.g. a star-like structure can result in even bigger changes to the material properties. To understand the dynamics of these materials on a molecular level depending on their geometries is important not only from the standpoint of basic research but also because most manufacturing methods of plastic are performed with the materials in their molten state, where they undergo the different states of rheological behavior, such as Rouse-like behavior and rubbery and viscous behavior.

Polymer dynamics have been studied for decades [1, 2, 3, 4] and the tube model has become the standard approach for describing linear chains. These chains experience topological constraints by the mutual entanglements, as the chains are physically not able to cross each other. This confinement can be described by an effective tube for a given chain which makes movement only possible along the contour length or primitive path of the chain in a one-dimensional repational movement.

Introducing a change in geometry by adding even a single side-branch changes their rheological behavior drastically [5, 6, 7] as any branch completely suppresses reptational movement along the tube. This strongly slows down the dynamics of the polymer chain. In the case of stars with multiple arms, this effect is even stronger and theories as for linear chains are no longer applicable. One of the reasons for this is that stars cannot reptate as opposed to their linear counterparts. Several aspects of these structures have been investigated in the past [8, 9, 10], like the viscosity increase of stars going to high numbers of arms [11] or the influence on particle size, shape and radius of gyration of different topologies [12]. These studies bring us closer to understanding the behavior of branched systems.

One aspect in the studies of branched polymer systems is to understand and quantify the behavior of the branch point (BP) itself on a molecular length scale as it should show the largest reaction to the different geometries, as the characteristics might not always correlate to changes in the macroscopic behavior. This use of several complementary techniques to study the same materials helps to form a better understanding.

This work combines numerical simulations with several experimental techniques. It is possible to perform molecular dynamics simulations of polymers that would be highly difficult to synthesize. The simulations also give the opportunity to create direct visualization of the branch point movement as seen in Figure 1, which allow the direct observation of changes to the BP mobility.

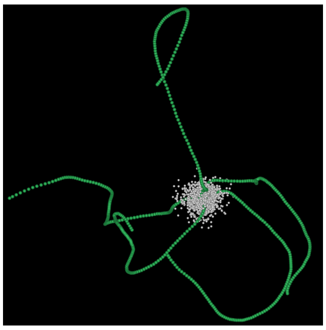

Figure 1: Green lines are typical mean paths of a 5-arm-star for fixed arm ends. The cloud of points represent the positions of the branch points at different simulation times.

Neutron spin echo (NSE) spectroscopy, combined with a labeling technique unique to neutron scattering, makes it possible to extract the motion of the polymer branch point experimentally and compare it to the calculations from the simulation and theoretical model. Rheological measurements add a macroscopic overview and a much wider range of timescales. Polyethylene and its parent polymer polybutadiene are polymers with simple chemical structure where branching can be introduced and are therefore used in the different experiments.

To describe the relaxation process and BP movement of branched polymers several models expanding the standard tube model are used. In branched the relaxation of the individual arms have to happen hierarchically, meaning that first the outer parts of the polymer have to relaxe before the inner parts have the possibility to. Other models are the branch point hopping [13, 14, 15] where short side arms act as additional firciton for asymmetric systems. To describe the movement of symmetric polymer star systems the model of Vilgis and Boué for polymer networks was adopted and modified [16]. This was by including the influenced of constraint-release mechanisms such as dynamic tube dilution[17, 18] into the model.

The work contains a systematic study for symmetric stars investigating the influence of functionality, meaning the number of arms and the arm length on the mobility of the branch point as well as the range of the influence of these branch points on individual star arms. Parts of the shown results have been already published but the author of this work Stefan Holler *et al.* [19]. Reprinted with permission from:

Stefan Holler, Angel J Moreno, Michaela Zamponi, Petra Bacová, Lutz Willner, Hermis Iatrou, Peter Falus, and Dieter Richter. The role of the functionality in the branch point motion in symmetric star polymers: A combined study by simulations and neutron spin echo. *Macromolecules*, 51(1):242–253, 2018. URL: `https://doi.org/10.1021/acs.macromol.7b01579`, `doi:10.1021/acs.macromol.7b01579`. Copyright 2018 American Chemical Society.

Furthermore a investigation on the influence of very short unentangled side chains on the dynamics of asymmetric stars has been performed, also investigating the dependence on backbone length. The methods include neutron spin echo spectroscopy, small angle neutron scattering, rheology and several molecular dynamics simulations of the complex systems.

Chapter 2 introduces the established models needed to describe polymers from their static characteristics to Rouse theory and dynamic tube dilution. Chapter 3 describes the different experimental methods and the basics of neutron scattering and rheology as well as the polymer synthesis and sample preparation used in this work. The details of the bead-spring simulation are described in Chapter 4 including a description of all simulated systems. The results of NSE and MD simulations for the symmetric stars are discussed in Chapter 5. Chapter 6 deals with the results of the studies on the asymmetric stars. All the most important conclusions are summarized in Chapter 7.

2

POLYMER THEORY

Polymers are defined as chains that are constructed out of a large number of the same individual part or monomer. They can have many different geometrical forms, from simple linear chains of various lengths to complex stars, H-polymers, combs or trees, as well as connected networks. These materials are commonly known as plastics and are usually defined by their macroscopic properties, such as hardness, strength, density and flexibility. Their properties are dependent on their chemical composition as well as on their static and dynamic microscopic behavior. This influences their production and how they can be processed. In the following section the standard theoretical models to describe the static and dynamic behavior for linear and branched polymers are introduced.

2.1 STATIC POLYMER PROPERTIES

The static characteristics of polymers can be described by using a statistical approach. The simplest model to describe a linear chain is the "random walk", where the chain consists of N segments of length l that are positioned at $\vec{R}_n$ with $n = 1, ..., N$. In the classical random walk model there is no restriction on the angle between neighboring segments. The end-to-end distance of a chain $\vec{R}_E = \vec{R}_N - \vec{R}_1$ is the distance between the end segments. This is equal to the sum of all connecting vectors $\vec{r}_n$ between the neighboring segments. The median chain distance of the random walk is $\langle\vec{R}_E\rangle = \sum_{n=1}^{N} \vec{r}_n = 0$. The mean quadratic chain end-to-end distance is used to describe the chain size

$$R_E^2 = \langle\vec{R}_E^2\rangle = \sum_{i,j=1}^{N} \langle\vec{r}_i \cdot \vec{r}_j\rangle = \sum_{i=1}^{N} \langle\vec{r}_i^2\rangle + \sum_{i\neq j}^{N} \langle\vec{r}_i \cdot \vec{r}_j\rangle. \tag{2.1}$$

Without any correlations between different segments this becomes

$$R_E^2 = Nl^2 \tag{2.2}$$

for the simplest possible chain model. As for more realistic polymers there is a dependence on the bond vector between neighboring segments, which is dependent on the chemical composition of the chain and its monomers. Hence, the proportionality constant C_∞ is introduced, which increases the end-to-end distance, which is a measure for the stiffness of a polymer. This factor can be included in the effective temperature dependent bond-length as $l^2 = C_\infty l_0^2$, which the chemical bond-length l_0 ($l_0 = 1.54$ Å for carbon-carbon bond) and the chain length becomes $R_E^2 = Nl^2$ with N the number of segments of length l. Another value that is commonly used to describe the magnitude of polymer chains is the radius of gyration, R_g. It is the mean square displacement of the chain segment from the center of mass of the chain.

$$R_g^2 = \langle \vec{R}_g^2 \rangle = \frac{1}{N} \sum_{n=1}^{N} \langle (\vec{R}_n - \vec{R}_{cm})^2 \rangle, \tag{2.3}$$

where $\vec{R}_{cm} = \frac{1}{N} \sum_{n=1}^{N} \vec{R}_n$ is the center of mass position. The segment to segment mean square distance for a random walk is for large N

$$\langle (\vec{R}_n - \vec{R}_m)^2 \rangle = |n - m| l^2, \tag{2.4}$$

which results in the following relationship for the radius of gyration

$$R_g^2 = \frac{1}{6} N l^2 = \frac{1}{6} R_E^2. \tag{2.5}$$

This however does not include assumptions like the exclusion of chain crossing but still offers a very good estimate for chains even without excluded volume.

A different way to calculate the segment length is by using the relation between radius of gyration R_g and the mean-square radius of gyration $< R^2 >_0 /M$ [20], with $\frac{<R_0^2>}{M} = \frac{6R_g^2}{m_0 \cdot N}$ and $R_g^2 = \frac{N \cdot l^2}{6}$. For this one needs the $\frac{<R_0^2>}{M}$ from literature and it has slightly different results for the segment length. Which one of the two different methods is the better description is still being debated.

2.1.1 *Static structure factor and random phase approximation*

The theoretical description of (small angle) neutron scattering (SANS) experiments from polymer melts consisting of labelled chains (co-polymers) can be achieved using the static structure factor $S(q)$ which is defined as

$$S(\vec{q}) = \frac{1}{N} \sum_{n,m=1}^{N} \langle e^{i\vec{q}(\vec{R}_n - \vec{R}_m)} \rangle, \tag{2.6}$$

with $\vec{q} = \vec{k} - \vec{k}'$ the scattering vector between the wavevector, before and after the scattering, it gives information about the structure in the investigated system. Using the information about the Gaussian chain statistics, the static structure factor can be calculated as

$$\begin{aligned} S(\vec{q}) &= \frac{1}{N} \sum_{n,m=1}^{N} e^{\langle -\frac{1}{2} \left(\vec{q}(\vec{R}_n - \vec{R}_m) \right)^2 \rangle} \\ &= \frac{1}{N} \sum_{n,m=1}^{N} e^{\langle -\frac{1}{6} \vec{q}^2 (\vec{R}_n - \vec{R}_m)^2 \rangle} \\ &= \frac{1}{N} \sum_{n,m=1}^{N} e^{-\frac{1}{6} q^2 l^2 |n-m|} = S(q). \end{aligned}$$

The structure factor contains all inter-particle correlations and reveals information about the structure. Going from this discrete representation to continuous variables the Debye-function is obtained

$$S(q) = \frac{1}{N}\int_0^N dn \int_0^N dm e^{-\frac{1}{6}q^2 l^2 |n-m|} = ND(q^2R_g^2). \tag{2.7}$$

If N is large the Debye function is

$$D(u) = \frac{2}{u^2}(e^{-u} - 1 + u) \tag{2.8}$$

with $u = q^2R_g^2$ and in a good approximation the static structure factor can be written as

$$S(q) = \frac{N}{q^2R_g^2 + 1}. \tag{2.9}$$

The Random Phase Approximation (RPA) [21, 22] is a way to theoretically calculate the static structure factor for partly labeled polymer chains and is a useful tool to interpret the scattering results of polymer networks [23, 24] and melts [25, 26]. A polymer melt consisting of two different monomer types (A and B) represents the labeled (protonated) and unlabeled (deuterated) polymer sections in the NSE and SANS experiments. The correlation functions without any interactions are given as

$$S_0^{AB}(q) = n_c s_0^{AB}(q) = \left\langle \sum_{l\in A} \sum_{l'\in B} \exp\left(i\vec{q}\cdot(\vec{r}_l - \vec{r}_{l'})\right) \right\rangle_0, \tag{2.10}$$

with n_c the total number of chains and s_0^{XX} the structure factor of a single chain. The total structure factor for a melt consistent of two component chains, as in the neutron scattering experiments, is given as

$$S^{tot}(q) = \frac{S_0^{AA}S_0^{BB} - (S_0^{AB})^2}{S_0^{AA} + S_0^{BB} + 2S_0^{AB}}. \tag{2.11}$$

The method by Read [27] for arbitrary geometries is used to calculate the static structure factor for the symmetric and asymmetric stars. The exact form of the correlators S_0^{XX} in eq. 2.11, as well as the origin of the form of the equation, are given in more detail in the Appendix A.1.

2.2 DYNAMICS OF LINEAR POLYMERS

The main focus of this work is the dynamics of polymers, which makes it important to understand some of the basic models that are used to describe the dynamic behavior of the investigated systems.

2.2.1 *Rouse Theory*

In the Rouse model [1, 28] a polymer chain is described by using beads that are connected with springs in a heat bath with a spring constant of $k = \frac{3k_B T}{l^2}$, where k_B is the Boltzmann constant, T is the temperature and l is the segment length. The equations of motion of the beads are described by the Langevin equations for the n-th bead at position $\vec{R}_n(t)$

$$\zeta_0 \frac{\partial \vec{R}_n(t)}{\partial t} = k \frac{\partial^2 \vec{R}_n(t)}{\partial n^2} + \vec{g}_n(t). \tag{2.12}$$

The boundary conditions on the ends of the chain are $\frac{\partial \vec{R}_n}{\partial n} = 0$ which represents a non-existing tension on the chain ends. The three forces are the friction, with ζ_0 the segment friction, the Brownian force $\vec{g}_n(t)$ that represents random collisions in the heat bath and finally, the spring force in the continuous limit $k\frac{\partial^2 \vec{R}_n(t)}{\partial n^2}$. Equation 2.12 can be solved by Fourier transformation into normal coordinates $(\vec{R}(t) \to \vec{X}(p,t))$ that results in

$$\zeta_p \frac{\partial}{\partial t} \vec{X}(p,t) = -\frac{2\pi^2 p^2}{N} \vec{X}(p,t) + \vec{g}(p,t), \tag{2.13}$$

where $\zeta_p = 2N\zeta_0$ and $\vec{g}(p,t)$ is given by

$$\langle g_\alpha(p_q, t_1) g_\beta(p_2, t_2) \rangle = 2\zeta_p k_b T \delta_{p_1 p_2} \delta_{\alpha\beta}. \tag{2.14}$$

The index p represents the mode number. The solutions with the mode relaxation time $\tau_p \approx \frac{1}{p^2} \cdot \frac{\zeta N^2 l^2}{3\pi^2 k_B T}$ are

$$\vec{X}(p,t) = \frac{1}{\zeta_p} \int_{-\infty}^{t} dt \, \exp\left(-\frac{t-t'}{\tau_p}\right) \vec{f}(p,t'). \tag{2.15}$$

The longest mode-relaxation time is $\tau_R = \tau_1$, which is called the Rouse time and is also defined as $\tau_R = \frac{N^2}{\pi^2 W} = \frac{R_E^2}{W l^4 \pi^2}$ with $W = \frac{3k_B T}{\zeta l^2}$ as the elemental Rouse rate. Often Wl^4 is also called the Rouse rate.

For the chain dynamics, the Rouse normal-mode time correlation function can be calculated as

$$\langle \vec{X}(p,t) \vec{X}(p,0) \rangle = \frac{R_E^2}{6\pi^2 p^2} \exp\left(-\frac{p^2}{\tau_R} t\right). \tag{2.16}$$

For $p = 0$ the center of mass diffusion is obtained

$$\langle \vec{X}(p,t)\vec{X}(p,0)\rangle = \delta_{\alpha\beta}\frac{2k_bT}{N\zeta}t = \delta_{\alpha\beta}2D_Rt, \tag{2.17}$$

with D_R the Rouse diffusion constant $D_R = \frac{k_BT}{N\zeta} = \frac{Wl^4}{3R_E^2}$. This is valid for each component z, y, z [1].

Additionally to the static structure factor in equation 2.6, the dynamic structure factor is also defined with the spacial correlation function, with the addition of the temporal change that is taken into account. The dynamic structure factor is

$$S(q,t) = \frac{1}{N}\sum_{m,n}\langle \exp\left[i\vec{q}\left(\vec{R}_m(t) - \vec{R}_n(0)\right)\right]\rangle, \tag{2.18}$$

and once again, using the Gaussian chain statistic approximation it can be written as

$$S(q,t) = \frac{1}{N}\sum_{m,n}\exp\left[-\frac{q^2}{6}\langle\left(\vec{R}_m(t) - \vec{R}_n(0)\right)\rangle\right]. \tag{2.19}$$

By transforming the normal modes back, one obtains the position vectors

$$\vec{R}_n(t) = \vec{X}_0 + 2\sum_{p=1}^{\infty}\vec{X}_p\cos\left(\frac{p\pi n}{N}\right). \tag{2.20}$$

The dynamic structure factor using this relation for the position vectors and the correlation for the normal modes (eq. 2.16,2.17) can be written as

$$\begin{aligned} S(q,t) = {} & \frac{1}{N}\cdot\exp(-q^2D_Rt)\cdot\sum_{n,m}\exp\left(-\frac{1}{6}|n-m|q^2l^2\right) \\ & \cdot\exp\left[-\frac{2Nl^2q^2}{3\pi^2}\sum_{p=1}^{N}\frac{1}{p^2}\right. \\ & \left.\cdot\left(\cos\left(\frac{p\pi n}{N}\right)\cos\left(\frac{p\pi m}{N}\right)\left(1-\exp\left(-\frac{t}{\tau_p}\right)\right)\right)\right]. \end{aligned} \tag{2.21}$$

For a pure center of mass diffusion of the chain the dynamic structure is given by the first term in this equation as

$$S(q,t) = N\exp\left(-D_Rq^2t\right). \tag{2.22}$$

The Rouse model describes the dynamics of short unentangled chains quite well. As long as the polymers are shorter than the critical molecular weight, which is called the entanglement weight M_e, the model is valid, however it fails for longer chains [29] [30]. Nevertheless, the model is valid for longer chains up to the entanglement time τ_e which will be discussed in the next section. The main reason it fails in these circumstances is that it neglects the topological interactions between different chains.

2.2.2 *Entangled Dynamics*

For polymers with a molecular weight larger than the entanglement mass M_e, the standard Rouse model is not applicable anymore. The reason for that is that topological interactions with other polymer chains start to dominate the relaxation behavior of the single chain. These entanglements between chains have a huge influence on the mechanical properties of the material. Entanglements act as temporary "connections" in systems when e.g. strain is applied to the material. Entangled systems show viscoelastic behavior and are an intermediate state between liquid and solid material. To account for the effects of these entanglements Doi and Edwards [1] created their "tube model" as an expansion of the reptation model by De Gennes [21]. It is a mean field approach to simplify the many body problem to one of only a single chain. The entanglements are replaced by confining topological constraints, these confine the polymer chain to a certain region, referred to as the tube, as it is the only path that the chain can move along. Movement in a perpendicular direction to the tube is restricted by the entanglements to a length scale that is called the tube diameter d. It also represents the region in space between entanglements that consists of N_e segments with $d = \sqrt{N_e} \cdot l$. A polymer consisting of N_e segments (segments $\equiv$ monomers) has a relaxation time τ_e, which corresponds to the Rouse time (τ_R) of a chain with $R_E = d$, which is refered to as the entanglement time during which it still follows the standard Rouse dynamics. It can be calculated using

$$\tau_e = \frac{\tau_R N_e^2}{N^2} = \frac{\zeta l^2}{3\pi^2 k_B T} N_e^2 = \frac{d^4}{\pi^2 W l^4}. \tag{2.23}$$

It is sufficient to introduce one additional length scale to describe the dynamic for entangled linear chains. The chain relaxation can be described using the following four different time regimes.

1. Rouse regime: $t < \tau_e$

   At times below the entanglement time, the chain dynamics can be described by the pure Rouse model, as chain monomers do not feel any restrictions by the surrounding chains.

2. Local reptation (Rouse in tube): $\tau_e < t < \tau_R$

   In the second time regime, starting at times larger than the entanglement time, the chain has explored the lateral expansion of the tube and can no longer move in those directions. This leads to a one dimensional restriction of the Rouse motion along the contour of the tube (primitive path), which is called local reptation.

3. Reptation: $\tau_R < t < \tau_d$

For $t > \tau_R$ internal modes have relaxed. The dominate process taking place at these times is reptation out of the tube. This process can be described by the tube survival probability $\varphi(t)$ which describes the average fraction of unrelaxed material or fraction of the original tube as the chain moves from its original position, which will also be discussed in Section 5.5.

The reptation or disentanglement time τ_d can be calculated as

$$\tau_d = \frac{\zeta l^4 N^3}{\pi^2 k_B T d^2} = 3Z\tau_R = \frac{3R_E^6}{\pi^2 W l^4 d^2}, \tag{2.24}$$

where Wl^4 is again the Rouse rate and R_E is the end-to-end chain distance.

4. Diffusion: $t > \tau_d$

For times larger than the reptation time τ_d, the chain has left the original tube and can proceed its diffusion unhindered, which leads to the mechanical properties of a simple fluid at these time scales.

The mean square displacement $\langle r^2(t)\rangle$ (see eq. 4.4) of a linear chain segment follows these four scaling regimes [1, 2, 31]

$$\langle r^2\rangle \sim \begin{cases} t^{\frac{1}{2}} & \text{for} \quad t < \tau_e & \text{Rouse} \\ t^{\frac{1}{4}} & \text{for} \quad \tau_e < t < \tau_R & \text{Rouse in tube} \\ t^{\frac{1}{2}} & \text{for} \quad \tau_R < t < \tau_d & \text{reptation} \\ t & \text{for} \quad \tau_d < t & \text{diffusion} \end{cases} \tag{2.25}$$

where τ_e,τ_R and τ_d are the entanglement, Rouse and disentanglement (relaxation) times, respectively, following the descriptions in [4, 32, 33]. A schematic representation of the segmental mean square displacement of a linear chain is shown in Figure 2 with the four different time regimes.

2.2.3 *Additional Relaxation Processes*

Experimentally measured viscosity of linear chains (scaling with molecular weight) has shown that there are additional relaxation processes needed to correctly describe the results, as discussed by Doi and Masao as well as Milner and McLeish [34, 35]. The two main mechanisms are constraint release (CR) and contour length fluctuations (CLF). These relaxation processes become important for star polymers as these cannot reptate.

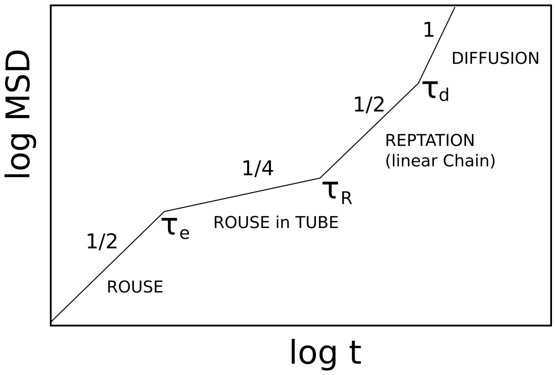

Figure 2: Schematic representation of the mean square displacement for linear chain vs time. Schematic description of the theoretical prediction with the four time zones of Rouse ($t^{1/2}$), Rouse in tube ($t^{1/4}$), reptation ($t^{1/2}$) and diffustion (t^{1})

Contour length fluctuation [36] is a correction to the assumption of fixed position and length of the primitive path. It accounts for the longitudinal fluctuations of the end segments of the chain. They affect the chain dynamics only at the time scales smaller than τ_R and do not include any center of mass motions. End segments of polymer chains can fluctuate the same way as all other segments, additionally they can also withdraw into the tube. The part of the tube that is now unoccupied by the chain is no longer relevant and the chain end can move into any other arbitrary direction which means that the initial length of the tube gets shorter over time. This process is dependent on the molecular weight of the chain as for shorter chains the relative fraction of chain ends is higher and therefore the CLF effect is stronger provided the chain is long enough to still be entangled.

Constraint release [31] is a mechanism that describes over time changes in entangled systems. For a given chain the neighboring chains that represent the fixed obstacles move over time as well. They are henceforth represented as appearing and disappearing entanglements. Formerly present obstacles to lateral chain movement can disappear over time. The changes to these constraints can be caused by fluctuations of the chain ends of neighboring polymers or by reptations of linear chains which lead to the resolution of individual constraints. This enables the tube to move in the direction of an entanglement constraint that disappeared due to the effects listed above in a Rouse like motion of the tube itself. This of course changes the original tube.

2.3 DYNAMICS OF BRANCHED POLYMERS

The presence of branch points and additional arms drastically changes the relaxation processes of polymers compared to linear chains. The commonly accepted tube model for linear chains is changed in branched polymers. The introduction of a single branch heavily slows down the overall relaxation process and leads to a more complex rheological spectra [5, 6, 7]. The rheological measurements of branched polymers show, for example, that stars have a broader spectrum of relaxation times compared to linear chain systems due to their hierarchical relaxation, amongst other things. To account for the additional complexity of such geometries additional relaxation processes have to be included in the standard tube model as polymers with sidearms cannot reptate. These relaxations happen hierarchically, which means that the process goes from the outer segments of the polymer towards the inner parts that are closer to the branch point where the mobility is lower, as the arms have to retract to the BP before it can move. This process of arm relaxation is further discussed in the section on tube survival probability (see Section 2.3.6). Some other processes to describe the branched systems are explained in the following subsections.

2.3.1 *Arm retraction and branch point motion*

The segments in highly entangled branched polymers relax hierarchically, in this process the outer arms ends relax first, progressing to the inner parts close to the branch points. As the BP is connected to several arms there is no single tube in which it can reptate. The process of arm retraction is exponentially slow which gives a wide range of relaxation times along the arm. For asymmetric stars the BP can move once the short arm has relaxed. There the shortest arm in a T-shaped 3-arm star relaxes first and acts as a friction increasing "fat bead". The BP can move along the tube of the remaining two long arms that form the backbone, but are slowed by the additional friction. This process is also sometimes called diffusive hopping. One can describe the branch point motion of such a chain by assuming a random walk

$$\langle r^2 \rangle = |L| d, \tag{2.26}$$

with $\langle r^2 \rangle$ the mean square displacement (MSD), L the length of the primitive path that is probed by the BP during its movement and d the tube diameter. With the assumption of a Gaussian distribution for the diffusion length L, one can write the MSD as

$$\langle r^2 \rangle = d\sqrt{2\langle L^2 \rangle / \pi}. \tag{2.27}$$

The diffusivity D can be related to $\langle L^2 \rangle$ because the BP motion is assumed to be diffusive and therefore $\langle L^2 \rangle = 2Dt$, with the factor two is due to the diffusion that only happens in one dimension. With these equations it is possible to create a direct way to obtain the diffusivity of the one-dimensional curviliear motion of the BP using

$$D = \frac{\pi}{4d^2}\left(\frac{\langle r^2 \rangle}{t^{1/2}}\right)^2 . \tag{2.28}$$

The factor within the brackets represents the "plateau value". The mean square displacement of the BP has a time exponent of $1/2$ so once the MSD is divided by $t^{1/2}$ it becomes flat (slope zero), which is when the polymer experiences reptational motion along the tube. The application of this will be seen in Section 6.1.2. For symmetric stars this is not applicable because there is no single arm that can act as friction bead as all arms should relax on the same time scale.

2.3.2 *Dynamic Tube Dilution*

In dynamic tube dilution (DTD) [17, 18] the tube diameter d of a polymer system changes as a parameter over time. It is a relaxation process, during which the individual chain segments explore a tube that is expanding progressively. DTD uses the same picture of entangled systems where the tube or primitive path of the chain is formed by obstacles in space. These obstacles are the other chains in the melt that cannot be crossed. As already mentioned, relaxation happens hierarchically beginning from the outer segments. This disparity in dynamics has the consequence that the inner segments of the stars are no longer hindered by the entanglements with the outer parts that have already relaxed at much earlier times. This leads to constraint release and is the origin of DTD. At times longer than the relaxation time of the outer arm segments the inner parts no longer feel the entanglements of the outer segments that have already relaxed. The relaxed material acts as a quasi-solvent, which leads to a slow dilution of the effectively entangled part of the network that can be modeled using a time dependent increase ("dilution") of the tube. The fraction of unrelaxed material in the system determines the dilated tube diameter and is proportional to the tube survival parameter (see Section 5.5).

2.3.3 *Early Tube Dilation*

Early tube dilation (ETD) [37] is a fluctuation effect that happens after time τ_e and is a relaxation process in branched systems that is similar to the dynamic tube dilation in its result. It is important to note, that it is not the normal widening of the tube that is mainly caused by constraint release and arm retractions. It is better described as fluctuations that do not produce direct constraint release. This effect was studied using simulations where the normal constraint release processes (reptation, arm retraction and DTD) were suppressed by fixing the chain ends in place, making the ETD effect much more pronounced in comparison. The main cause of the ETD is currently assumed to be the equilibration of tensions along the constrained chains. This and the ability of the branch point to perform small immersions into the tubes of the different arms, which are also called "diving modes" [38] that were seen in simulations. The relevancy of this effect at higher functionality is not yet known and was part if this investigation.

2.3.4 *Dynamical Models*

In order to describe the in the dynamic structure factor observed BP motion of symmetric star polymers the model of Vilgis and Boué [16] is used. This theory is a model to characterize the Brownian motion of chain segments and cross-links in networks. At first glance the model seems to be not applicable to describe the relaxation and mobility of polymer melts as the chains in it are permanently connected, but as it was shown [39] for a highly entangled 3-arm star, it can describe the BP confinement. As will be shown in Section 5.6.4, it can be adjusted to include DTD in order to describe stars with arms of only a few entanglements. The theory is based on the Rouse model to describe the free ideal polymer chain. Chain cross-links are introduced to create the network and are described as localized springs with a harmonic potential. This potential is dependent on the radius of gyration of the mesh as well as the monomeric friction parameter. In the model the segments stay localized within that radius of gyration, which leads to a localization plateau in the dynamic structure factor that was observed in earlier NSE spectroscopy measurements on entangled polyethylene stars [39].

Another model that describes dynamics in branched systems and accounts for dependence on functionality, is the model by Warner [40]. It describes the diffusional dynamics of specific positions in polymer chains with a Rouse approximation. It can be used to describe the movement of free chain ends, cross-links in rubbers or gels and branch points of star polymers. He starts from the de Gennes [41] diffusion law

$$\left\langle \left(\vec{R}(s,t) - \vec{R}(s,t') \right)^2 \right\rangle = D|t-t'|^{1/2}, \tag{2.29}$$

that describes the mean square displacement of a specific part ($\vec{R}(s,t)$) of the polymer chain dependent on the monomer diffusion constant D and a time dependency $t^{1/2}$ that is the consequence of the connectivity of the chains (see also Section 2.2.2). In his calculations he found that the time dependence was kept, but the actual diffusion constant was αD instead of just D. With a general dependence on the functionality of the cross-link α was found to be

$$\alpha = 2/f, \tag{2.30}$$

which means that $\alpha = 2/1 = 2$ for open chain ends, $\alpha = 2/2 = 1$ for linear chain segments and $\alpha = 2/4 = 1/2$ for cross-links of four 'arms'. This model can be used to describe the dependence of the Rouse rate on the functionality with the same $2/f$ dependence[39, 42] e.g. in neutron spin echo spectroscopy.

2.3.5 *Dynamic modulus and stress relaxation*

The deformation and flow of polymer liquids can be described by the results of rheological measurements. The two main properties measured are the storage modulus and the loss modulus of a material described by $G(\omega)$, which is the dynamic modulus. A more detailed description of (experimental) rheology can be found in Section 3.4.

It is also possible to describe the dynamic modulus and the stress relaxation process of symmetric and asymmetric polymer stars theoretically. Milner and McLeish [13] presented their theory for the symmetric star relaxation process which was extended by Frischknecht *et al.* [15] to apply for asymmetric 3-arm stars with a short side-arm that are investigated in this work.

The theory by Milner and McLeish incorporates higher Rouse modes on arm retraction and "dynamic-dilution" scaling of the entanglement length. This section will follow the key components of the calculations for the stress relaxation model that leads to the description of the dynamic modulus $G(\omega)$.

To calculate the dynamic modulus the general relaxation time $\tau(s)$ is needed with the relative arm coordinate s where $s = 0$ at the arm end and 1 at the branch point. This time has a relatively complicated form, as it has to incorporate two different time scales. The first time scale is the early regime τ_{early}. The second time regime for later times is the "activated" retraction time τ_{late} which is the time an arm takes to retract the distance s in its effective potential U_{eff}. The combined relaxation time including the crossover from early-time regime to the activated one is described as

$$\tau(s) = \frac{\tau_{\text{early}}(s)e^{U_{\text{eff}}(s)}}{1 + \tau_{\text{early}}(s)e^{U_{\text{eff}}(s)}/\tau_{\text{late}}(s)}. \tag{2.31}$$

It is dependent on three different parts, the effective potential $U_{\text{eff}}(s)$, the activated retraction time $\tau_{\text{late}}(s)$ and the early relaxation time $\tau_{\text{early}}(s)$. During the early time regime the displacement is still very close to the free end, so that the effective potential is still irrelevant to the calculations. The free arm end moves still without influence of any branch point and is mainly defined by the Rouse modes, therefore the early relaxation time is given as

$$\tau_{\text{early}}(s) = \frac{225\pi^3}{256}\tau_e s^4 Z_a^4, \tag{2.32}$$

which is dependent on the entanglement time τ_e, the number of entanglements per arm Z_a. During the later time regime τ_{late} the polymer chain is affected by the effective potential $U_{\text{eff}}(s)$. This "activated" time scale potential is given by

$$U_{\text{eff}}(s) = \frac{15Z_a}{4}\frac{1-(1-s)^{1+\alpha}\left[1+(1+\alpha)s\right]}{(1+\alpha)(2+\alpha)}, \tag{2.33}$$

with the dilution exponent α (either 1 or 4/3). with this the late relaxation time τ_{late} is obtained.

$$\tau_{\mathrm{late}}(s) \approx \tau_e Z_a^{3/2} \left(\frac{2\pi^5}{15}\right)^{1/2} \times \\ \times \frac{\exp\left[U_{\mathrm{eff}}(s)\right]}{s\left[(1-s)^{2\alpha} + \left(\left(\frac{4Z_a}{15}\right)(1+\alpha)\right)^{2\alpha/(\alpha+1)} \Gamma\left(\frac{1}{\alpha+1}\right)^{-2}\right]^{1/2}}, \quad (2.34)$$

With Γ the Euler function. Finally the dynamic modulus $G(\omega)$ for symmetric star polymers can be written in frequency space as

$$G^*(\omega) = G_0(1+\alpha)\int_0^1 ds(1-s)^{\alpha}\left(\frac{-i\omega\tau(s)}{1-i\omega\tau(s)}\right), \quad (2.35)$$

where G_0 is the plateau modulus.

For asymmetric stars one has to consider that after the short arm has relaxed the asymmetric star can reptate along the remaining tube of the backbone. Following the theory of Frischknecht *et al.*[15] the complex modulus G^* was then calculated as the sum of contributions from arm retractions, reptation and early time Rouse modes.

This calculation contains the same parameters as for the symmetric star with the addition of the length of the short arm and the parameter p which is the dimensionless constant, that is thought to be of the order of unity [15]. This "hopping" parameter is the fraction of the tube diameter, with values found between 1/60 and 1, that the branch point of an asymmetric star moves after a time τ_s^*, which is the short arm relaxation time. To calculate the effective reptation time τ_d, the effective diffusion constant D_{eff} is needed with $1/D_{\mathrm{eff}} = 1/D_b + 1/D_c$, where D_c is the Rouse diffusion coefficient

$$D_c = \frac{k_b T}{2N\zeta} \quad (2.36)$$

with k_b the Boltzmann constant, N number of monomers in the long arm and ζ the monomeric friction parameter. The effective curvilinear diffusion coefficient D_b of the BP along the backbone is then

$$D_b = \frac{(p d_h)^2}{2\tau_s^*} \quad (2.37)$$

where d_h is either the undiluted or diluted tube diameter and τ_s^* the short arm relaxation time.

2.3.6 *Tube survival probability from theory*

The tube survival probability is the amount of material that remains unrelaxed in a polymer, depending on the time. This factor is used in the dynamic tube dilution (DTD) and can be obtained from simulation by calculating the tangent correlation function for individual polymer segments [37, 43, 44] or using the same theory as Milner *et al.* [13], described in Section 2.3.5.

Using the relaxation time $\tau(s)$, which is dependent on $\tau_{\text{early}}(s)$ and τ_{late}, one can calculate the local survival probability $\delta(t, s)$ [2] at any position of the arm by

$$\delta(t, s) \sim \exp\left(-\frac{t}{\tau(s)}\right). \tag{2.38}$$

Integrating $\delta(t, s)$ over the full arm length the tube survival probability is calculated as

$$\varphi(t) = \int_0^1 \exp(-t/\tau(s))\, ds. \tag{2.39}$$

The result for calculated tube survival probability of symmetric stars with $Z_a = 5$ and 13 are shown in Figure 24.

3

EXPERIMENTS

3.1 NEUTRON SCATTERING

Neutron Scattering is an established technique to investigate materials and their behavior. Neutrons are used due to their different scattering characteristics compared to electrons or photons. Light photons or x-rays interact with the electrons of the target material and usually only have a very shallow penetration depth that is dependent on and proportional to the electron density of said material. Neutrons are electrically neutral, and have a very high penetration depth compared to charged particles like electrons, thus neutrons are invaluable to investigate bulk material. They scatter on the atomic nucleus and the scattering cross section of neutrons varies strongly between isotopes of the same material, which is exploited in the experiments. The kinetic energy of neutrons of the common experimental wavelengths of $5 - 20$ Å is in the same energy region as the excitation energy of molecular and atomic movement. This allows the measurement of structural information using measurements of angular distribution of the scattered neutrons, as well as the measurement of dynamics using the energy transfer, which lead to velocity changes. The velocity $\vec{v}$ of a neutron with mass m_n are used to determine the energy E and the momentum $\vec{p}$:

$$E = \frac{1}{2} m_n v^2 = \frac{\hbar^2 k^2}{2 m_n} \tag{3.1}$$

$$\vec{p} = m_n \vec{v} = \hbar \vec{k} \tag{3.2}$$

where $k = 2\pi/\lambda$ is the wavenumber with the wavelength of the neutron λ. The energy and momentum transfer during the scattering process are

$$\Delta E = \hbar\omega = \frac{\hbar^2}{2 m_n}(k^2 - k'^2) \tag{3.3}$$

$$\Delta \vec{p} = \hbar \vec{q} = \hbar(\vec{k} - \vec{k}') \tag{3.4}$$

where the scattering vector $\vec{q} = \vec{k} - \vec{k}'$ is the difference between the wavevector before and after the scattering process.

The neutron-nucleus interaction can be described by a Fermi pseudo potential [45]

$$V(\vec{r}) = \frac{2\pi\hbar^2}{m_n} b\delta(\vec{r}), \tag{3.5}$$

with $\vec{r}$ as the position of the neutron relative to the nucleus, m_n the neutron mass, b the bound scattering length and $\delta(\vec{r})$ the delta-function.

Table 1: Coherent neutron scattering lengths and coherent and incoherent scattering cross section for Hydrogen, Deuterium and Carbon.

Isotope	$b^{coh}(10^{-15}m)$	$\sigma^{coh}(bn)$	$\sigma^{inc}(bn)$
^{1}H	-3.74	1.76	80.26
^{2}H	6.67	5.59	2.05
^{12}C	6.65	5.55	0.001

This scattering length varies widely and unsystematically from element to element and even for different isotopes of the same element. Some examples are shown in Table 1 [45]. The scattering length between deuterons and protons is quite different (the minus sign represents a phase shift of 180 degree for the scattered wave), which makes it possible to have high contrast between chemically labeled (protonated) and unlabeled (deuterated) material that still exhibits the same molecular characteristics.

Table 1 lists different scattering lengths, b^{coh} and the two different scattering cross sections σ^{coh} and σ^{inc} as we differentiate between coherent and incoherent scattering. The coherent scattering length is the mean value of the isotope composition and nucleus-spin orientation. This means that the neutrons can be scattered coherently leading to interference and the scattering cross section $\sigma_{coh} = 4\pi|\overline{b}^2|$ which is proportional to the mean scattering length.

The incoherent scattering on the other hand describes a random distribution of isotope composition and spin orientation with completely uncorrelated scattering and no interference by other nuclei. The scattering cross section $\sigma_{inc} = 4\pi\left(\overline{|b|^2} - |\overline{b}|^2\right)$ for incoherent scattering is proportional to the mean square deviation of the scattering length. Instead of writing the scattering length for singular atoms one can write the general scattering length density as

$$\rho = \frac{\sum_i b_i}{V}, \tag{3.6}$$

with V the averaged molecular unit volume. For the investigation of systems containing different materials, the scattering contrast is of interest, which is defined as $\Delta\rho = \rho_1 - \rho_2$. This is the difference between the scattering length densities of the two materials.

The incoming neutron beam can be described as a plane wave that has the amplitude of $\exp(i\vec{k}\vec{r}(t))$, where the time dependence $E/\hbar t$ is contained within $\vec{r}(t)$. Scattering this wave on N atoms that each have the potential V_i leads to sphere shaped waves of amplitude b_i. The waves overlay each other with a resulting amplitude at the detector of

$$A(\vec{Q}, t) = \sum_i b_i \exp(-i\vec{Q}\vec{r}_i(t)). \tag{3.7}$$

The detector cannot directly measure the amplitude but only the scattering intensity. The information about the phase of the wave is lost. From the measured intensity the doubled differential scattering cross section [46] is gathered:

$$
\begin{aligned}
\frac{d^2\sigma}{d\Omega d\omega} &= \frac{k'}{k}\frac{1}{\pi}\int dt\; e^{-i\omega t}\sum_{m,n}^{N}\langle b_m b_n\rangle \left\langle e^{-i\vec{q}\vec{r}_n(0)} e^{-i\vec{q}\vec{r}_n(t)}\right\rangle \\
&= \frac{k'}{k}\frac{1}{2\pi}\int dt\; e^{-i\omega t}\Bigg\{ \sum_{m,n=1}^{N} b_m b_n \left\langle e^{-i\vec{q}\vec{r}_n(0)} e^{-i\vec{q}\vec{r}_m(t)}\right\rangle \\
&+ \sum_{m,n=1}^{N} \frac{\sigma_{\mathrm{inc},n}}{4\pi}\left\langle e^{-i\vec{q}\vec{r}_n(0)} e^{-i\vec{q}\vec{r}_n(t)}\right\rangle \Bigg\} \\
&=: \frac{d^2\sigma_{\mathrm{coh}}}{d\Omega d\omega} + \frac{d^2\sigma_{\mathrm{inc}}}{d\Omega d\omega} \\
&=: \frac{k'}{k}\left\{ N b_{\mathrm{coh}}^2 S_{\mathrm{coh}}(\vec{q},\omega) + N\frac{\sigma_{\mathrm{inc}}}{4\pi} S_{\mathrm{inc}}(\vec{q},\omega)\right\}, \qquad (3.8)
\end{aligned}
$$

with k and k' as the absolute values of the incoming and scattered vector.

The coherent and incoherent dynamic structure factors are defined as $S_{\mathrm{coh}}(\vec{q},\omega) = \frac{k}{k'}\frac{1}{N\bar{b}^2}\frac{d^2\sigma_{\mathrm{coh}}}{d\Omega d\omega}$ and $S_{\mathrm{inc}}(\vec{q},\omega) = \frac{k}{k'}\frac{4\pi}{N\bar{\sigma}}\frac{d^2\sigma_{\mathrm{inc}}}{d\Omega d\omega}$. The coherent dynamic structure factor gives the possibility to find a particle at time t at position $\vec{r}$ while any other particle was at position $\vec{r} = 0$ at time $t = 0$. The incoherent structure factor on the other hand is the self correlation function giving the probability for the same particle that was at position $\vec{r} = 0$ at time $t = 0$ to be at place $\vec{r}$ at time t. Calculating the Fourier transformation of $S(\vec{q},\omega)$ gives the intermediate scattering function $S(\vec{q},t)$

$$
S_{\mathrm{coh}}(\vec{q},t) = \frac{1}{N}\sum_{m,n}\langle \exp(i\vec{q}\vec{r}_m(t)) \cdot \exp(-i\vec{q}\vec{r}_n(0))\rangle \qquad (3.9)
$$

and

$$
S_{\mathrm{inc}}(\vec{q},t) = \frac{1}{N}\sum_{n}\langle \exp(i\vec{q}\vec{r}_n(t)) \cdot \exp(-i\vec{q}\vec{r}_n(0))\rangle, \qquad (3.10)
$$

where <> contributes the mean over the ensemble. The coherent dynamic structure factor is the sum of all position vectors of the sample particles and their development over time. The incoherent structure factor is the self correlation over time of a single particle.

3.2 SMALL ANGLE NEUTRON SCATTERING - SANS

Small angle neutron scattering (SANS) is a powerful and versatile technique for the investigation of structures in soft matter materials. The investigation range of SANS spans sizes of 10 Å up to 10^3 Å. The q-range of SANS ranges from 1 $Å^{-1}$ to 10^{-4} $Å^{-1}$ with a typical wavelength of 5 Å. Small angle scattering is a technique that allows only a structural analysis, without any energy resolution. In this work the focus lies on the dynamic of polymers but as the structure and exact labeling of the polymers is very important to interpret the results, the additional information from the static structure factor

$$S(q) = \int_{\infty}^{\infty} S(q,\omega)d\omega, \tag{3.11}$$

is important too. The scattering intensity I_{scat} that is measured by SANS is related to the structure of the sample and is compared to the incident intensity I_{inci} at the measured angle θ at detector distance L. The detector area is $A_{det} = \Delta\Omega L^2$. With this and the transmission T of the sample, the ratio between the two intensities is defined as the scattering cross section

$$\frac{d\sigma}{d\Omega} = \frac{\text{\# of particles scattered into solid angle } \Omega \text{ per time}}{\text{\# of incoming particles per time and area}}, \tag{3.12}$$

so that

$$\frac{d\sigma}{d\Omega} = \frac{I_{scat}}{I_{inci}}\frac{L^2}{A_{det}}\frac{1}{T} \tag{3.13}$$

with T the transmission. This can be normalized for the sample volume in the beam V, to get the macroscopic scattering cross section

$$\frac{d\Sigma}{d\Omega} = \frac{1}{V}\frac{d\sigma}{d\Omega}, \tag{3.14}$$

and the coherent scattering function can also be written as

$$\frac{d\Sigma}{d\Omega}(q) = \Delta\rho^2 V_{scat}\phi S(q), \tag{3.15}$$

with ϕ the volume fraction of the observed objects and $\Delta\rho^2$ the quadratic scattering contrast between two different materials and the volume of the scatter-er V_{scat}, whereas the incoherent structure factor is just a constant in small angle scattering.

A schematic representation of a SANS experiment is shown in Figure 3. The experiment consists of a wavelength selector that filters out all neutrons that are not of the wavelength λ with a $10-20\%$ distribution. A collimator system is positiond between the selector and the sample. By changing the selector-sample and/or sample-detector distance the investigated scattering angle, the q-values are changed as $q = (4\pi/\lambda)\sin(\theta/2)$ for quasi-elastic scattering. Not-scattered neutrons (direct beam) are caught in a beam stop at the center of

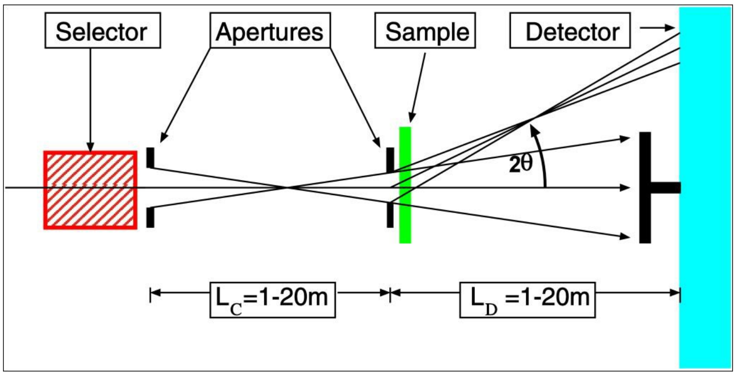

Figure 3: Schematic representation of experimental SANS setup. The neutrons fly into the wavelength selector, through the collimator (two apertures), scatter at the sample and hit the detector with the direct beam being blocked by a beamstop. The distances is varied to measure different q regimes. Picture taken from [47].

the detector and are used to measure the transmission. The position sensitive detector counts the scattered neutrons.

SANS measurements need to be corrected for instrument resolution and background. The first correction is the absolute calibration and detector sensitivity correction, which is done by measuring the scattering from a incoherent scatterer like plexiglass which has no q-dependence. The measured intensity will then be normalized with the known calibration factor of the reference. The background signal of an empty sample holder, which was a quartz glass sandwich cell as used for the samples have to be corrected for. The measurements in this work were done on the custom-made polymer stars using the parent polybutadiene polymer so the measurements could be carried out at room temperature as polybutadiene is liquid at 295K.

The experiments were performed at the KWS-2 instrument at Heinz Maier-Leibnitz Zentrum in Garching, with a wavelength of $\lambda = 5\,\text{Å}$ and a beam area of $5 \times 5\ \text{mm}^2$. The samples were measured at detector distances 8m, 4m and 1m to gather data for a q-range from 0.002 up to $0.8\,\text{Å}^{-1}$. The sample thickness was between 0.97 and 1.01 mm with roughly 80mg of polymer liquid. A far more detailed description on the experiment and the used machine can be found in Ref. [48] about the KWS-2.

The measured structure factors were compared with the theoretical calculations for the static structure factor using the De Gennes' "Random Phase Approximation" (RPA)[21, 22] (see Section 2.1.1).

3.3 NEUTRON SPIN ECHO SPECTROSCOPY - NSE

The basic principle of a neutron spin echo spectrometer (NSE) is the measurement of the energy difference of a neutron before and after a scattering event. By utilizing the neutron spin as a kind of stopwatch to analyze the difference in time that the neutron takes to cover a certain distance before and after it was scattered. Neutrons are not electrically charged, but they have a magnetic moment which leads to a precession of the neutron spin when the neutron is moving in a magnetic field.

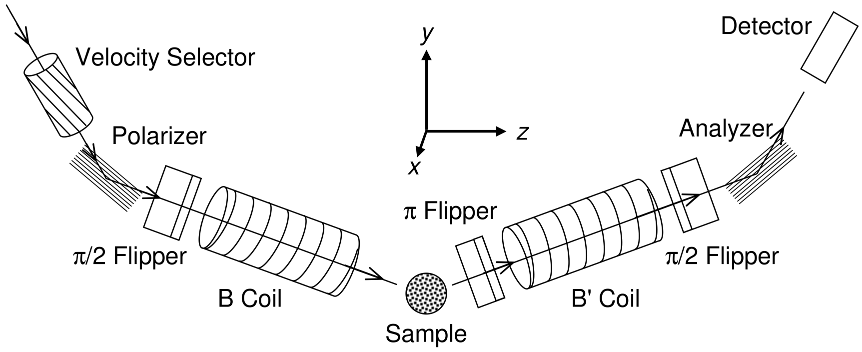

Figure 4: Schematic setup of a neutron spin echo spectrometer. Picture taken from [49].

The basic setup of a NSE spectrometer is shown in Figure 4. More details can be found in the literature e.g. the lecture notes of Mezei [50]. The neutrons are created in a neutron source, usually a nuclear fission reactor with broad wavelength (velocity) distribution. Using a velocity selector the distribution is limited to a specific wavelength band with a dispersion of usually $10 - 15\%$. A polariser (e.g. magnetic multilayer mirror) is used to filter only the neutrons that have a spin in the direction of flight. To change the spin direction to a perpendicular orientation to the magnetic field (first coil) a $\pi/2$ flipper is used. After the spin flip the neutrons enter the magnetic field of the precession coil and start their Larmor precession. Depending on the speed of the neutrons they spend varying amounts of time in the magnetic field and end up with different spin orientations. The precession angle is $\phi = \gamma/\nu \cdot J$ with γ the gyromagnetic ratio of the neutrons, ν the speed, and $J = \int_s |\vec{B}| ds$ the field integral along the flight path of the neutrons. With a π flipper the spin is turned by 180 degrees before they hit the sample. If they are scattered in-elastically, their velocity and energy change. Both energy and momentum are unchanged in the case of elastic scattering events. A second precession coil is positioned behind the sample position and the neutrons travel through it. The magnetic field is identical to the first one. The neutrons would be turned back to their initial polarization before they entered the first coil but as they inelastically interacted with the sample and changed their velocity they are not exactly in the same orientation. A second $\pi/2$ flipper is used as a mean to project the spin onto the x-z plane. The analyzer transmits the scattered neutron with a probability that is proportional to the cosine of the effective precision angle $\Delta\phi$. In the case of elastic scattering all spins are polarized back in translational direction and the signal at the detector is maximized. In the case of inelastic scattering with the sample, the velocity of the neutron is changed and $\phi_{\text{before}} \neq \phi_{\text{after}}$. This means that the second $\pi/2$ flipper does not turn the spin back in the movement direction and the signal at the detector is not maximized anymore. The transmission function of the analyzer is given by $\cos(\Delta\phi)$ with $\Delta\phi = \phi_{\text{after}} - \phi_{\text{before}}$. The probability that a neutron is scattered with the energy transfer ω and momentum transfer q is proportional to the scattering function $S(q, \omega)$. The measured signal from the NSE is the "intermediate-scattering-function"

$$S(q,t) = \int S(q,\omega) \cos\left(\underbrace{\gamma \frac{m_n^2}{2\pi h^2} J\lambda^3}_{t} \, \omega \right) d\omega. \tag{3.16}$$

The product of "neutron-constant" $\gamma \frac{m_n^2}{2\pi h^2}$, neutron wavelength cubed and the field-integral, gives the Fourier time. By changing the magnetic field in the main coil and/or the incoming wavelength it is possible to measure $S(q,t)$ at different times. To determine the form of the echo (final polarization is identical to initial), an additional coil is needed. It changes the magnetic field provided by one of the main coil slightly. The resulting oscillation of the neutron beam polarization is the spin echo group.

A perfect NSE experiment would be able to directly measure the ratio $\frac{S(q,t)}{S(q)}$ from the echo amplitude $I(q,t)$ and the average intensity $I(q,0)$. Unfortunately, in real experiments there is always a loss of polarization and therefore the maximum polarization of $I_{\text{up}} - I_{\text{down}}$ is determined by measuring the max. intensity I_{up} when all flippers are turned off and the min. signal I_{down} when only the π-flipper is active. With this information it is possible to correct the gathered signal as follows

$$\frac{S(q,t)}{S(q)} = \frac{I(q,t)}{(I_{\text{up}} - I_{\text{down}})/2}. \tag{3.17}$$

In the last step, the signal is corrected for the resolution of the instrument by measuring the purely elastic scattering on grafoil (hexagonal crystalline carbon) for which $S(q,t)/S(q)$ is ideally supposed to be 1. The actual measured function is the resolution function of the instrument. The correction for it is a simple division

$$\frac{S(q,t)}{S(q)_{\text{corrected}}} = \frac{(S(q,t)/S(q))_{\text{sample}}}{(S(q,t)/S(q))_{\text{elast}}}, \tag{3.18}$$

where "elast" refers to the fully elastic scattering grafoil. One also has to correct for the background scattering of the sample cuvette and the unlabeled material. The background correction follows the formula

$$\frac{S(q,t)}{S(q)} = \frac{2 \cdot (I(q,t)_{\text{sample}} - T_{\text{ratio}} I(q,t)_{\text{bg}})}{(I_{\text{up}} - I_{\text{down}})_{\text{sample}} - T_{\text{ratio}}(I_{\text{up}} - I_{\text{down}})_{\text{bg}}}, \tag{3.19}$$

with $T_{\mathrm{ratio}} = T_{\mathrm{sample}}/T_{\mathrm{bg}}$ as the transmission ratio of sample and background. For the measurements of labeled polymers the volume fraction of actual protonated label has to be corrected for. The protonated volume fraction varies between the lowest 4% for the large 4-arm star and 14% for the Asym S-1.0 star and the background was measured with a fully deuterated sample and has to be corrected for. It is possible to measure movement on a very small spatial scale and a time scale of $0.1 - 500$ ns for these types of polymer samples, and with special labeling schemes it is even possible to analyze the movement of only specific parts of complex polymer structures.

The neutron scattering length of deuterons and protons is very different, which leads to a contrast between the labeled part and the deuterated matrix. Specifically labeled stars with a small amount (compared to the deuterated matrix) of label at the branch point were used, thus, the coherent dynamic structure factor was measured. It shows the internal segment-segment pair correlations of the labeled section. The measurements were performed at the IN15 at the Institut Laue-Langevin, at a temperature of 509 K and wavelengths of 10 Å and 14 Å. With these settings, times up to 500 ns for four different q values in the range from 0.05 to $0.115\,\text{Å}^{-1}$ were measured. The data was corrected for the instrumental resolution and the background which was measured with the fully deuterated, linear polyethylene chains.

3.4 RHEOLOGY

Rheology is the science of deformation and flow and involves the measurement of controlled (viscometric) flow. This section follows partially the Chapter on Rheology by Sunthar [51] in rheology of Complex Fluids. In rheological experiments a force is applied to a material and the resulting velocity or shear rate is measured (or the force is measured as a result of shear rate). It also measures the effects of deformation of the material and its properties. One of these properties is the viscosity η, which is a material's fluidity, that is dependent on the material's relaxation process. Environmental parameters like temperature, pressure and shear rate, as well as the time for how long the shearing force is applied, all have influence on the viscosity of a fluid. Shear stress σ is generated by a force that is applied to a material with $\sigma = F/A$. F is the force and A is the cross sectional area of the material parallel to the applied force vector. The effective shear viscosity η is defined as

$$\eta = \frac{\sigma}{\dot{\gamma}} \tag{3.20}$$

where $\dot{\gamma}$ is the shear rate. The viscosity is measured in Pa s (Pascal second). Other than viscosity the elasticity of materials is a major focus of rheology as complex fluids exhibit elastic behavior. The elasticity of a material is defined similar to Hook's law and the modulus of elasticity is given as

$$G = \frac{\sigma}{\gamma} \tag{3.21}$$

where γ is the angle of shearing deformation or the strain. G is measured in Pa and is known as the shear modulus for fully elastic materials. The value for G in solids is usually very high ($> 10^{10}$Pa) compared to polymer melts that are in the range of $10 - 10^6$ Pa.

In viscous materials the storage and loss modulus are measured instead as they relate to the energy that is stored/lost during deformation that can be recovered. A typical measurement for polymer melts is the response to an oscillatory force and the results for a linear and star polymer melt are shown in Figure 5. The two different profiles are the G' for the storage modulus and G'' for the loss modulus of the complex modulus G^*, which are the real and imaginary component respectively. G' represents the elastic modulus of a polymer and G'' measures the viscous response. The figure can be divided into four different, distinctive zones. For low frequencies ω the polymers are in the viscous regime where they show Maxwell behavior $G' \approx G\lambda^2\omega^2$ and $G'' \approx \eta\omega$. Here λ is the characteristic relaxation time. The second zone is the transition into flow as G' and G'' cross over, with

$$\lambda = \frac{G'}{G''\omega} \tag{3.22}$$

as the characteristic relaxation time. Changes in molecular mass of the investigated polymer mainly change the response in the first two zones, with an increase in mass (and therefore chain length) stretching the curve to lower frequencies and bringing the curve higher and with a longer flat part. The third zone is the plateau area. The value of G' in this plateau is called the plateau modulus G_N^0. This plateau region is only present in entangled (relatively long) polymer melts. At higher frequencies the polymers reach the Rouse regime that is universal for all types of polymers of the same material. The slope is only different for different materials.

The big difference between stars and linear chains is easily visible in Figure 5 with the stars showing a much wider plateau region with a "double" plateau. They also typically have their crossover to viscous behavior at much lower frequencies than similar sized linear chains as the exponential scaling of the relaxation process widens the frequency regimes.

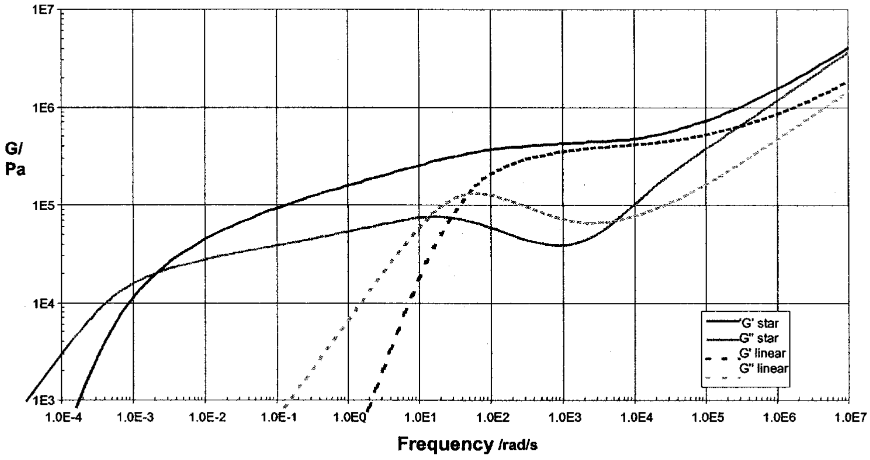

Figure 5: Comparison G' and G'' modulus of a polymer liquid of monodispers lienar and star polyisoprene melts. Figure from [2].

Rheology gives the possibility to observe the molecular polymer dynamics on a wide dynamic range. It greatly extends the accessible time region of the other experiments like NSE that can only really observe the time region around the Rouse and entangled regime. Therefore, in order to observe the full relative spectrum, the dynamic modulus G was measured to obtain the storage modulus G' and loss modulus G''. This is achieved by applying a constant strain γ to a polymer liquid and changing the plate oscillation frequency ω while measuring the dynamic response. The experiments were performed on an ARES rheometer, using 8 mm diameter circular plates with a sample thickness of 1 mm. The strain was kept at a constant $\gamma = 1\%$ and the frequency swept between $\omega = 0.1$ and $100\frac{\text{rad}}{\text{s}}$. The same measurement was performed at several different temperatures between $-85°\text{C}$ and $+25°\text{C}$ in ΔT steps of $10°\text{C}$. The dynamic responses at different temperatures is combined by the method of time-temperature superposition to generate a single master-curve (TA Orchestrator software). This curve can go to much higher and lower frequencies than experimentally possible. The principle is that different temperature responses can be shifted to one reference temperature T_R

by changing their frequency position. The shift factor is generated using the Williams-Landel-Ferry [52] (WLF) model

$$\log_{10} a_T = \frac{-C_1 \cdot (T - T_R)}{C_2 + (T - T_R)}, \tag{3.23}$$

where a_T is the shift factor and C_1 and C_2 are positive constants depending on the material and T_R. With this method it is even possible to shift the curves to temperatures that were not directly measured or are impossible to measure in this specific setup e.g. short chain polybutadiene (PB) at room temperature as these are too fluid.

As polyethylene (PE) is semi-crystalline at room temperature its parent polymer polybutadiene was chosen for the rheological measurements.

3.5 POLYMER SYNTHESIS AND SAMPLE PREPARATION

To perform the different experiments four different center-labeled star polymers were prepared. For easier visualization they are schematically represented in Figure 6. One asymmetric and three symmetric polyethylene (PE) stars were investigated by NSE spectroscopy. The parent polybutadiene (PB) polymers were used for SANS and rheological measurements. Additionally there were four polymers reused for this thesis from previous published [39] and unpublished works. These older samples are the large 3-arm star and three asymmetric stars with long backbone and short side arm. These stars were prepared in a similar fashion to those synthesized in this work.

The star arms are mostly diblock copolymers, that consist of a long deuterated and a short protonated PE part. They are covalently connected to a center branch point *via* the protonated part such that the branch point is labeled. The label size per chain was about 1 kg/mol, corresponding to about 1/2 of the entanglement mass of roughly 2 kg/mol of PE and kept the same as in previous works by Zamponi *et al.* [39] for consistency. The label was only put on three arms of the 4-arm stars to keep the same label size in all systems, which means that the fourth arm was fully deuterated. Both the 3- and the 4-arm stars were synthesized to have a "small" and a "large" version. The arm length of the small stars were produced with a overall molecular weight of 9 kg/mol corresponding to $\sim$ 5 entanglements. This size was chosen to be the exact match for the MD simulation polymers with 125 beads per arm. The larger stars have an arm length of approximately 26 kg/mol which corresponds to 13 entanglements.

There are four different asymmetric stars. They can be considered as a backbone formed by the two large arms with a third short side arm. The small asymmetric star (Asym S-1.0) has a backbone of 18 kg/mol with a side arm of 2 kg/mol which corresponds to 1 entanglement mass and is half protonated and half deuterated. One of the longer asymmetric stars has the same short side arm configuration, only the backbone is much longer at about 56 kg/mol. The two other asymmetric stars (Asym L-(0.5) and Asym L-(0.3)) have even shorter side arms with 0.9 and 0.66 kg/mol and backbones of 44 and 46 kg/-mol, respectively. In the case of these two stars the complete short sidearm is protonated and they were synthesized by Deanna Pickel, ORNL. The exact size of each star can be found in Table 2.

For all stars the center protonated label is comparatively small as the majority of the material is deuterated PE (or PB) which creates the invisible matrix for the NSE experiments. This specific labeling scheme makes it possible to directly access the motion of the branch point. All new samples and some of the reused stars were synthesized by Dr. Lutz Willner from Forschungszentrum Jülich GmbH and Hermis Iatrou from Department of Chemistry, University of Athens.

The synthesis process consists of three major steps. In the first step the single arms were created by living anionic polymerization of 1,3-butadiene.

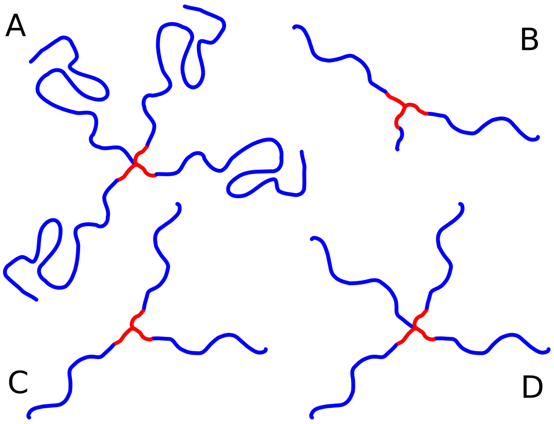

Figure 6: Schematic representation of newly synthesized polymers. The dueterated outer arms are blue and the protonated label is red. A: 4-arm large, B: Asym S-1.0, C: 3-arm small, C: 4-arm small.

In the second step these living arms were linked to methyltrichlorosilane (CH_3SiCl_3) and tetrachlorosilane ($SiCl_4$), respectively, serving as the centers for the 3- and 4-arm PB stars. The third step is the saturation of the polybutadiene with deuterium using a palladium catalyst which leads to the final PE star. The final product is well-defined and temperature stable. The polymerization of the parent PB-arm and the reaction of the linking process were performed in high vacuum using custom-made glass reactors. Details of the techniques (e.g. purification steps, used solvents and initiator preparation) and the used equipment can be found in reference [53]. The following is only a short description of the synthesis process.

The labeled PB-d_6-PB-h_6 arms (long and short) were synthesized using sequential addition of $1,3$-butadiene-d_6 and $1,3$ butadiene-h_6 respectively. The PB-d_6-PB-h_6 arms with 9 $(8-1)$ kg/mol were prepared in a larger volume as they are used for both small symmetric stars and the small asymmetric star. As the large 3-arm star was synthesized for a previous experiment [39] the long arm with 26 $(25-1)$kg/mol was separately prepared. For the small symmetric 4-arm star a single 9 kg/mol fully deuterated arm was prepared, whereas for the large 4-arm star the same 25 kg/mol deuterated block as in the diblocks was used. The used initiator was t-butyllithium in all cases and benzene was utilized as a solvent. This leads to a polybutadiene with 93% $1,4$- and 7% $1,2$ addition (random). The characterization of the arms was performed before the linking reaction.

The living arms were reacted in methyltrichlorosilane with excess arms and kept for one month to complete the funtionalization of the 3-arm stars. Methanol was used to terminate the residual arms and removed in a fractionation process.

As the 4-arm stars and asymmetric 3-arm stars each consist of two different types of arms the process was slightly more complicated. For the 4-arm star, the unlabeled arm (fully deuterated) was attached to tetrachlorosilane first. A large excess of $SiCl_4$ was used in this process to avoid multiple substitution and the excess tetrachlorosilane was removed by distillation. The d-PB-$SiCl_3$,

Table 2: Molecular Weight Characteristics of 3-, 4-arm symmetric and asymmetric polybutadiene star polymers and linear polybutadiene chains.

sym stars	$M_w^{a)}$ star [kg/mol]	M_w PB-d_6 [kg/mol]	M_w PB-d_6-PB-h_6 [kg/mol]	M_w single PB-d_6 [kg/mol]	$\frac{M_w}{M_n}$ star
3-arm small	27.3	8.2	9.2	-	1.02
4-arm small	35.7	8.2	9.2	8.8	1.02
3-arm large*	74.3	25.8	26.85	-	1.04
4-arm large	105	24.8	25.8	24.8	1.04
asym star				short d_6+h_6	
Asym S-1.0	20.6	8.2	9.2	$0.95 + 1.2$	1.02
Asym L-1.0*	55.7	27.6	28.6	$1.0 + 1.0$	1.03
Asym L-0.5*	44.9	20.0	22.0	h0.9	-
Asym L-0.3*	46.2	21.8	23.1	h0.66	-
linear chains					
Lin 6.3	12.0	12.0	-	-	-
Lin 21	40.0	40.0	-	-	-
Lin 27.4	52.0	52.0	-	-	-

[a)] Weight average molecular weight determined by multi detector size exclusion chromatography (SEC).

* samples from previous experiments

which was the product of this step, was dissolved in dry benzene and reacted with the PB-d_6-PB-h_6 labeled living arms, again with an excess of arms. They were also kept for one month and the surplus arms were removed by fractionation after termination. The asymmetric 3-arm star was constructed similarly.

The last step of the synthesis was the saturation of the polybutadiene stars with deuterium. This was performed using palladium on barium sulfate as a catalyst. The saturation was performed in cyclohexane at 90°C and 45 bars pressure while stirring. The catalyst was filtered out after the reaction and the final PE stars were obtained by precipitation in a acetone-methanol mixture.

The characterization by size exclusion chromatography (SEC) was perfomed on the PB stars, arms and blocks. A combined multi angle laser light scattering detector with an refractive index detector was used for absolute molecular weight determination. The chromatograms of the individual arms indicate almost monodisperse molecular weight distribution, as they show single narrow peaks. SEC data indicate that the stars are essentially free of single arms. The 4-arm stars contain small amounts of higher molecular weight impurities: large 4-arm star at $3-4\%$ amount and the small 4-arm star at $1-2\%$ amount. An example for the SEC is shown in Figure 7 for the small 4-arm star. Proton nuclear magnetic resonance spectroscopy (H-NMR) was used to determine the molecular weight of the protonated polymer blocks.

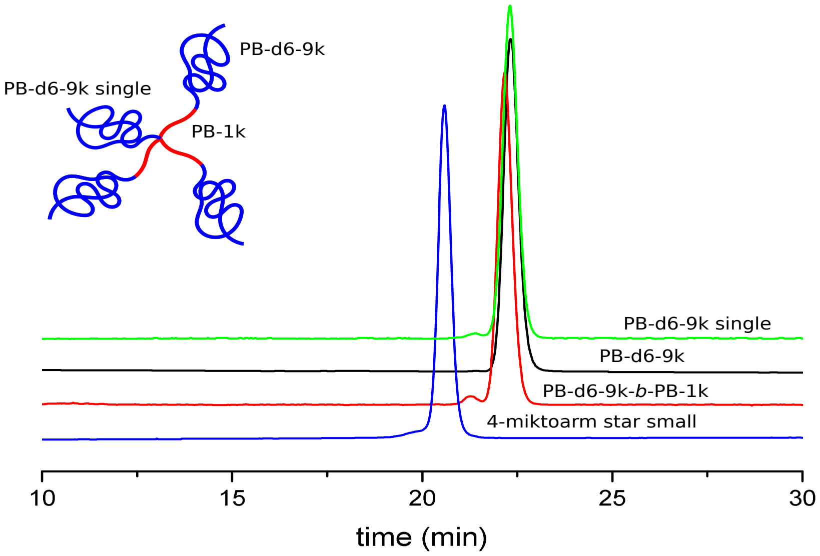

Figure 7: Size exclusion chromatography (SEC) for 4-arm small symmetric star. Green: PB-d_6-9k single arm, Black: PB-d_6-9k block, Red: PB-d_6-9k-b-PB-1k arm, Blue: final 4-arm star small after fractionation.

For neutron spin echo spectroscopy, the PE stars were put into Niobium containers with 4 mm sample thickness. To ensure the container was completely filled with the crystalline PE, it was filled and melted several times in a vacuum oven at 100°C. The sample holder was sealed in an argon glove box with a teflon seal. To remove any air bubbles the containers were kept upright in a vacuum oven at 400 K for several hours. For the rheological and small-angle neutron scattering experiments, the parent polybutadiene polymers were used as they are more or less liquid at room temperature (depending on the polymer geometry). PB is therefore much better suited for these types of experiments compared to PE which is semi-crystalline at these temperatures and would need a high temperature sample environment.

4

SIMULATIONS

Computer simulations are a great tool to investigate dynamics of complex polymer systems. They can be used to bridge the gap between theoretical models and experiments. Like every method, they have their own set of advantages and disadvantages depending on the system examined. In this work the molecular dynamics (MD) simulations can reach much longer timescales, up to a factor of 20 longer than the experimental method of neutron spin echo spectroscopy. Another advantage is that real space confinement analysis, which is the accurate tracking of individual polymer beads at any time of the simulation, is possible. Complex geometries (e.g. 5-arm stars), that would be more difficult to synthesize for experiments, can be simulated with basically the same effort as linear chains. As several approximations have to be made for the coarse grained simulations they can never be completely accurate, but should give a reasonable description for real polymers.

Coarse grained MD simulations, in contrast to fully atomistic systems, are several orders of magnitude less time consuming and therefore give the opportunity to simulate much larger sample sizes to much longer times, which increases the statistical accuracy. They do however, neglect the chemical details of the investigated polymers. That is, however, not the focus of this work as the studied polymer melt dynamic is independent of the detailed chemical composition. By simplifying the polymer chains with beads that are connected by springs and only applying simple potentials, it is almost possible to reach the regime of diffusion.

4.1 SIMULATION DETAILS AND MODEL

The classic bead-spring model is used as the base for the MD simulations and follows Kremer and Grest [4]. Beads ("monomers") connected by springs represent the linear polymers and the individual arms of the stars. The additional central bead in each star is where all arms are connected. This central bead of the star polymer or the linear chain is also called the branch point (BP). All beads have the same mass m_0 and diameter σ. By introducing a repulsive Lennard-Jones (LJ) potential between the beads an excluded volume was implemented,

$$U_{LJ}(r) = \begin{cases} 4\epsilon \left[\left(\frac{\sigma}{r}\right)^{12} - \left(\frac{\sigma}{r}\right)^{6} + \frac{1}{4} \right] & \text{for } r \leqslant r_c \\ 0 & \text{for } r > r_c, \end{cases} \tag{4.1}$$

with the cutoff distance of the potential $r_c = 2^{1/6}\,\sigma \approx 1.1225\,\sigma$. The springs connecting the beads are represented by a finite extensible nonlinear elastic (FENE) potential

$$U_F = -\frac{1}{2} K_F R_F^2 \ln\left[1 - \left(\frac{r}{R_F}\right)^2\right], \tag{4.2}$$

with a maximum bond length $R_F = 1.5\,\sigma$ and a spring constant $K_F = 30\epsilon/\sigma^2$. The LJ diameter σ is the unit length of these simulations. The combined effective potential is shown in Figure 8. A bending potential is additionally introduced between every three consecutive beads in order to implement local stiffness. The bending potential was given by:

$$U_{\text{bend}}(\theta) = a_2\theta^2 + a_4\theta^4, \tag{4.3}$$

where the angle between consecutive bond vectors is θ. The values $a_2/\epsilon = 0.92504230$ and $a_4/\epsilon = -0.054183683$ were used, which produces a potential that is almost indistinguishable from the cosine potential used by Bačová *et al.* in ref. [37]. The potential only differs for large angles which are never found in the simulation due to the repelling LJ interaction between connected beads, hence make the difference between the two potentials negligible. The used stiffness potential provides a slightly less flexible character to the chains (characteristic ratio for semi flexible chain [37, 54] $C_\infty \approx 3.6$ vs. $C_\infty \approx 1.8$ for the flexible case $a_2 = a_4 = 0$), and decreases the entanglement length. Thus, an analysis of the primitive path for this semiflexible model at the same simulated density gives an entanglement length of $N_e \approx 25$ monomers, whereas the same analysis gives $N_e \approx 65$ for the flexible case. This allows for the simulation of much 'longer' chains in terms of number of entanglements, compared to the flexible counterpart, hence these systems are much better entangled. This also results in a slightly increased time exponent in the mean square displacement (see Figure 14) for all simulated polymers compared to the theoretical model. The exponent in the Rouse regime for the linear chain is 0.6 in the simulation compared to 0.5 in the theory. As this increase is the same for all systems, it does not change the results that were gathered from the simulations significantly.

Time and length in the simulations are given in units of $\tau_0 = (m_0\sigma^2/\epsilon)^{1/2}$ and σ, respectively. The temperature $T = \epsilon/k_B$ of the simulation (with k_B the Boltzmann constant) and density $\rho = 0.85\,\sigma^{-3}$ of the monomers correspond qualitatively to a polymer melt density [4].

The procedure of Refs. [37, 55] was followed in the generation and equilibration of the simulated system. In the first step the stars and the linear chains were constructed with the correct statistics for the intramolecular distances. The goal is to create simple gaussian chains in a short time by simulating weakly entangled chains [37]. These quickly reach the gaussian equilibration regime. As a second step the complex architectures are created by connecting the weakly entangled parts. The polymer structures are put at random positions in a simulation box and the prepacking method by Auhl *et al.* [55] is followed, which constitutes of a Monte Carlo simulation. The polymers are treated as rigid objects that are shifted in large scale motions (translations,

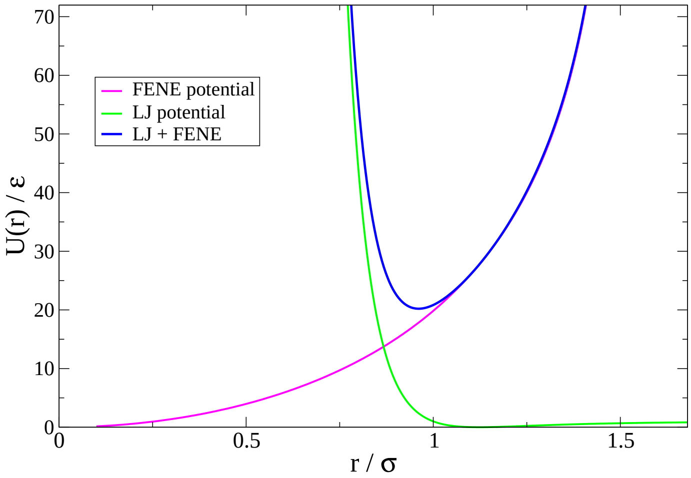

Figure 8: Lennard-Jones and FENE potential are combined to form one attractive and repulsive potential as the force field between simulated beads.

rotations, reflections, etc). The local density fluctuations of the system are calculated after each step. When they are reduced due to a position change, making the system density more uniform, the movement is accepted and used as a new starting point. This leads to a significant reduction of inhomogenities in the system with relative low computational cost. In the last step of the equilibration the standard MD simulation is run but with a capped force of the LJ potential. This is done because it is still possible for beads to have overlapping positions. This radius cap is reduced over time and at some point the final LJ potential is used. The production simulation is only run once the polymers have recovered their correct statistical properties. More details on the equilibration method are found in Ref. [37].

For all simulations with symmetric and asymmetric stars as well as the linear chains, periodic boundary conditions are used. The longest runs reached up to 4×10^8 time steps for the final production simulation. The MD simulations were performed with GROMACS [56]. Langevin dynamics was used with a friction $\Gamma = 0.5\, m_0/\tau_0$ and a time step $\Delta t = 0.005\, \tau_0$.

4.2 SIMULATED SYSTEMS

4.2.1 *Symmetric Stars*

Symmetric stars with different numbers of arms (functionality) f = 3, 4 and 5 were simulated. Linear chains with two "arms" are also included in the setup. Each simulation consists of only a single type of polymer. The polymers also all have the same number of monomers in each arm N_a, to have monodispersity. All symmetric stars can be seen in a schematic representation in Figure 9, with $N_a = 125$ corresponding to $Z_a = N_a/N_e \approx 5$ entanglements per arm. For the linear chain the backbone consists of 251 beads and $Z \approx 10$ as the number of entanglements. In the figure, N is the number of beads per star and the number of polymers in the simulated box is given by N_c. This number varies depending on the system from 200 for the linear chain (50200 total monomers) to 159 for the 5-arm stars (99534 total monomers).

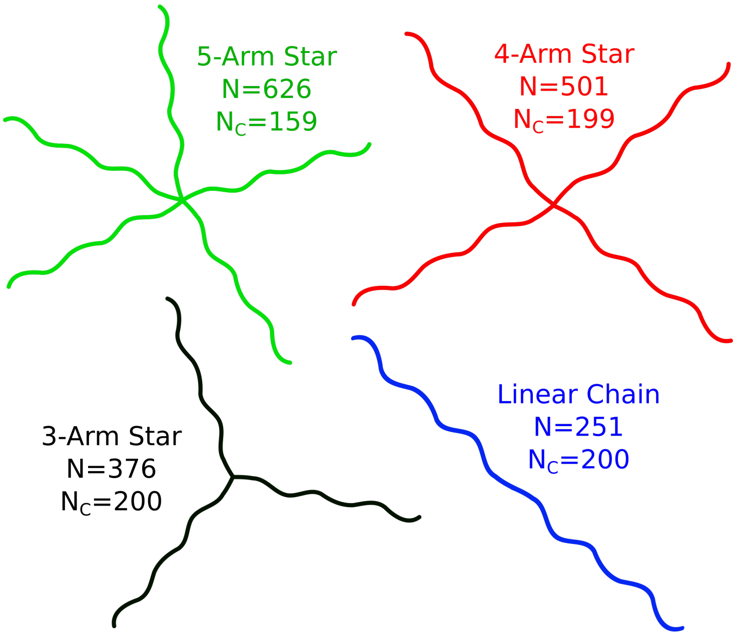

Figure 9: Schematic representation of the simulated symmetric systems. N_C is the number of polymers in the simulated box. N is the number of beads per polymer. Each arm is 125 beads long (corresponding to $Z_a \approx 5$ entanglements). For the most part the same color scheme is used to represent the corresponding data sets of each system in other figures, where it was applicable.

4.2.2 *Asymmetric Stars*

For asymmetric stars, four systems were simulated with the same backbone length but different lengths for the center positioned side branch. The geometry can be seen in Figure 10. The backbone consists of a linear chain of either 251 or 401 beads, with the center bead again being the branch point. The side arm has a length of up to 25 beads or one entanglement and systems with $Z = 1/4, 1/2, 3/4$ and 1 were simulated. The data for the star with long backbone and one whole entanglement side branch was reused from a previous work of Bačová *et al.*[37]. These systems were simulated to systematically analyze the behavior of asymmetric stars with one unentangled short side chain, up to and including the time they reach the "reptation" regime.

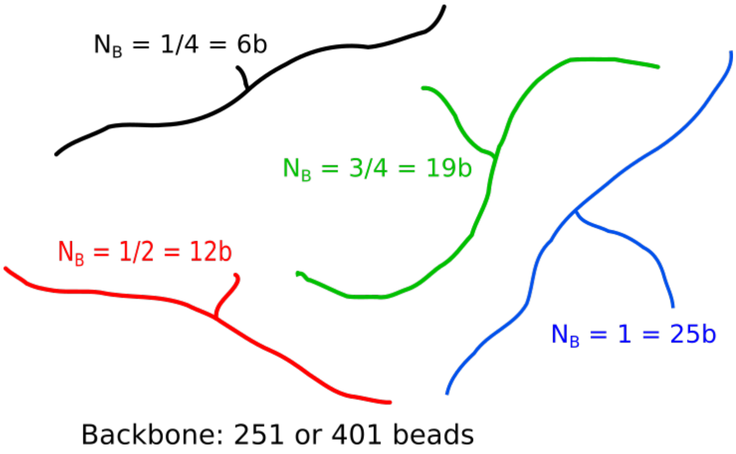

Figure 10: Schematic representation of the simulated asymmetric systems. N_B is the length of each short side branch in number of entanglements Z and number of beads b. Each system was simulated with 200 chains. The simulations were perfomed with short and long backbone stars. 'Short' equals 251 beads ($Z = 10$) and 'long' equals 401 beads ($Z = 16$).

4.2.3 *Fixed End Simulations*

The computational cost increases drastically with the length of the polymers. This can be circumvented by decreasing the number of polymers in each simulation, where the downside of this method is the reduced statistic for the data analysis. Also with the implementation of periodic boundary conditions the possibility of the chains influencing themselves increases once a certain polymer length is reached. A different way to circumvent this problem is to perform the simulations with the end monomers of each star arm fixed in place during the complete simulation run and only allowing the rest of the polymer to move. This allows a complete repression of arm retraction and other constraint release mechanisms. As a result, these systems can be seen as simulations of much longer star polymers, as in very long chains retractions and dynamic tube dilution effects play only a very small roll. This method is used in some of the real space dynamics analysis and to analyze the functionality dependence of the mean square displacement in Section 5.4 as well as a comparison to the NSE data for very long stars.

4.3 ANALYSIS

The simulations are set up to create full coordinate snapshots of each system at certain time intervals. This allows for the calculation of several parameters of the simulated polymer system. The most important ones, that are featured as results in this work, are the mean square displacement (MSD), the coherent dynamic structure factor, the tube survival probability and the individual bead movement analysis. Some of these calculations are performed only on a specific part of each molecule, the label. This allows to directly compare some of the simulation results with results from neutron scattering experiments where polymers are also labeled. As every bead of every molecule in the simulation box can be followed and identified it is possible to chose the exact label size and form.

For the calculation of the MSD the central bead of each star (and linear) polymer three beads on each connected arm were used to follow the movement of the branch point. This provides a better statistical analysis compared to the MSD of a single bead. For the calculation of the dynamic scattering functions the label was chosen to represent the corresponding label of the NSE experiments, which is $1/2$ entanglement on three arms around the branch point. As one entanglement is equal to about 25 beads, the label was chosen to consist of 13 beads on three arms plus the center BP bead (40 in total).

The MSD at a time t can directly be calculated for the labeled part

$$\langle \Delta r^2(t) \rangle = \frac{1}{N_L} \cdot \sum_{n=1}^{N_L} \left(\vec{R}_n(t) - \vec{R}_n(0) \right)^2 , \tag{4.4}$$

with the number of particles in the label N_L.

For the molecular movement analysis in Section 5.4, the average position of the stars was calculated using a sum over all positions during the calculation divided by the number of time steps. This makes it possible to compare the position of single molecules at different times to the mean path of the star or linear chain. By calculating the distances between these mean positions and the coordinate of the tracked particle, it is possible to create distance distributions for any bead.

The calculation of the tube survival probability with the use of the end-to-end correlation function is described in Section 5.5 and Refs [1, 57, 37]. Each arm is divided into short segments and the individual relaxation time of said segment is calculated. Combining these relaxation times creates the complete arm relaxation function that can be translated to the tube survival probability of the stars.

To directly compare the MD simulations and the NSE spectroscopy experiments, the coherent dynamic structure factor for the labeled branch point segment is calculated from the simulation data with

$$S(q,t) = \sum_{n=1}^{N_L} \sum_{m=1}^{N_L} \frac{\sin\left(q \cdot \left(\vec{R}_n(t) - \vec{R}_m(0)\right)\right)}{q \cdot \left(\vec{R}_n(t) - \vec{R}_m(0)\right)} . \tag{4.5}$$

The results have to be scaled to the correct time and length scales of the experiment as they are still in τ_0 and σ units.

5

SYMMETRIC STARS - RESULTS AND DISCUSSION

This chapter deals with the results of the simulations and experiments on the symmetric polymer stars. The simulations of 3-, 4- and 5-arm stars with fixed and open arm ends are analyzed to determine the dynamics of individual simulation-bead movements, tube survival probability and dynamic structure factor. In the experiments small ($Z_a = 5$) and large ($Z_a = 13$) 3- and 4-arm stars are investigated using small angle neutron scattering, rheology and neutron spin echo spectroscopy. SANS and Rheology results also include the newly synthesized Asym S-1.0 star. The results of simulations and experiments are compared where possible. The main interest of this investigation is the effect of a different functionality and different arm length on the dynamics of the polymer, specifically on the dynamics of the branch point. How these dynamic changes will also show the influence of dynamic tube dilution that is stronger for polymers with shorter arms.

5.1 SMALL ANGLE NEUTRON SCATTERING

SANS is used as a means to characterize the structure of the polymer stars. It measures the static structure factor (see Section 3.2) that is compared with the theoretical fit from RPA calculation. The theoretical fit from the synthesized geometries is compared with the SANS data, to verify the synthesis process and the sizes of the labeled branch point and the individual arm lengths. Figure 11 shows the measured static structure factor for the three newly synthesized symmetric polymer stars compared to the fitted theory. The results for the Asym S-1.0 star are shown as well.

The results show the behavior of partially labeled polymers with an expected scattering peak (RPA) at roughly $q = 0.04 - 0.06\,\text{Å}^{-1}$ depending on the polymer and a strong decay to a low incoherent background at large q ($q > 0.6\,\text{Å}^{-1}$). Additional forward scattering at very small q ($q < 0.02\,\text{Å}^{-1}$) is also observed in the experiment. The measured polymers are the parent polybutadiene (PB) stars of the PE samples. The experiment was performed at room temperature of roughly 295 K and the data was corrected for background by measuring and subtracting an empty sample cell and performing standard SANS corrections. The scattering data is normalized to a theoretical thickness of 1 mm with a factor $I = I_0 \cdot 1\,\text{mm}/d$. The experiments were performed at KWS-2 at MLZ in Garching.

The expected star composition can be found in Table 2 and the values from the fitted functions can be seen in Table 3. The fit algorithm was initially designed by Staropoli *et al.*[58]. It was adjusted to not only work for symmetric stars with a number of identical arms with a labeled center and a non-labeled outer part, but also for asymmetric stars by adding the last arm with interchangeable label and non-labeled length, so that the asymmetrical 3-arm stars with very short labeled third arms and the 4-arm stars with non-labeled fourth arm can be calculated. It calculates the random phase approximation (see Section 2.1.1) and adjusts for background and forward scattering. The theoretical static structure factor is described as

$$I = \frac{\Delta\rho^2}{N_A} \cdot \mathrm{RPA} + \mathrm{bgr} + \mathrm{pref} \cdot q^{-s}, \tag{5.1}$$

where I is the intensity dependent on q, $\Delta\rho^2$ is the contrast-factor between protonated and deuterated material divided by the Avogadro constant N_A, RPA is the random phase approximation, "bgr" is a constant background and "pref" is a prefactor for the forward-scattering with exponent s.

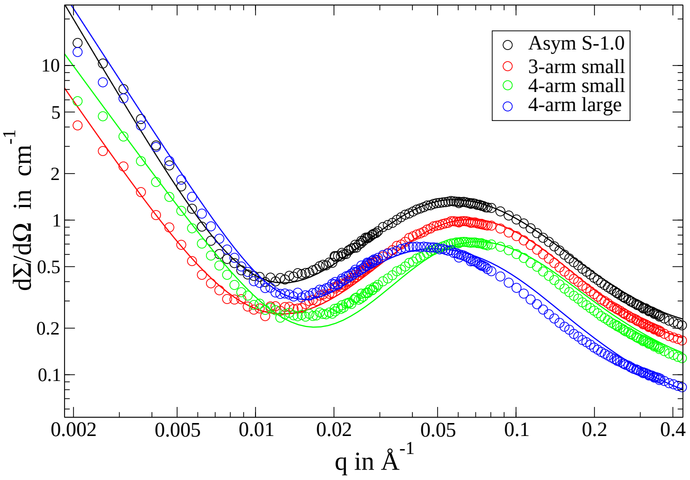

Figure 11: Static structure factor of the center labeled symmetric 3- and 4-arm and asymmetric 3-arm polybutadiene stars with fitted theoretical structure factor that includes RPA. Black circles and lines are the asymmetric 3-arm star Asym S-1.0, red circles are the small 3-arm star, green circles are the small 4-arm star and blue circles are the large 4-arm star. The measurements range from q between 0.002 and 0.4 Å^{-1} at detector settings between 1 and 8 m.

The RPA contributes to the peak height and position of the static structure factor, which is mainly depending on the geometry of the star (as described in Section 2.1.1 and in the Appendix A.1). To apply it to the experimental results adjustments to the theoretical RPA are needed. The contrast factor $\Delta\rho^2$ between deuterated and protonated material factors into the calculation as a intensity factor for the RPA.

The incoherent scattering background is constant for each sample and is proportional to the amount of protonated material in each sample. Theoretically at a scattering vector of $q \simeq 0$ there should be no scattering intensity. This is only valid when all polymers have the exact same composition [59]. The results show however parasitic forward-scattering for very small q values, which are in the fit accounted for by $\mathrm{pref} \cdot q^{-s}$. The forward scattering might be caused by different effects. It can be caused by small air bubbles (voids) in the sample and scattering on different polymer artifacts single arms, interconnects or even (fractal-) clusters and variable label sizes on the polymers [59]. Pure void scattering would lead to a exponent s of 4, but the fitted exponent is closer to a factor between 2.2 and 2.9, so a mixture is far more plausible. Two additional values that are needed in the RPA calculation, are the segment length and the monomer volume. The monomer volume of PB is of course constant for all different stars and 60 cm^3/mol, calculated from the monomer density $M_0 = 54$ g/mol divided by the density $\rho_D = 0.9$ g/cm^3. The segment length is calculated from $\frac{<R_0^2>}{M} = \frac{6R_g^2}{m_0 \cdot N}$ and $R_g^2 = \frac{N_{chain} \cdot l_{chain}^2}{6}$ [20, 60] with $\frac{<R_0^2>}{M} = 0.876$ Å^2 at room temperature and $N_e = M_e/M_0 = \frac{1900\ g/mol}{54\ g/mol} = 35$ the number of segments per entanglement. The segment length is therefore 6.88 Å, which makes the protonated label of roughly 1kg/mol on each arm correspond to about 17.5 segments. The center labeled stars all behave like in the RPA predicted with a scattering peak. The peak position and height is given by the size of the label compared to the rest of the arm and the number of arms.

The fits were made by starting with the theoretical segment lengths of the non-labeled outer part and protonated inner part of the stars (they are shown in brackets in Table 3). The fitted values were $\Delta\rho^2$, the background, the "exponent" and the prefactor within expected sizes. The size of the polymer components were adjusted slightly afterwards to receive a better match. The two different 4-arm stars do not have any protonated component in their fourth arm which would result in a segment length of 0. In the numerical calculation of the RPA however needs a non zero value. The inc. "bgr" factor follows the dependence on the amount of protonated material. The amount for each star is shown in brackets in the Table 3.

The fitted values that are shown in Table 3 for all four stars are relatively close to the values of the expected chemical composition. The theoretical length of each arm segment are shown in brackets next to their fitted values. They are overall a good verification of the geometric structure and label accuracy of the synthesis as they are generally within 10% of the theoretical value.

Table 3: Values for the static structure factor that describes the polybutadiene stars used for plots in Figure 11. The four different star arm parts are given in number of segments, with one entanglement corresponding to 35 segments. Theoretical values are shown in brackets. *The calculations would not allow values of 0 for the asym protonated part. The number in brackets for the background is the amount of protonated material in the stars.

	3-arm small	4-arm small	4-arm large	Asym S-1.0
functionality	3	4	4	3
thickness d / mm	0.968	0.989	1.016	1.009
$\Delta\rho^2/N_A$ / $cm^{-4}\cdot$ mol	$0.745 \cdot 10^{-2}$	$0.607 \cdot 10^{-2}$	$0.627 \cdot 10^{-2}$	$0.65 \cdot 10^{-2}$
# segm. D	154 (144)	160 (144)	480 (434)	150 (144)
# segm. H	16 (17.5)	17.5 (17.5)	23 (17.5)	19 (17.5)
# segm. asym D	-	170 (161)	480 (434)	15 (17)
# segm. asym H	-	2* (0)	4* (0)	22 (21)
prefactor	$13.4 \cdot 10^{-7}$	$56.8 \cdot 10^{-7}$	$22.1 \cdot 10^{-7}$	$39.7 \cdot 10^{-7}$
bgr / cm^{-1}	0.11 (11%)	0.05 (8%)	0.04 (4%)	0.15 (14%)
exponent	2.46	2.31	2.60	2.85

5.2 RHEOLOGY

To observe how the flow behavior of the polymers is dependent on their molecular structure, rheological measurements were performed on three different symmetric parent polybutadiene (PB) stars that correspond to the PE stars that were used in the NSE experiments. The data for the large 3-arm star were taken from the published results of Zamponi *et al.*[39]. All experimental results were shifted to 25°C (room temperature) to have comparability with the previously acquired experimental data.

The theoretical model by Milner *et al.* [13] (see Section 2.3.5) was used in a numerical MAPLE calculation and compared with the experimental data for the symmetric stars with only two fitted values τ_e and G_0 as listed in Table 4. The entanglement time τ_e is the characteristic value dependent on monomer friction and tube diameter and is responsible for the position on the frequency ω axis of the data. The plateau modulus G_0 alternates the plateau height and the fitted values are close to the literature value of 1.15 MPa [61]. The model also needs the entanglement mass that is 1900 g/mol and the dilution exponent α set to 4/3 as well as the arm length Z_a of the stars. The model does not include a functionality dependence.

The model is a good description for all four different stars, as can be seen in Figure 12. Two sets of stars are shown in each figure with the short and long stars shown together respectively. All stars show the expected star like rheological behavior with double plateau or plateau plus shoulder. The pair of large stars have a significantly wider shoulder region between $\omega = 5$ and 1000 rad/s that is typical for highly entangled star polymers. Linear chains would only have one "low" region in their G''. In shorter polymers these features are generally not this strongly pronounced. This can be seen in the right graph with the $Z_a = 5$ stars that do not display the shoulder at lower frequencies. They still have a more pronounced plateau region than linear counterparts.

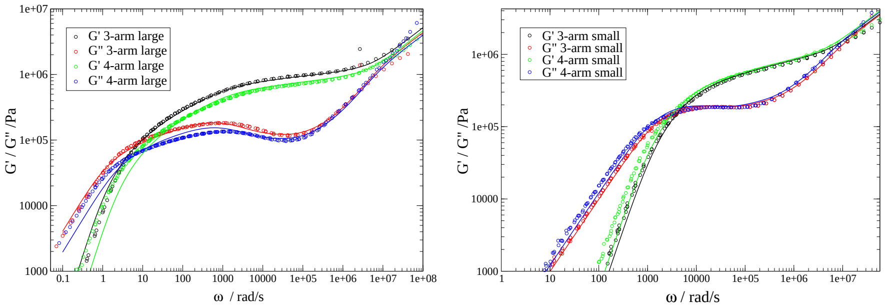

Figure 12: G'' Loss- and G' storage-modulus measured (symbols) for large symmetric 3- and 4-arm stars (left) and small symmetric 3- and 4-arm stars (right) with theoretical model (lines) shifted to 25°C

The short (arm length $Z_a = 4.85$) stars are almost identical in both G' and G''. This is expected as they have the same arm length and storage and loss modulus are not expected to change with functionality. Only for the viscosity some deviation was found for the 3-arm star (see below). Small differences could also be attributed to measurement errors or differences in the measurements. The large 3-arm star data was obtained several years prior to the 4-arm counterpart and the temperature range for the measurement was different (3-arm star measured up to room temperature and 4-arm star only up to $-5°C$). Small differences in sample thickness can also not be excluded. It is additionally noticeable that the 3-arm stars do not show a cross over between G' and G'' in the Rouse regime. The large stars show a slightly different behavior as both G' and G'' is lower for the four arm star except for the Rouse and the viscous regime where the data are basically identical. The viscous part is expected to differ in the same way as the two small stars but the arm length of the 3-arm star is about one entanglement longer than the 4-arm star, shifting it to a lower frequency. Testing the theoretical model for the 4-arm star with identical Z_a to the 3-arm stars resulted in a match of the two viscosity regimes. Other than the already mentioned errors in the measurement process the reason for the difference in plateau height might be due to effects of potential diving modes that are overshadowed by the faster relaxation in shorter stars and therefore only show in the large systems.

The theoretical model by Milner *et al.* [13] is generally a good description for all four different symmetric star systems. It only has difficulties describing the plateau region of the large 4-arm star and the viscous region of both 4-arm stars. This could be explained by the lack of functionality dependence in the model.

The Newtonian viscosity of stars increases exponentially with arm molecular weight with no functionality dependence [11], with the exception of 3-arm stars, where it was found to be about 20% lower than same length 4-arm counterparts [11]. To test this for the stars measured in this work, the viscosity of

Table 4: Rheology parameters for symmetric polybutadiene stars. All stars have the same $\alpha = 4/3$ and M_e = 1900 g/mol.

sample:	Z arm	τ_e in s	G_0 in Pa
3-arm small	4.85	0.18×10^{-6}	1.0×10^{-6}
4-arm small	4.85	0.22×10^{-6}	1.0×10^{-6}
3-arm large	15.0	0.16×10^{-6}	1.1×10^{-6}
4-arm large	14.2	0.2×10^{-6}	0.9×10^{-6}

the symmetric 3- and 4-arm stars is calculated from the rheological measurements. It can be obtained by using

$$\lim_{\omega \to 0} \frac{G''}{\omega} = \eta_0. \tag{5.2}$$

This can be plotted and the viscosity is obtained from the low frequency part where the graph is flat (seen in Figure 13) where the mean value over roughly one decade of each plateau was calculated. The viscosity results are shown in Table 5.

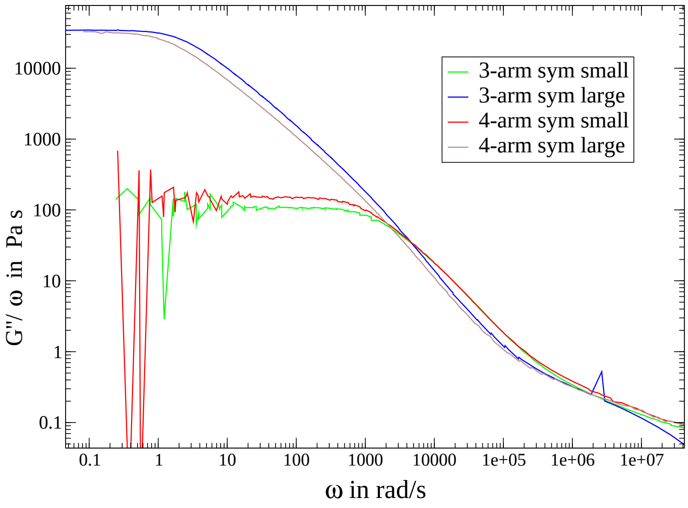

Figure 13: G''/ω for the symmetric stars. The viscosity can be read off the plateau part at low frequencies.

To determine the arm length dependence of the viscosity the same way Fetters *et al.* [11] did it in his work, the viscosity was plotted as $\ln(\eta/Z_a^{3/2})$ against Z_a. The literature value for the resulting linear slope is 0.47. The result from here measured stars was a slope of $\nu = 0.44$ which is in good agreement with the literature value considering only two pairs of each functionality were measured.

The viscosity of the 4-arm star is also slightly higher than the 3-arm star for identical arm lengths (both $Z_a = 5$), the measured stars in this work showing a difference of $\approx$ 26%. This was also expected from literature, where 4-arm stars generally have a $\approx$ 20% higher viscosity than their 3-arm counterparts.

Table 5: Viscosity for the symmetric stars, calculated from the measured loss modulus G'' at 25°C.

System	Viscosity in Pa s	arm length in kg/mol
3-arm small	110 ± 10	9.2
4-arm small	150 ± 10	9.2
3-arm large	33000 ± 1000	26.85
4-arm large	32000 ± 1000	25.8

The measured viscosity of the large symmetric stars is basically the same, this can be explained by the difference in Z_a of about one entanglement, making the 4-arm star less viscous as it is shorter.

5.3 MEAN SQUARE DISPLACEMENT

From the MD simulations, the mean square displacement (MSD) of the BP for the different star systems and linear chains is calculated according to eq.4.4. To increase the statistics of the analysis not only the singular branch point but also the closest three beads connecting to it are accounted for in the MSD calculations.

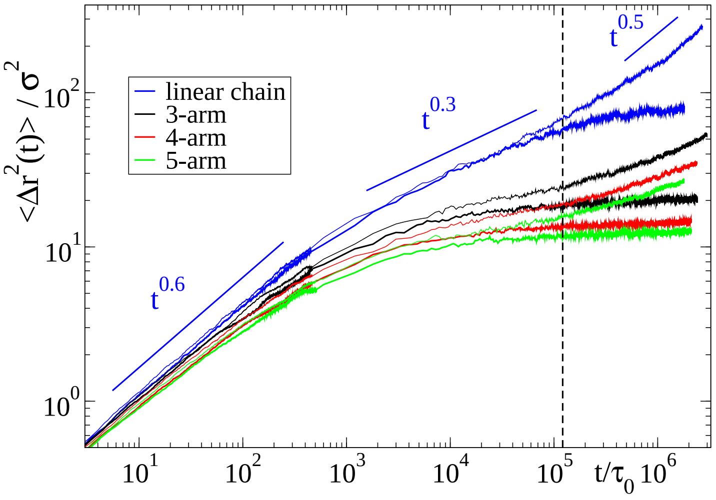

Figure 14: Simulation results for the MSD of the molecular center (branch point and three nearest beads in each arm). Data are shown both for the simulations with free and fixed ends (the latter displaying the long-time plateau). Blue, black, red and green curves correspond to the systems with functionality $f = 2$ (linear chains) and $f = 3, 4$ and 5, respectively. The solid lines indicate, from short to long times, the different power-law regimes $\langle \Delta r^2 \rangle \sim t^{0.6}$ (Rouse), $t^{0.3}$ (Rouse in tube) and $t^{0.5}$ (reptation) in the linear chains. These differ slightly from the theoretical values (see text). The vertical dashed line indicates the time scale equivalent to the limit of the NSE window, $t_{NSE} = 400$ ns (see below).

The results can be seen in Figure 14 which shows both the results for the fixed and free ends simulations. Tube theory for linear chains predicts the power laws that are described earlier in this work [1, 4, 32, 33] (see eq. 2.25 in Section 2.2.1). One can see that the linear chain with free ends follows the theoretical expectation (Rouse, Rouse in tube, reptation) well with minor differences in certain time regimes. At early times ($t < \tau_e \approx 1800\,\tau_0$ [37]) the MSD has an exponent of 0.6 instead of the 0.5 that is predicted by the Rouse model. The Rouse-in-tube time window is also slightly different with a 0.3 exponent instead of the 0.25 [1] (times between τ_e and $\tau_R = \tau_e Z^2 \approx 1.8 \times 10^5\,\tau_0$). As mentioned earlier, the small difference is most likely caused by the introduction of the small bending potential that leads to semi-flexible chains. This potential is responsible for short-range non-Gaussian interactions that are not accounted for in the classical Rouse model for linear chains. The simulations show the expected reptation behavior after the Rouse time with $\langle r^2 \rangle \sim t^{1/2}$. The diffusive time regime for linear chains start after the disentanglement time ($\tau_d = 3\tau_e Z^3 \approx 5.4 \times 10^6\,\tau_0$) but this is outside the simulation timescale.

The differences between the star polymers and the linear chains are very obvious looking at Figure 14. The branch point of the stars exhibits a much slower relaxation after the initial Rouse regime in which all polymers still behave almost identical. The slowing down increases with the number of side arms and show a functionality dependence for both the simulations with free and with fixed ends with a very large difference between the linear chain and the 3-arm star and consecutive smaller steps with higher functionality. For a quantitative analysis of the decrease in mobility the plateau height of the MSD for the simulations with fixed ends are determined. In these system the effects of dynamic tube dilution and other arm relaxation processes do not influence the mean square displacement as the fixed end beads suppress all types arm retractions and related constraint-release mechanisms. Even so, the branch point seems not to be fully localized, as one can still observe a very small increase of the MSD in the plateau region for all functionalities. These small relaxations lead to the assumption that there are still constraint release mechanisms at work like e.g. end-looping events [32] where a chain loop moves around the end of a arm to disentangle. This and other possible mechanics still have influence on the systems.

Table 6: Plateau height of the MSD in the simulations with fixed ends.

System	Plateau height (σ^2)
linear chain	75.3 ± 3
3-arm star	20.1 ± 0.5
4-arm star	14.3 ± 0.3
5-arm star	12.4 ± 0.3

The plateau height was calculated as the mean value of the MSD for times $t > 4 \times 10^5\,\tau_0$. The results can be found in Table 6. A functionality dependence of branch point motion was described by the work of Warner [40]. He calculated a generally valid description for the diffusion of cross linked polymers that is dependent on the number of links, resulting in a $2/f$ dependence of the mean square displacement with f the functionality. This can be directly compared to the plateau height p_f in MD simulations of symmetric stars with fixed ends. Table 7 shows the calculated theoretical and simulated ratios (p_f/p'_f) of the functionality and the plateau heights for $3 \leqslant f \leqslant 5$. The different ratios are in rather good agreement with the theoretical prediction. The case of $f = 2$ for the linear chain deviates from the theoretical prediction by a factor of roughly 2.5 when the Warner theory is applied. As the theory is designed explicitly for cross linked points this is not really surprising.

The differences of the branch point mean square displacement are not only caused by the different functionality dependent localization strength. Other influences besides the already mentioned end-looping are possible, like for example the "diving modes" in the early tube dilution (ETD) processes. In these modes the branch point is probing the tube of the individual arms, which could lead to a broadenig of the bare tube[37]. That in turn can have influence on

Table 7: Simulation (from Table 6) and theoretical values of the ratios of the MSD plateau heights in the systems with fixed ends. The plateau height is denoted as p_f for the system with functionality f.

	p_4/p_5	p_3/p_5	p_3/p_4
theory	1.25	1.66	1.33
simulation	1.15 ± 0.05	1.62 ± 0.08	1.40 ± 0.07

the MSD and the diving modes are also potentially functionality dependent. However these effects should stop at long times and a plateau with no further increase is expected at long enough times. The ETD effect is described by the function $g(t)$ that will be used in later parts of this work (see Section 5.6.2). A detailed description of ETD-effects and $g(t)$ can be found in the work of Bačová *et al.*[37].

Taking a closer look at the MSD for the simulations with free ends gives more insight into functionality dependent relaxations. The MSD behavior of the free end simulations can be best compared by adjusting for the contributions of early tube dilution and matching with the plateau heights obtained from the fixed end simulations. The MSD of the 4- and 5-arm stars were shifted to have the same plateau height as the 3-arm stars. Furthermore the times were also scaled to adjust for differences in branch point friction so that the Rouse regime of all stars overlap again after the vertical shift. The so determined shifting factors for time and space were also applied for the stars simulated with open ends. The result of this rescaling can be seen in Figure 15. This graph should be independent of all functionality influences. One can easily see that for the fixed end simulations the MSD plateaus overlap for the whole time range.. The free end simulations on the other hand show significant differences in the slope of the MSD. The relaxation is obviously still functionality dependent. An analysis of the graphs at times $4 \times 10^5\, \tau_0 < t < 2 \times 10^6\, \tau_0$ shows that the exponent describing the slope t^x varies between $x \approx 0.26$ for $f = 3$ to $x \approx 0.19$ for $f = 5$.

In dynamic tube dilution the renormalization of the tube parameter is only depending on the tube survival probability (see Section 5.5). If this theory is correct, DTD, within the valid time scale $t < t^*$, with $t^* = 3300$ ns (see. Section 5.5) should be independent of the functionality of the star and affect them all equally as shown in Figure 24. Even though further renormalization outside of pure DTD are necessary to include the non-constraint release "early tube dilution" (discussed in Ref. [37]), the data in Figure 15 are already corrected for the ETD, localization strength and friction differences.

This means that the differences in slope exponents are not explained by the current DTD model which is independent of functionality. The effects are more likely caused by other processes, suggesting that the DTD model is in need of a revision to explicitly account for the number of arms connected to the branch point.

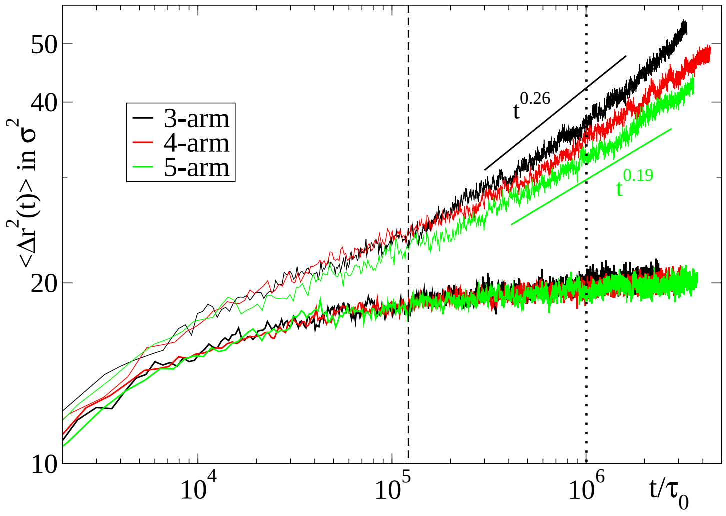

Figure 15: Rescaled MSD of the centers of the star polymers with free (three top curves) and fixed ends (three bottom curves). See the main text for details of the rescaling procedure. The black and green solid lines indicate effective power-law behavior $\langle \Delta r^2 \rangle \sim t^{0.26}$ and $t^{0.19}$, respectively. The vertical dashed and dotted lines indicate the time scales equivalent to the limit of the NSE window ($t_{NSE} = 400$ ns) and the limit of validity of DTD ($t^* = 3300$ ns, see Section 5.5), respectively.

5.3.1 *MSD of different arm segments*

In addition, the mean square displacement of different segments along the star arms was calculated to see how the mobility of larger segments depend on their positions along the arm length and if it is dependent on the functionality for both fixed and open end simulations. The MSD was calculated for a segment length of 13 beads or 1/2 entanglement at positions of 1.1 (27 beads), 2.0 (51 beads) and 3.3 (82 beads) entanglements from the branch point. To improve the statistics of the results the calculation was performed on two arms per star and averaged.

Figure 16 shows the MSD for three different segments for all three symmetric stars in the simulation with open arm ends. On the first glance it is obvious that all three stars show the exact same behavior independent of the number of arms as expected. Only for the "inner segment" the 3-arm star (black) shows a slightly higher MSD. Compared to the MSD for the BP in Figure 14 one can see that the mobility is less restricted going outward on the arm and already at a distance of about 1 entanglement length the MSD is about twice that of the branch point. This mobility for the segments increases the further one is from the branch point but again does not depend on the functionality. For the outermost segment a strong increase in mobility seems to occur already much earlier than for the two segments that are closer to the BP, since it is closest to the free arm end.

Taking a look at the MSD for the same segment positions for the simulations with fixed ends, again no dependence on functionality is found. In Figure 16 the MSD for the different segments of the 3-arm star are shown as example. In

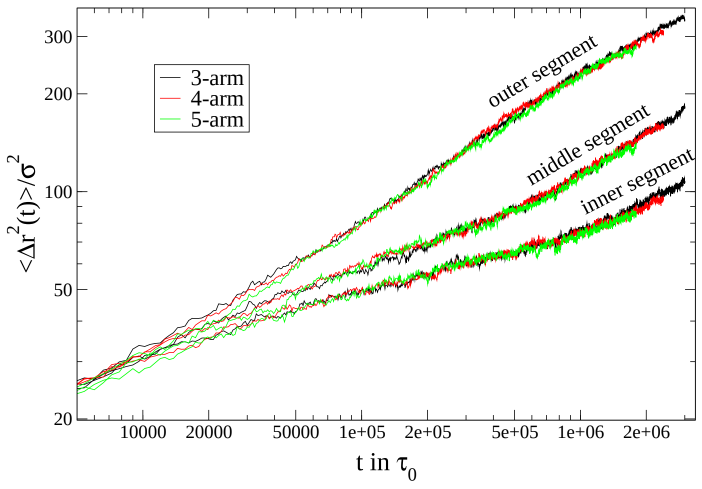

Figure 16: Mean square displacement of selected segments along the arms of the symmetric stars in the open end simulations. For each star the different segments have the same length at the same relative position from the branch point of the arm. The segments are positioned at the inner third, the middle and the outer third of the star arm.

this case, the MSE of all three segments level off into a plateau. The plateau at the end time of the simulations still has a small slope that was also observed for the branch point meaning no complete suppression of all relaxation processes. The three different segments reach their respective plateaus at different times. The innermost segments at about one entanglement distance from the BP goes into the lowest plateau, the middle and outer third segment go into a about 20% higher plateau with the outer segment taking significantly longer to reach it. The middle segment is obviously furthest from both the BP and the fixed arm end and therefore is the least influenced by restrictions caused by the fixed end point or the branch point with its multiple arms, which makes it the most mobile.

At early times the inner and outer segments show very similar behavior, only at a certain time when the inner most segment reaches its plateau the outer segment still increases until it reaches the same plateau as the middle segment. An explanation for this might be the additional "pull" of the moving branch point that the outer most segment does not experience. Additionally the outer segment is roughly 20% further from the fixed point than the inner segment is from the branch point. All three segments still have a MSD that is 2 to 2.5 times larger than the branch point MSD of the three arm fixed end star.

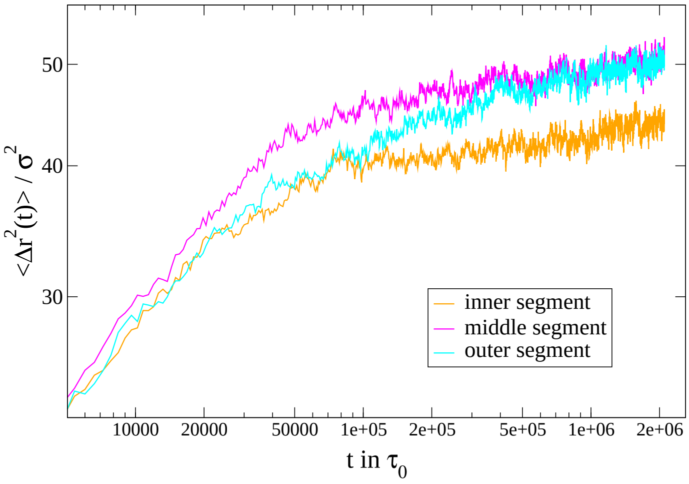

Figure 17: Mean square displacement of segments along the arms of one symmetric 3-arm star in the fixed end simulations. Each segment is the same length at a different position from the branch point of the star arm. The segments are positioned at the inner third, the middle and the outer third of the star arm.

5.4 REAL SPACE ANALYSIS

One of the biggest advantages of computer simulations is that the exact position of each molecule and bead is known at every time step of the simulation. This gives unique possibilities to take a look at spatial confinement and to analyze the movement and positions of the polymers. For this purpose the positions of different monomers along the polymer have been saved at time intervals of $t_{save} = \tau_e/4$. This makes a comparison between stars of different functionality possible as well as observing the difference between systems with fixed and open arm ends.

5.4.1 *Branch point fluctuations around mean path position*

Figure 18 displays the positions for the BP over the simulation time window for the linear chain and all different symmetric stars with fixed ends. The green line is the calculated mean path of a single polymer, and the white dots that form a cloud around it, are the position of the branch point at the different times of the simulation. The maximum time for all systems is the same and set to $t_{max} = 5 \times 10^5\ \tau_0$ as this corresponds to the maximum simulation time of the 5-arm star with fixed ends. With increasing functionality the size of the cloud gets smaller and therefore the confinement of the BP gets stronger. Even though the ends are fixed for the linear chains, one can see the expected longitudinal exploration the center bead performs along the tube.

This effect of the time evolution of this motion is shown in Figure 19. For this purpose the "clouds" have been plotted for different times during the simulation for the linear chain with fixed ends. The figure shows the same chain at $50\,\tau_e$, $125\,\tau_e$ and $500\,\tau_e$ from top to bottom. The chain appears to be moving back and forth along its tube during the time of the simulations, which is expected as it cannot reptate with fixed arm ends.

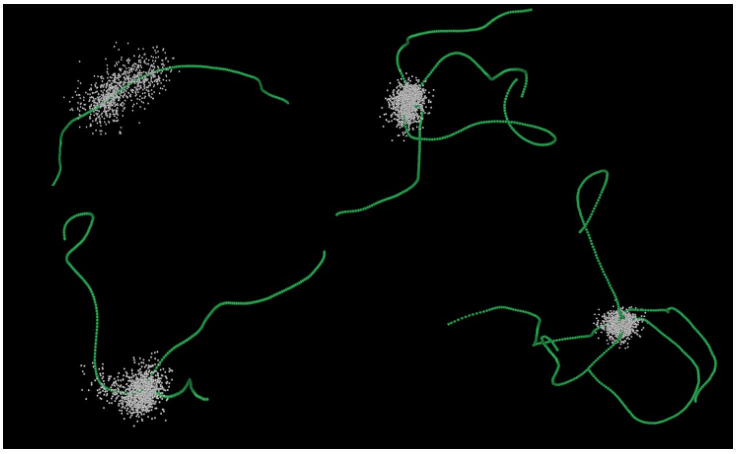

Figure 18: Green lines: typical mean paths of a linear chain, a 3-arm-star, a 4-arm-star and a 5-arm-star. The clouds of points represent the positions of the branch points at every time multiple of $\tau_e/4$. The figures have been created from the simulations with fixed arm ends.

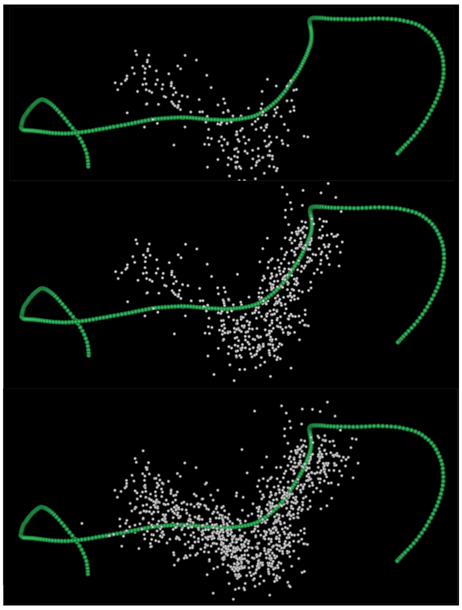

Figure 19: Time evolution of center point position in simulation of linear chain with fixed arm ends, after $50\,\tau_e$ (top), $125\,\tau_e$ (middle), $500\,\tau_e$ (bottom).

For the branched systems one can see the much stronger confinement of the BP around its mean position. In the case of the 3-arm star one can still see the branch point "diving" into the directions of the arms [37, 38]. These explorations cannot be seen in the stars with higher number of arms ($f = 4$ and 5). These deep movements along single tubes need some in-phase fluctuations of all arms around the branch point. They become highly unlikely as a result of increased drag on the branch point and are not noticed within the time frame of the simulations.

Figure 20 shows the same type of visualization of the mean path and branch point position as in Figure 18, but for the case of free arm ends. This of course leads to a greater distance distribution for the observed points in the representation. Nevertheless, one can see that even with free arm ends the confinement of the branch point increases with higher number of arms as the density of points in the center increases. This is easily visible going from the linear chain to the 3-arm star. Comparing the figure for the open end simulations with the fixed end simulations the magnitude of arm relaxation becomes clear, as the size of the cloud in Figure 18 is significantly smaller than in Figure 20.

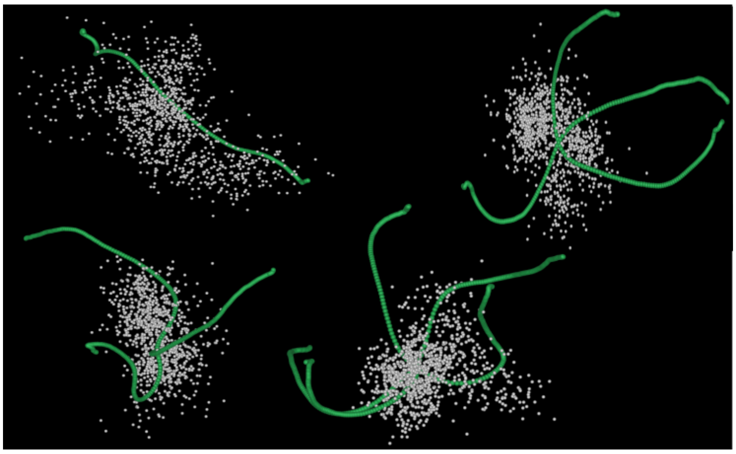

Figure 20: Green lines: typical mean paths of a linear chain, a 3-arm-star, a 4-arm-star and a 5-arm-star. The clouds of points represent the positions of the branch points at every time multiple of $\tau_e/4$. The figures have been created from the simulations with open arm ends.

5.4.2 *Monomer fluctuations along arms*

For a more quantitative analysis of the fluctuations, the normalized distribution of distances multiplied by the phase factor $G(r) \cdot 4\pi r^2$ is calculated. $G(r)$ is the distribution of distances r of the branch point at the different points in time during the simulation to the calculated mean position for the fixed arm end systems. The results are plotted in Figure 21 and show the expected behavior of stronger confinement for increased functionality. A three dimensional Gaussian function is used to fit the data. $G(r) = (3/2\pi\sigma_r^2)^{3/2} \exp[-3r^2/2\sigma_r^2]$ with σ_r the variance provides a good description of the data with the exception of the part with the largest distance to the BP. These "tails" are more pronounced for lower f and could be explained by the motions along the tubes as they are most relevant for the linear chain and the 3-arm star.

To see how strong the influence of the branching on the mobility of other beads along the arms of the polymer star is, the distribution of distances of selected monomers compared to their respective mean position are calculated and shown in Figure 22 for the 3-arm star. One can see that with increasing distance to the branch point, the distribution becomes wider, shifts to longer distances, and therefore the corresponding bead has a higher mobility. The bead for which the distribution is plotted is given in number of entanglements Z from the 3-arm star branch point up to a maximum of $Z = 2.8$, which is slightly more than half the distance between the BP and the fixed arm end. At the distance $Z > 2$ the distributions become almost identical and similar to the center bead in a corresponding linear chain, which means that the influence of the BP has almost stopped. To test how the functionality of the polymer stars influences this behavior, the same calculations have been performed for

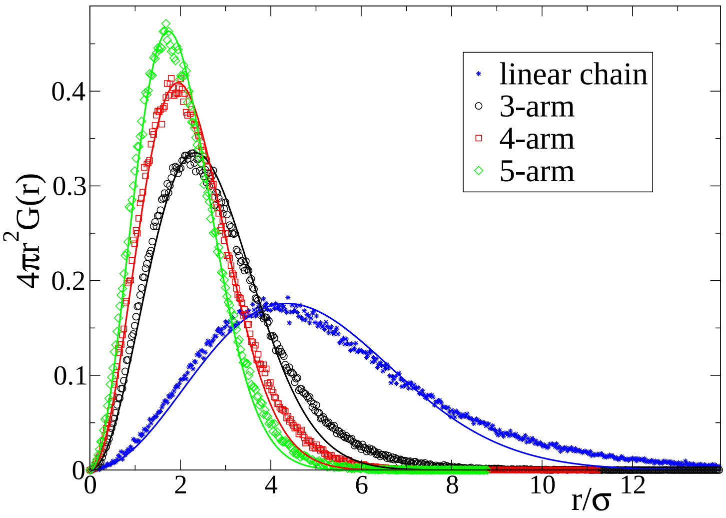

Figure 21: Distribution of distances between the branch point and its respective position in the mean path (symbols) with fits to a 3d-Gaussian function (lines).

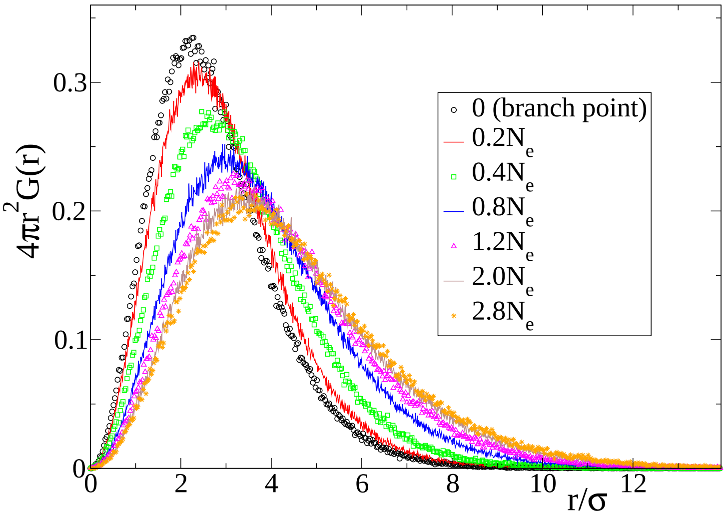

Figure 22: Distributions of distances between selected monomers of the 3-arm star and their respective positions at the mean path. Each distribution is labeled (see legend) by the chain contour distance (number of monomers) between the selected monomer and the branch point (in units of the entanglement length $N_e = 25$).

the two other star systems and the average fluctuation $\langle r^2 \rangle^{1/2}$ is plotted in Figure 23. The plots show the data normalized to the fluctuation of the corresponding linear chain with $\langle r^2 \rangle = \int_0^\infty 4\pi r^2 G(r) dr$. The x-axis of the plot is given as the contour length as a function of N_{arm}/N_e with 0 as the branch point position and 5 as the fixed arm end. Once normalized the difference in confinement with respect to the functionality can be observed especially close to the branch point where the split between the three systems is quite obvious. The difference gets much smaller at around two entanglements from the BP, but even at distance of 3Z the fluctuations of the monomer in the branched systems are still about 10% reduced compared to the linear chain.

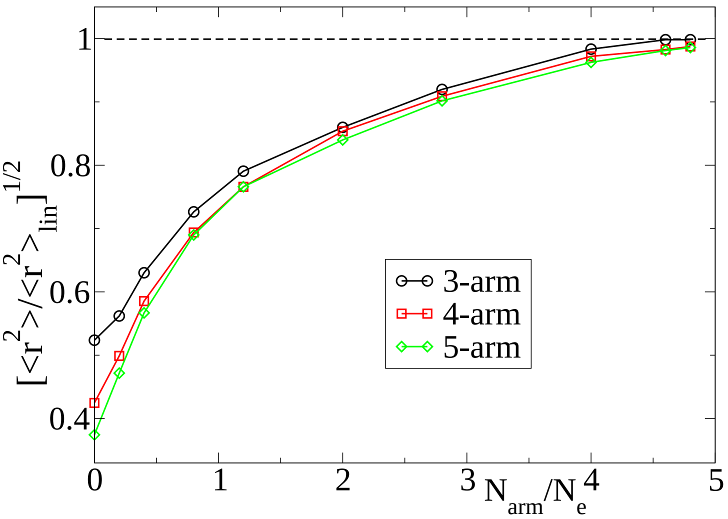

Figure 23: Average fluctuation of selected monomers around their positions in the mean path, normalized by the corresponding value for the linear chains. The horizontal dashed line indicates the reference of the linear chain, $\langle r^2 \rangle = \langle r^2_{\text{lin}} \rangle$. The data are represented vs the normalized contour distance, N_{arm}/N_e, to the branch point (so that $N_{\text{arm}}/N_e = 0$ and $N_{\text{arm}}/N_e = 5$ correspond to the branch point and the fixed arm end, respectively).

5.5 TUBE SURVIVAL PROBABILITY

The hierarchical relaxation processes have to be followed before the branch point of the investigated stars can move outside of its initial "tube" area. The dominating relaxation process for these fairly entangled (arm length $Z = 5$) stars is the dynamic tube dilution process. The DTD is proportional to the amount of unrelaxed material in the system, which corresponds to the tube survival probability. The tube survival probability (TSP) $\varphi_l(t)$ can be written in terms of the tangent correlation function following Doi and Edwards [1]. In the free end simulations the equation

$$\varphi_l(t) = \left\langle \vec{u}_{i,l}(0) \cdot \left(\vec{R}^e_i(t) - \frac{1}{f-1} \sum_{i \neq j}^{f} \vec{R}^e_j(t) \right) \right\rangle \tag{5.3}$$

gives the tangent correlation function. A detailed description of the calculations is given in Ref. [37]. $\vec{u}_{i,l}(t)$ is the tangent vector of the l-th segment of the i-th arm at time t. The end-to-end vector of the i-th arm is $\vec{R}^e_i(t)$. As in the symmetric stars all arms are identical we calculate the average over f number of arms. The sum includes all non self referencing arms and carries the cross-correlation factor $1/(f-1)$. For the calculations each arm is divided into segments of 10 beads in length (12 segments in total) that are numbered from the branch point to the outermost segment going l = 1, 2, ..., n_s with the outermost segment $n_s = 12$. The tangent vector $\vec{u}_{i,l}(0)$ is the end-to-end vector of such a segment. As a tube coordinate $s_l = l/n_s$ is chosen that as one goes from $s_l = 1/n_s$ to $s_l = 1$ the position changes from the branch point (where $S_l = 0$) to the end of the arm. A Kohlrausch-William-Watts (KWW) function, which is a basic stretched exponential $\phi_l(t) = \exp(-(t/\tau_K)^\beta)$ is used to fit the data. Plotting the relative tube coordinate s_l against the KWW relaxation times τ_K of the according segments in Figure 24 (symbols) for the symmetric stars and in Figure 25 (symbols) for the different arms (short and long) of the asymmetric star shows the decay over the time of the simulation. The total tube survival probability for the stars, which corresponds to the total fraction of unrelaxed material is

$$\Phi(t) = \frac{\sum_{i=1\dots f} Z_i \cdot \varphi_{i,l}}{\sum_{i=1\dots f} Z_i}, \tag{5.4}$$

where Z_i is the number of entanglements per arm and the sum goes over the number of arms f in the star. For the symmetric stars the total tube survival probability is the same as for a single arm, since they are all identical and hence $s(t) \hat{=} \Phi(t)$. In the case of the asymmetric stars the different arm lengths have to be considered. The resulting overall tube survival probability decays just slightly faster than the single long arm (see Figure 25 blue line), as most of the star material is contained in the two long arms.

The results for all three different symmetric stars (3-, 4- and 5-arm see Figure 24) show within their error margins the same non-exponential behavior and can again be fitted by a KWW function. The fitted stretched exponential with $\beta = 0.44$ and $\tau_K = 2.9 \times 10^6\, \tau_0$ can be used to describe the tube survival probability of the different symmetric stars.

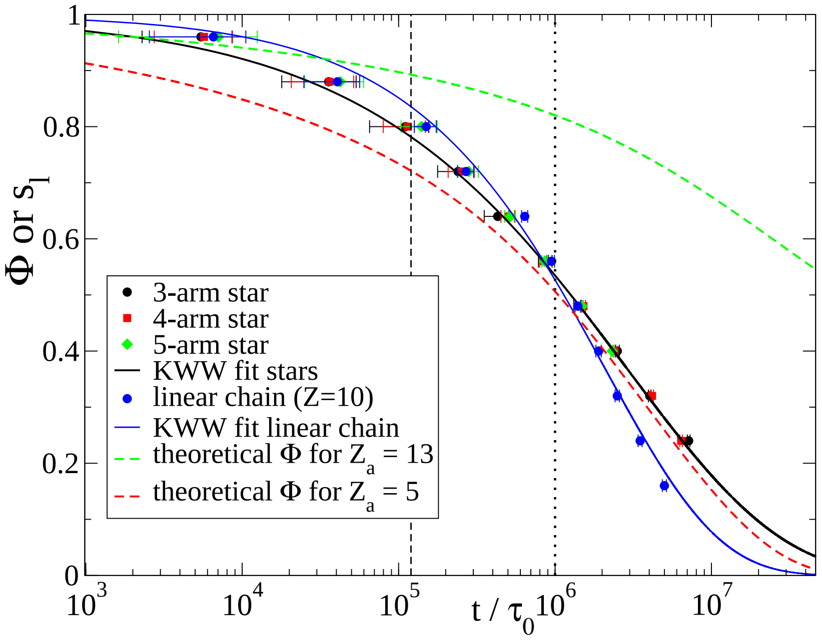

Figure 24: Unrelaxed path coordinate s_l of different segments (symbols) of arms for 3- (black), 4- (red) and 5-arm (green) star as well as linear chain (blue). The black solid curve is a KWW fit for the stars and the blue solid line for the linear chain. The dashed lines are the theoretical tube survival probabilities Φ for $Z_a = 5$ (red) and $Z_a = 13$ (green) calculated with Milner and McLeish theory with $\alpha = 1$. Vertical dashed line is the time scale equivalent to the limit of the NSE window, $t_{NSE} = 400$ ns. Vertical dotted line is the validity time window of the DTD for $Z_a = 5$ at $t^* = 3300$ ns.

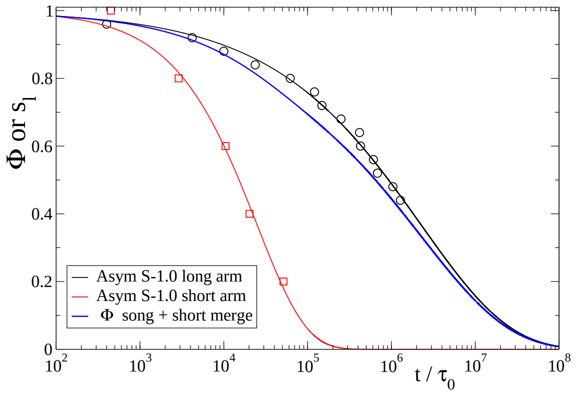

Figure 25: Unrelaxed path coordinate s_l of different segments (symbols) of short sidearm (red) and long arms (black) for the asymmetric star. Red and black lines are the corresponding KWW fits. The blue line is the combined tube survival probability for the complete asymmetric star.

The DTD is only valid for a certain timescale [2]. This means, that DTD is only valid at times, where the rate of tube broadening is slower than the rate for self-diffusion of the monomers on the segments relaxing at the same time (the tube would otherwise not influence the chain relaxation).

The equation

$$(1-s)s^2 > \frac{2}{3Z_a}, \tag{5.5}$$

with the tube coordinate s, gives this limit [2]. For $Z_a = 5$ this means that DTD is only valid for $s > 0.55$ which translates to the tube survival probability up to times $t < t^* = 10^6\,\tau_0$. With the simulations much larger times can be reached, but the functionality dependent divergence that was observed in the rescaled MSD curves already happens well within the DTD time window as can be seen in Figure 15.

To compare the star tube survival probability for the stars to that of a linear chain the same relaxation times for the "arms" of a linear chain were calculated. In the case of a $Z = 10$ linear chain it consists of two arms of $Z_a = 5$ for which the relaxations from the outer to the innermost segments are shown in Figure 24 compared to the three different stars. Within their error bars, the linear chain shows the same behavior as the stars up to a time of about $10^6\,\tau_0$, after which it decays faster than all three stars. This is also the same time scale up to which the DTD is still valid. The TSP for the linear chain can also be approximated by a stretched exponential function with $\beta = 0.6$ and $\tau_K = 2.1 \times 10^6$. It is nevertheless very interesting that within the validity time regime of DTD the linear chain relaxes basically identical to the stars and the expected faster relaxation only emerge at very large times. This shows that the relaxation of the outer segments of a star arm of the length $Z = 5$ is not influenced by the branch point at early times.

The TSP can also be calculated with the theory introduced by Milner and McLeish and compared to the results from the simulation. Further details and the exact analytical expressions can be found in Section 2.3.5, Section 2.3.6 and e.g., Refs. [13, 62]. The theoretical tube survival probabilities for stars with arm lengths $Z_a = 5$ and 13 are plotted in Figure 24 (red and green dashed lines). The theory provides a decent description of the simulation results at times longer than the Rouse time of the arm $\tau_R = \tau_e Z_a^2 \approx 5 \times 10^4 \, \tau_0$. However they generally predict a lower (about 10%) TSP than the siumulation results. As simulation results for long arm systems are not available it is the only way to obtain TSP predictions for these systems.

5.6 DYNAMIC STRUCTURE FACTOR OF SYMMETRIC STARS

5.6.1 *NSE - Functionality and Size*

One of the key experiments to analyze the dynamics of branch point motion is the neutron spin echo spectroscopy. It gives the possibility to directly measure the dynamic structure factor for the BP of the polymer stars. This is possible due to the small protonated label (3 times $1/2$ entanglement) that is only placed around the BP making it the only "visible" part of the polymer in NSE sectroscopy. The measurements were performed on large ($Z_a = 13$) stars with 3 and 4 arms as well as their smaller ($Z_a = 5$) counterparts. The large 3-arm star sample was made for and already used in the work of Zamponi *et al.* [39] and the measurements were repeated in this work to achieve longer times in the NSE experiments. This makes it possible to directly compare stars of different size and functionality. Measurements were made for times up to roughly $400\mathrm{ns}$ and at different q values between $q = 0.05\,\text{Å}^{-1}$ and $0.115\,\text{Å}^{-1}$. The size of the protonated label was kept the same for all four investigated systems and the only changing factor was the deuterated part of each star. The exact chemical composition and synthesis can be seen in Table 2 and Section 3.5 respectively. The experiments were performed at a temperature of 509 K, where the polyethylene stars are in the melt state. The normalized dynamic structure factors, $S(q,t)/S(q)$, with $S(q) = S(q,0)$, are shown. How the data is obtained is described in detail in Section 3.3.

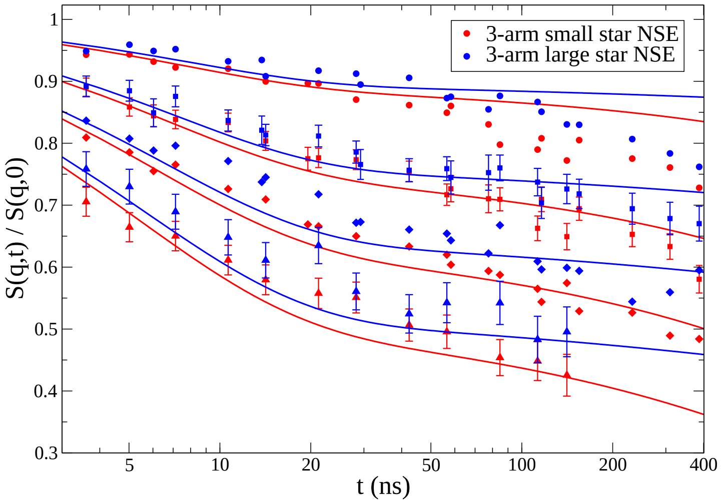

Figure 26: Measured dynamic structure factor of large $Z_a = 13$ (blue) and small $Z_a = 5$ (red) 3-arm stars. Symbols are NSE data, lines are fits to the theory (see text). The q values are $0.05\,\text{Å}^{-1}$, $0.077\,\text{Å}^{-1}$, $0.096\,\text{Å}^{-1}$ and $0.115\,\text{Å}^{-1}$ from top to bottom.

To see the effect of arm length on the mobility of the BP we compare the structure factor of stars with the same number of arms. A direct comparison of the 3-arm small (moderately entangled) and long (strongly entangled) star is shown in Figure 26 and in Figure 27 the results for the corresponding 4-arm stars are plotted. These plots also include the fit with the model function which will be described in detail later in this chapter. Comparing the different star

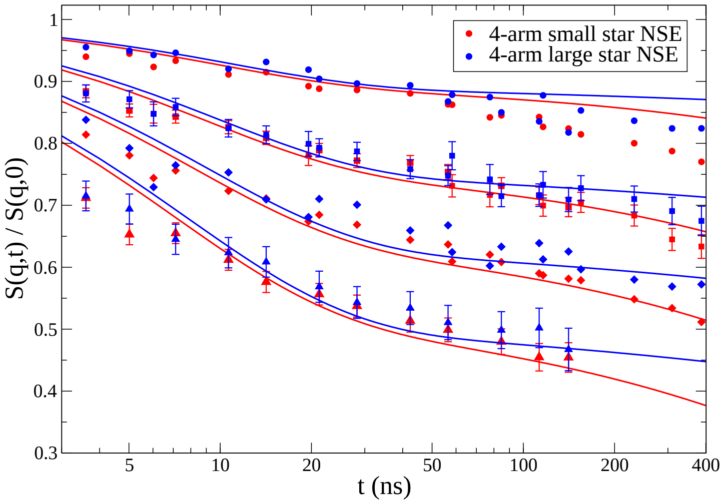

Figure 27: Measured dynamic structure factor of large $Z_a = 13$ (blue) and small $Z_a = 5$ (red) 4-arm stars. Symbols are NSE data, lines are fits to the theory (see text). The q values are $0.05\,\text{Å}^{-1}$, $0.077\,\text{Å}^{-1}$, $0.096\,\text{Å}^{-1}$ and $0.115\,\text{Å}^{-1}$ from top to bottom.

sizes, one can easily see that $S(q,t)/S(q)$ shows a faster decay for the smaller stars, this represents a higher mobility of the labeled branch point. During the early times both stars show very similar behavior up to around 30 ns. At intermediate times between 30 ns and about 80 ns the slope flattens out and at later times larger than 100 ns the stars show additional decay which means further relaxation. This additional decay is much stronger for the small stars than for the larger counterparts that only show a very small decay at these long times. As the full arm relaxation times are far beyond the experimentally observable time scale this relaxation can probably be attributed to a broadening of the tube by DTD. As this effect is obviously stronger for the small stars this is in accordance with the expectations from DTD theory. The same behavior as observed in the 3-arm stars is reflected in the 4-arm systems. Both systems show that longer star arms lead to a much stronger confinement of the branch point.

The effect of functionality on the dynamic structure factor can be seen in Figure 28, where the small 3- and 4-arm stars are plotted against each other and in Figure 29 for the large stars. The graph also includes the results of the MD simulations which will be further discussed later on. Starting with the small stars, one can see that they show very similar behavior for early times but start do deviate from each other at around 80 ns. The 3-arm star shows clearly a faster decay which follows the expectation of a stronger confinement (slower decay) for higher number of arms. This effect is visible in all four different q values. Taking a look at the large stars the picture looks similar but with a much less pronounced difference between the 3- and 4-arm stars. They still show the general trend, but the data overlaps within the error bars. This is consistent with the findings from the mean square displacement and real space analysis of the MD simulations (see Sections 5.3 and 5.4) if the stars with fixed ends are used as a substitute.

5.6.2 *NSE compared to scaled MD Simulations*

To make a direct comparison between the results of the MD simulations and the NSE spectroscopy measurements as shown in the Figures 28 and 29, the coherent dynamic structure factor of the simulated systems has been calculated using equation 3.9. For this calculation only the parts of the stars that correspond to the protonated label are included. This equals to 13 beads (1/2 of the entanglement length of 25 beads) on three arms of the star plus the branch point itself. This is also kept for the 4- and 5-arm stars. As the simulations are in Lennard-Johns units the results have to be scaled to make a direct comparison in experimental times (ns) and wave vector (Å^{-1}) possible. This was achieved by scaling the times with the corresponding ratio of entanglement times and the q values with the tube diameters ratios.

The scaling factor for the simulation time comes to $\gamma_t = 7/2100$ ns, with $2100\,\tau_0$ and 7 ns as the approximate values of the simulation [63] and experimental [39] entanglement time respectively. A slight adjustment of $\approx 17\%$ compared to the theoretical value of $1800\,\tau_0$ to the entanglement time has been performed to create a better match. To rescale the q values from the simulation to their experimental counterparts the factor $\gamma_q = 49/8.75, \text{Å}/\sigma$ was applied. 49 Å corresponds to the experimental tube diameter of linear polyethylene chain [36] and $8.75\,\sigma$ is the value from bead-spring simulated chains [64]. These rescaling parameters gives a good agreement between the dynamic structure factor for the comparison of molecular dynamics simulations and neutron spin echo spectroscopy experiments for the small stars as can be seen in Figure 28. In all NSE measurements for both large and small stars a systematic discrepancy between theory and experiment can be found at $q = 0.05\,\text{Å}^{-1}$. This same inconsistency is found between the simulation results and the experiment. The experimental data showed a stronger drop in $S(q,t)/S(q)$ as both the simulations and the theory. The reason for this difference that was solely seen at the lowest measured q value is not clear at this moment. As will be shown later, the theoretical description is in good agreement with the simulations (see Figure 30) (within experimental time scale) and it is only the experimental results that show this drop. This gives reason to believe that it might be just an artifact from the experimental setup. An explanation could be the close proximity of the detector to the primary beam at the small angles that are needed for the lowest q values, but the true nature of this effect is not known yet.

As already mentioned the simulations of the small 3- and 4-arm stars show very similar behavior to the results from NSE spectroscopy experiments. This means that they again support the notion that higher functionality increases the confinement of the branch point in the symmetric stars. The simulations show a more pronounced difference between the stars already at much earlier times as seen in Figure 28 and 29. The simulated larger stars were as stated in Section 4.2 not simulated with corresponding arm length but for small stars with fixed arm ends, as simulations of such long chains have very high computational cost. Even though the simulations with fixed ends suppress almost all relaxations, it is nevertheless interesting to compare the data with the experi-

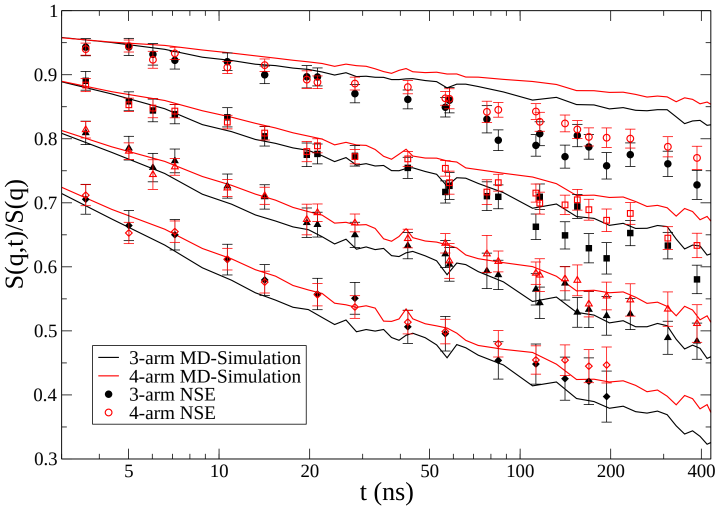

Figure 28: Dynamic structure factor from NSE (symbols) and MD simulations with rescaled units (lines), for small 3-arm (black) and small 4-arm (red) stars. The q values are (in $Å^{-1}$): 0.05 (circles), 0.077 (squares), 0.096 (triangles) and 0.115 (diamonds), from top to bottom.

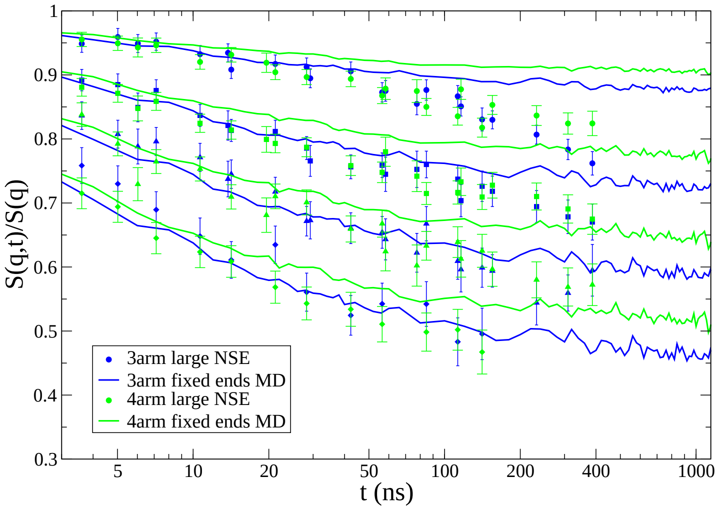

Figure 29: Dynamic structure factor from NSE (symbols) and MD simulations with rescaled units (lines) for large 3-arm (blue) and large 4-arm (green) stars. The q values are (in $Å^{-1}$): 0.05 (circles), 0.077 (squares), 0.096 (triangles) and 0.115 (diamonds), from top to bottom.

ment. The simulations (see Figure 29) go into a pronounced plateau as already expected from earlier results in the mean square displacement. They also show a distinct difference for the different functionality, that is more pronounced than in the experiment, especially at longer times. At early times up to ≈ 20 ns the NSE and MD data agree, at longer times the experimental data show a clear decay from the intermediate plateau which is reflecting the progressive loss of confinement through dynamic tube dilution that is not present in the fixed ends simulations.

5.6.3 *Theoretical Description using a modified Vilgis and Boué model*

The existing theoretical descriptions for polymer dynamics are often only applicable for linear chains or fixed networks and are not applicable for more complex architectures like symmetric stars. In order to find a theory to describe the motion of the BP in simulated and measured star systems the model of Vilgis and Boué [16] was used as a starting point. This model describes the dynamics of confined chain segments in cross linked polymer networks by a harmonic potential.

This model allows to describe the BP confinement in large star polymers[39], because relaxation processes, such as DTD are negligible in the accessible NSE time window for these large stars. Going to shorter arm length as the here investigated stars these processes become more important. For these reasons the Vilgis and Boué model was modified to include arm length dependent DTD.

Within the Vilgis and Boué model, the relative mean square displacement of two monomers m and n is calculated as[16, 39]

$$\begin{aligned}\left\langle\left(\vec{r}(m,t)-\vec{r}(n,0)\right)^2\right\rangle &= 3R_{\text{mesh}}^2\left[1-\frac{1}{2}\left(2\cosh\left(\frac{l^2}{3R_{\text{mesh}}^2}|n-m|\right)\right.\right.\\ &-\exp\left(-|n-m|\frac{l^2}{3R_{\text{mesh}}^2}\right)\operatorname{erf}\left(\frac{1}{3R_{\text{mesh}}^2}\sqrt{Wl^4t}-|n-m|\frac{l^2}{2\sqrt{Wl^4t}}\right)\\ &\left.\left.-\exp\left(|n-m|\frac{l^2}{3R_{\text{mesh}}^2}\right)\operatorname{erf}\left(\frac{1}{3R_{\text{mesh}}^2}\sqrt{Wl^4t}+|n-m|\frac{l^2}{2\sqrt{Wl^4t}}\right)\right)\right],\end{aligned} \tag{5.6}$$

with Wl^4 the Rouse rate, l the segment length, R_{mesh} the well parameter which corresponds to the radius of gyration of the single mesh and $\operatorname{erf}()$ the error function. With this MSD the dynamic structure factor can then easily be calculated according to eq. 2.19.

The Vilgis-Boué model only accounts for fluctuations of the branch point and does not include relaxation. Therefore, the dynamic structure factor obtained from equations 5.6 and 2.19 goes into a plateau. This plateau signifies the confinement of the branch point. As DTD will introduce a loss of confinement over time, the mesh size has to change over time, following the DTD renormalizations. The mesh size is related to the tube diameter with the following relation: $d = \sqrt{6 \cdot R_{\text{mesh}}^2}$. In order to account for the affect of DTD the following renormalization for eq.5.6 are done[2, 13, 14].

$$d^*(t) = d\varphi^{-\alpha/2}(t), \tag{5.7}$$

where $\varphi(t)$ is the tube survival probability and $\alpha = 1$ or $4/3$ is the dilution scaling exponent. The fits shown used $\alpha = 1$ as the scaling exponent but changing it to $\alpha = 4/3$ had basically negligible impact.

Knowing $d \sim R_{\text{mesh}}$ a renormalization of the mesh parameter

$$R_m^{*2} = R_m^2/\varphi^\alpha(t) \tag{5.8}$$

is performed and the monomer distance

$$|n-m|^* = |n-m| \cdot g(t) \cdot \varphi(t) \tag{5.9}$$

changes again with $\varphi(t)$ and additioally with $g(t)$. The function $g(t)$ is an additional slowly varying early tube dilation (ETD) function determined from simulations in the work of Hawke [65] and Bačová [37], starting out as 1 at time 0, it approaches 0.75 for times larger than 500 ns. It is needed to describe the diving modes in 3-arm symmetric stars as it slightly increases the mobility of the branch point and it was equally applied in the renormalization for the stars with higher functionality. The segment distance renormalization effect in eq. 5.9 is very small compared to the renormalization of the mesh size in eq. 5.8, it does only change the form of the graph at intermediate times (15 to 100 ns) and has no significant influence on the resulting mesh size in these systems.

For the tube survival probability the simulation results for the small stars are used which are fitted with a KWW function described in Section 5.5 with $\tau_K = 9.66 \times 10^4\ \tau_0$ and $\beta = 0.44$. As there are no large star simulations the theoretical tube survival probability equation for $Z_a = 13$ (see Section 5.5 and Figure 24) were fitted by a KWW with $\tau_K = 1.23 \times 10^6\ \tau_0$ and $\beta = 0.265$. For the calculation of the dynamic structure factor for branch point labeled stars, a few more approximations have to be made. $S(q,t)/S(q)$ is calculated only for the protonated label of the "backbone" as if they are linear chains. Including the third and forth arm in the calculations would need the inclustion of inter-arm correlations that are not known for every system. The value of the Rouse rate for linear chains is $Wl^4 = 7 \times 10^4\ \text{Å}^4 \text{ns}^{-1}$ [66], it is adjusted for stars with $3, 4$ and 5 arms with the corresponding factor $2/f$ [39, 40].

Now $S(q,t)/S(q)$ can be calculated with the mean square displacement that is dependent on the tube survival probability and also takes early tube dilution into account. This results in a dynamic structure factor that no longer goes into a full plateau but at longer times decreases. The NSE time scale is in both cases (small and large stars) well within the validity window of DTD. For $Z_a = 5$ this time is $t^* = 10^6\ \tau_0$, which corresponds to 3300 ns and for $Z_a = 13$ the dynamic tube dilution should theoretical be valid up to $t^* = 10^9\ \tau_0$ or 3.3×10^6 ns.

This theory with the bare, undilated tube parameter d as the sole fit parameter is now used to obtain theoretical curves to compare to the experimental $S(q,t)/S(q)$. The results can be seen in Figure 26 and 27.

A good description of the data (except the lowest q) is determined by only fitting the tube diameter d. All other parameter are fixed and the scaling of the Rouse rate with $2/f$ seems to be valid. Fitting the friction parameter additionally has no significant impact on the resulting fit and tube diameter. The observed decays in $S(q,t)/S(q)$ can be attributed to the dilation of the tube explored by the branch point.

Table 8 shows the obtained values for the tube diameter d. With around 35 ± 1 Å for the undilated confinement size in all measured stars the value is

Table 8: Effective initial tube diameter from NSE experiments and MD simulations.

sample:	NSE	MD
3-arm small	35.4 ± 0.2 Å	35.7 ± 0.2 Å
4-arm small	34.9 ± 0.2 Å	34.4 ± 0.2 Å
5-arm small		33.2 ± 0.2 Å
3-arm large	35.9 ± 0.2 Å	
4-arm large	36.2 ± 0.2 Å	

much smaller than the tube diameter for the linear polyethylene chain that lies at $d = 49$ Å [36]. Note, that both values have been obtained using two different theories with the modified Vilgis-Boué model for the PE stars and a standard tube model [1] for the linear PE. They are using different assumptions and an equivalence of the obtained tube diameters should not be expected.

Even though the differences between the individual stars is not very large, for the small stars a obvious tendency in both the simulations and the experiments results can be seen, which is that the bare tube diameter decreases with increasing functionality. This cannot be observed for the large stars as they were not directly simulated and the NSE results of the large 3- and 4-arm stars do not differ much from each other and a large difference in the resulting confinement d cannot be expected. With the new approach considering the effect of DTD we have obtained the undilated confinement size which is the initial or starting tube diameter before any relaxation effects. The value for the large 3-arm stars are also smaller than the effective confinement of 38 Å from previous measurements [39], with the same exact star polymer using the original Vilgis-Boué theory for fitting. The original model does not account for DTD which probably results in the higher effective tube diameter. Also the measurements now are extended to longer times (400 ns instead of 200 ns) where the the deviation from the plateau becomes more prominent.

5.6.4 *Theory applied to Simulations*

The modified Vilgis-Boué model can also be applied to the results from MD simulations. As the MD data has been rescaled to the experimental q values even a direct comparison of the fitted tube diameter is possible. The comparison of theory and simulations for all three stars with $f = 3, 4$ and 5 is shown in Figure 30 and the numerical values for the undilated tube d are listed in Table 8.

The d values provided by the fits are within the error bars of the corresponding NSE results as both are $d \approx 35$ Å. The results are obtained by fitting the theory in the time window of to NSE the experiments of up to 400 ns. For times larger than that the values were calculated from these obtained fits. One can see that within the NSE window all three different stars can be described very well. At longer times it becomes obvious that the theory does not match to higher functionality as nicely as it does for lower f. For 3-arm stars the match is pretty good up to around $t^* = 10^6\,\tau_0$ which is the validity regime of DTD [2] (see Section 5.5). After that the theoretical fit declines much faster than

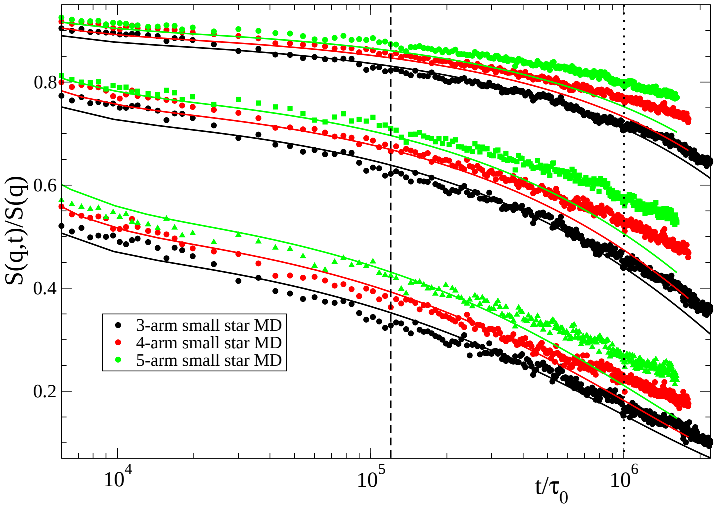

Figure 30: Dynamic structure factor of small 3-arm (red), 4-arm (blue) and 5-arm (green) stars. Symbols are the MD data. Lines are fits to the theory (Vilgis-Boué model with DTD), with $q\sigma = 0.28$ (circles), 0.43 (squares) and 0.54 (triangles), from top to bottom. These wave vectors correspond to the NSE values (in $Å^{-1}$) $q = 0.05$, 0.077 and 0.115, respectively. The vertical dashed and dotted lines indicate the time equivalent to the limit of the NSE window ($t_{NSE} = 400$ ns) and the limit of validity of DTD ($t^* = 3300$ ns), respectively.

the simulations. For $f = 4$ and 5 the theory starts to deviate already at earlier times $t > 3 \times 10^5\ \tau_0$ and $10^5\ \tau_0$ respectively. This overestimation of the tube widening is beyond the time window of the NSE (400 ns), but still within the validity window of DTD. The time frame of the experiments and the validity of the DTD is shown in Figure 30 with two dashed lines. The results are consistent with the observations from the MSD analysis in Section 5.3. Even though the tube survival probability was found to be independent of functionality, different behavior of the MSD and the $S(q,t)/S(q)$ functions are observed. The higher functionality stars ($f = 4$ and 5) relax slower than predicted and it shows that using solely DTD (even within its validity time frame $t < t^* = 10^6\ \tau_0$) to predict the behavior of star polymers is not sufficient or that DTD might have to be adjusted to account for functionality of stars.

6

ASYMMETRIC STARS - RESULTS AND DISCUSSION

The strong influence of entangled side chains on the dynamic of polymers is a known phenomenon and has been studied, often in the case of comb polymers with many "teeth" or with symmetric system with many arms. Asymmetric stars with short entangled side arm have been studied intensively [15]. Even a single side chain with just one entanglement length [57, 39] can have a large influence on the relaxation process. This chapter will focus on the transition to even shorter, non entangled side chains with arm lengths between 0.25 and 1 entanglement length and compare them to corresponding linear chains and symmetric stars. Asymmetric 3-arm stars with different backbone and side arm lengths have been simulated, for detailed geometries see Section 4.2.2. For some of the same geometries experiments were performed in the form of rheology and neutron spin echo spectroscopy.

In this chapter different aspects have been investigated to further understand the dynamics of asymmetric stars with unentangled side arm. The first part explores the MSD of the BP for different side arm lengths and different backbones from the simulations.

This data allows to determine the effective friction added by the short side arm and its relaxation times. Also the hopping fraction can be estimated.

This is followed by the results from the rheology experiments comparing the asymmetric stars to linear and symmetric counterparts. The influence of the hopping parameter on the theoretical description of the dynamic response as well as a viscosity analysis is shown. The last part is the evaluation of the dynamic structure factor for simulation and experimental data. Even though the simulations and experiments show good agreement with each other, no theoretical description for the behavior of the asymmetric stars could be found that fully describes the data. Different approaches for the theoretical description are discussed in the last part of this chapter.

6.1 SIMULATION RESULTS

6.1.1 *Mean square displacement*

A first step in analyzing the results of the simulations for asymmetric stars is to calculate the mean square displacement. Figure 31 shows the MSD $\langle r^2(t) \rangle$ of a linear label on the asymmetric stars with a backbone length of $Z_b = 10$ entanglements and the linear chain of the same length. The label is placed on the backbone and the length of 13 simulation beads centered at the BP or center point. Its length is equal to roughly $1/2$ an entanglement length to create good enough statistics for the evaluation. The length of the short unentangled sidearm varies from $Z_a = 0.25$ to 1 in steps of $1/4$ entanglement and in the resulting MSD one can easily see the differences between the five different polymers. At early times they start out identical with $< r^2 > \sim t^{0.6}$

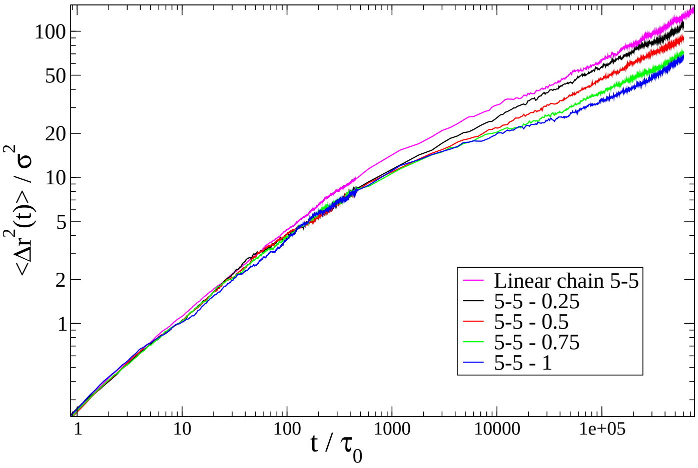

Figure 31: Mean square displacement of linear chain and asymmetric stars with backbones of $Z = 10$ entanglements.

and the linear chain follows the same behavior as already described in Figure 14. At times of about $2000\,\tau_0$ which is close to the entanglement time of $\tau_e = 1800\,\tau_0$, the MSD of the four asymmetric stars start to split up and one can see that the slowdown in the MSD is stronger the longer the side arms, as expected. They need different amounts of time to reach the reptation along the tube regime, where they have again the same time exponent of $t^{0.5}$ and run parallel to each other with the stars with longer side arm being below the ones with shorter or no arm. The same behavior was observed for the asymmetric stars with longer backbone of $Z_b = 16$ with slightly lower values for the $t^{0.5}$ region where they run parallel as they generally are slower than their shorter counterparts.

6.1.2 *Reptation Plateau*

The reptation plateau is obtained when the mean square displacement divided by $t^{0.5}$ is plotted and reaches a plateau. This is needed to calculate the diffusivity (see Section 2.3.1)

$$D = \frac{\pi}{4d^2}\left(\frac{\langle r^2\rangle}{t^{1/2}}\right)^2 \tag{6.1}$$

directly from the motion of the branch point [57] with the part inside the brackets $\frac{\langle r^2\rangle}{t^{1/2}} = G$ that is called the plateau height. At times roughly $t > 4 \cdot 10^5\,\tau_0$ the stars reach their plateau region. The plateau value is calculated by averaging over the time region, where the curves are flat between $4 \cdot 10^5\,\tau_0$ and $10^6\,\tau_0$, depending on the individual star. The error is calculated by obtaining the standard deviation of the plateau values. The reptation plateaus are shown for the example of the asymmetric stars with backbone length of $Z_b = 10$ entanglements in Figure 32. The values for the plateau heights for these and the stars with backbone length of $Z_b = 16$ can be found in Table 9. The reptation plateau is used to calculate the side arm friction that should be independent of the backbone. It is also needed for the calculation of the "hopping parameter" p^2 in Section 6.1.5.

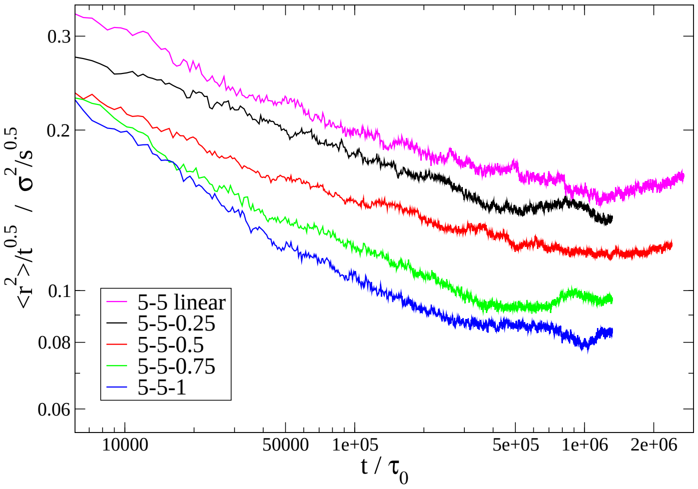

Figure 32: Region of the reptation along the tube for the Mean Square Displacement divided by $t^{1/2}$ for the asymmetric 3-arm stars with 10 entanglement backbone length and side arm lengths between 0.25 and 1 entanglements as well as the linear chain.

6.1.3 *Side Arm Friction*

To evaluate the additional friction F_{arm} that a short unentangled side arm adds to the backbone friction of a linear polymer the following procedure is used to normalize to the linear chain. This is a alternative way to represent the data with several approximations and does not have strong physical significance.

$$\frac{D_{star}}{D_{lin}} = \frac{G_{star}^2 \cdot d_{lin}^2}{G_{lin}^2 \cdot d_{star}^2}, \tag{6.2}$$

using eq. 6.1, D the diffusivity along the tube, G as the plateau height value and d the tube diameter of the different polymers. In a first approximation we set the tube diameters to the same values as we do not have the diameters for the individual stars. Knowing that the diffusivity D is inverse proportional to the polymer friction [67] as $D \propto \frac{1}{F}$, the relationship between the friction and the plateau values becomes

$$\frac{F_{star}}{F_{lin}} \propto \frac{G_{lin}^2}{G_{star}^2}. \tag{6.3}$$

The goal of these approximations is to find the friction that is added to the linear chain by the short side arm, so with $F_{star} = F_{backbone} + F_{arm}$ the final relationship between arm friction and the measured plateau height becomes

$$H_{eff} = 1 + \frac{F_{arm}}{F_{lin}} \propto \frac{G_{lin}^2}{G_{star}^2}. \tag{6.4}$$

H_{eff} is the effective friction normalized to the linear chain. A linear chain with no side arm has $H_{\text{eff}} = 1$ and the values increases proportional to the friction provided by the short side arm. The resulting values for plateau height G and H_{eff} for the two different backbone lengths are listed in Table 9 with the values for the plateau height of the stars with side arm longer than one entanglement on the backbone $Z_b = 16$ used from the publication of Bačová *et al.*[57].

Table 9: Plateau heights from the MSD divided by $t^{1/2}$ for the asymmetric stars with short side arms (G). Proportional effective friction added by the side arm for the same stars (H_{eff}). Values with * have been taken from Bačová *et al.*[57] to expand the data with values for longer sidearms.

Z_{arm}	plateau height G $Z_b = 10$	plateau height G $Z_B = 16$	H_{eff} $Z_b = 10$	H_{eff} $Z_b = 16$
0	0.157 ± 0.005	0.136 ± 0.007	1	1
0.25	0.142 ± 0.004	0.124 ± 0.004	1.22 ± 0.11	1.2 ± 0.16
0.5	0.119 ± 0.002	0.116 ± 0.003	1.74 ± 0.14	1.37 ± 0.18
0.75	0.096 ± 0.002	0.084 ± 0.003	2.67 ± 0.22	2.68 ± 0.38
1	0.084 ± 0.003	$0.066^{*} \pm 0.003$	3.49 ± 0.35	4.12 ± 0.78
2	-	$0.031^{*} \pm 0.001$	-	19.2 ± 2.7
3	-	$0.023^{*} \pm 0.001$	-	34.9 ± 5.3

To check the dependence of the effective friciton on the side arm length, it is plotted for the two different backbone lengths against the respective length of the arm in Figure 33 and fitted with a quadratic function $H_{\text{eff}} = x \cdot Z_a^2 + 1$ with $x \approx 3$. This matches the data for side arm lengths smaller and equal to 1 entanglement but fails for the longer ones ($Z_a = 2$ and 3) as the friction increases much faster with the length of the side arm than a quadratic function. This is to be expected as the side arm friction should behave similar to the arm relaxation time in its dependence on arm length (see Section 6.1.4). For short unentangled chains the arm relaxation time τ_{relax} is quadratic in its length dependence. The friction seems independent on the length of the backbone chain once normalized by the friction of the backbone linear chain in the two simulated examples. Both types of polymers seem long enough to follow the hierarchical relaxation behavior described in Section 2.3.1 were the short side arm relaxes into a "friction bead" and the backbone can reptate along the tube.

6.1.4 *Relaxation of Short Arm*

To calculate the relaxation times τ_{relax} of the short side arms of the asymmetric stars the end-to-end correlation function [57] is used. It is defined as

$$C(t) = \frac{\left\langle \vec{R}(t) \cdot \vec{R}(t_0) \right\rangle}{R^2(t)}, \tag{6.5}$$

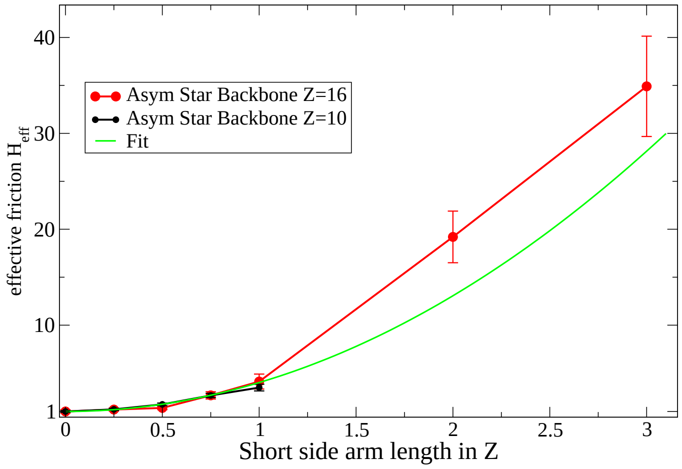

Figure 33: Effective friction H_{eff} created by the side arm of the asymmetric star for the two different simulated backbone length, normalized to corresponding linear chain. $Z_b = 10$ (black) and $Z_b = 16$ (red) with a quadratic fit $F = 3.0 \cdot Z_a^2 + 1$ (green).

with $\vec{R}(t)$ and $\vec{R}(t_0)$ the end-to-end vectors of the side arm at the times t and t_0. When the correlation function in Figure 34 is zero it means that the short side arm is fully relaxed. There are two commonly used definitions when a polymer is said to have relaxed, one is when the correlation function is 0.1 which is called the "longest" relaxation time and the second one is when the function is $1/e$ with e as Euler's number.

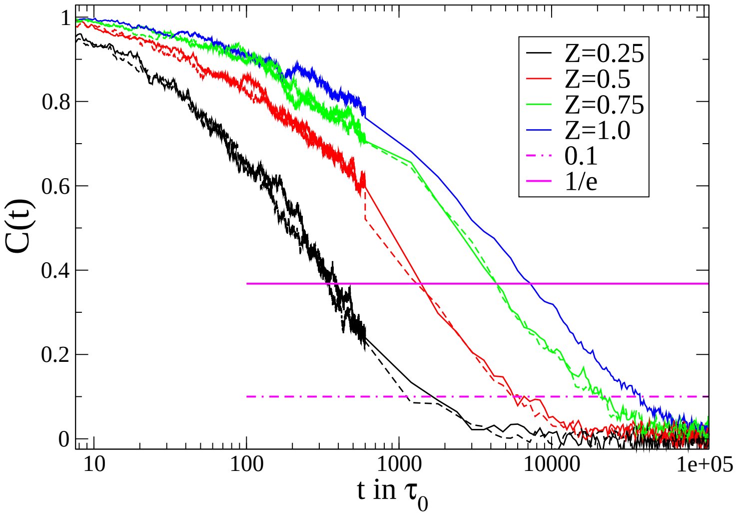

Figure 34: Relaxation of short side arms for the asymmetric stars with backbone length of $Z_b = 10$ (solid lines) and $Z_b = 16$ (dashed lines) with short arm length between $Z_a = 0.25$ and 1 in steps of 0.25. The horizontal lines mark values of 0.1 and $1/e$.

The calculated values for both can be found in Table 10. They are obtained by fitting the relaxation with a KWW function and calculating the values for

$C(t) = 0.1$ and $1/e$. The theoretical prediction for the Rouse time is also found in the table. For unentangled ($Z_a < 1$) polymers that are fixed on one chain end the Rouse time is in the first approximation four times the Rouse rate of the free linear chain

$$\tau_{\text{relax}} = 4 \cdot \tau_e \cdot Z_a^2, \tag{6.6}$$

with the entanglement time $\tau_e = 1800\,\tau_0$ and Z_a the length of the short arm. The fact that the chain is basically fixed in place at the branch point, where it is connected to the backbone polymer contributes the factor 4 to the standard Rouse time approximation. The comparison of both calculated and theoretical values can be found in Figure 35. The $1/e$ relaxation times are in decent agreement with the Rouse time expectation.

Table 10: Short arm relaxation times for the simulated asymmetric stars with backbone length of $Z_b = 10$ and $Z_b = 16$ for relaxation to $1/e$ and 0.1 and the prediction by the Rouse theory.

Z_a side arm	$\tau_{\text{relax}}(0.1)$ in τ_0	$\tau_{\text{relax}}(1/e)$ in τ_0	Rouse prediction in τ_0
	Star with $Z_b = 10$ backbone		
0.25	1600 ± 200	400 ± 70	450
0.5	6000 ± 500	1400 ± 200	1800
0.75	21500 ± 3000	4300 ± 200	4050
1	37000 ± 5000	7400 ± 200	7200
	Star with $Z_b = 16$ backbone		
0.25	1400 ± 200	350 ± 80	450
0.5	6000 ± 500	1400 ± 200	1800
0.75	20500 ± 3000	4300 ± 400	4050
	$Z_b = 16$ longer side arm from literature [57]		
1	37000 ± 9000	-	-
2	439000 ± 65000	-	-
3	2133000 ± 507000	-	-

This validates the quadratic dependence of the Rouse relaxation time on the arm length for short unentangled chains. This quadratic behavior does not apply for chains longer than one entanglement and the arm takes much longer to relax. This can be seen by comparing the data of the star with backbone of $Z_b = 16$ with data from literature [57] for stars with longer side arm with $Z_a = 1, 2, 3$ (see Table 10). The increase in relaxation time is obviously not quadratic anymore for $Z_a > 1$ and slows down rapidly for more entangled chains.

6.1.5 *Hopping parameter calculation*

The dimensionless hopping parameter p^2 gives the mean distance the branch point is assumed to move as a fraction of the tube diameter (pd) after the

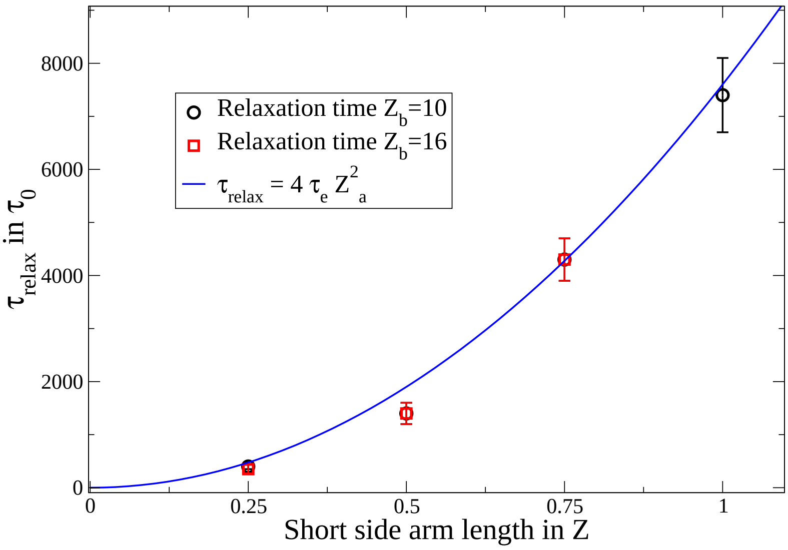

Figure 35: $1/e$ relaxation times of short side arms for the asymmetric stars with backbone length of $Z_b = 10$ (black) and $Z_b = 16$ (red). Theoretical relaxation time fitted (blue).

relaxation time of the short arm τ_{relax}. p is supposed to be one, but in rheology was found to be much smaller for short (but still entangled) arms. Here p shall be determined by the following calculation from Ref. [57] for the results of the simulations on asymmetric stars with very short unentangled side arms.

Starting with the equation for the diffusivity as introduced and explained in Section 6.1.2

$$D = \frac{\pi}{4d^2}\left(\frac{\langle r^2\rangle}{t^{1/2}}\right)^2, \tag{6.7}$$

and combining it with the expression for it from Ref. [7] which includes the time dependent diluted tube diameter d_h. For a diluted tube the branch point needs to cover a smaller distance along the primitive tube path but the actual distance covered is set by the time scale of the short side arm retraction τ_{relax}. This expression is given by

$$D = \frac{p^2 d_h^4}{2\tau_{relax} d^2} \tag{6.8}$$

where d_h can be either the undiluted tube diameter $d_h = d$ or the diluted one $d_h^2 = d^2/\varphi^\alpha$ with φ the tube survival probability and τ_{relax} is the short arm relaxation time. This leads to an expression for the hopping parameter:

$$p^2 = \frac{\pi\tau_{relax}}{2d_h^4}\left(\frac{\langle r^2\rangle}{t^{1/2}}\right)^2. \tag{6.9}$$

This equation however does not take the friction of the backbone into account. The more general expression that includes the backbone friction is given by

$$p^2 = \frac{2d^4\pi\tau_{\text{relax}}}{d_h^4}\left[\frac{\left(\frac{\langle r^2\rangle}{t^{1/2}}\right)^2}{4d^4 - 3\pi^3\tau_e Z_b\left(\frac{\langle r^2\rangle}{t^{1/2}}\right)^2}\right]. \tag{6.10}$$

Here Z_b is the backbone length. The results for the p^2 calculations from the MSD data of the MD simulations are shown in Figure 36. The calculations were made with the 0.1 relaxation time for the short side arm to keep consistent with the literature results. Using the $1/e$ value for the relaxation time decreases the p values for the unentangled side arm significantly, making them between three and five times smaller. Using this relaxation time does not omit the failure of the description once backbone friction is included. The tube survival probability was approximated with

$$\varphi_{\text{approx}} = \frac{Z_{\text{star}} - 3Z_a}{Z_{\text{star}}} \tag{6.11}$$

with Z_{star} the amount of material of the complete star in number of entanglements. This approximation assumes that the star relaxes at the same speed from each open end.

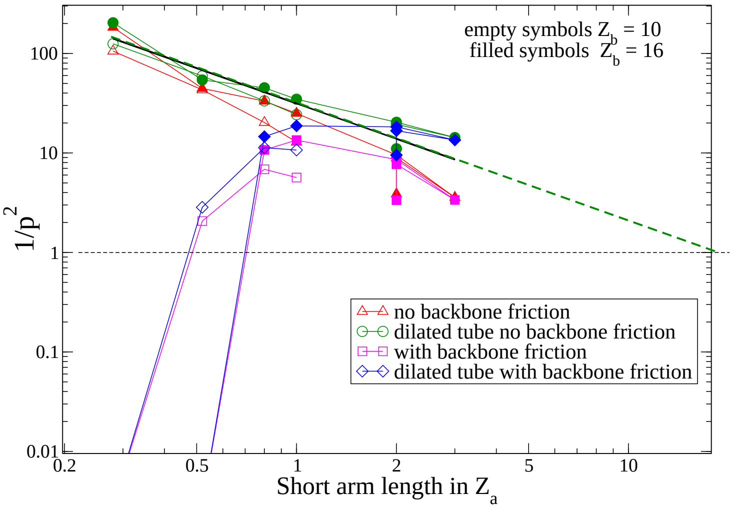

Figure 36: Hopping parameter plotted as $1/p^2$ for asymmetric stars with backbone length of $Z_b = 10$ and $Z_b = 16$ with short side arms between $Z_a = 0.25$ and $Z_a = 3$. $\alpha = 4/3$ for the dilated tube and 1 otherwise. The results for the stars with short arm larger than 1 are taken from Bačová *et al.*[37].

Without backbone friction, (green and red symbols) the results would show that for very short side arms the factor p^2 becomes very small in the orders of $1/40$ to $1/200$ and for longer side arms ($Z_a > 1$) the fit (dashed line) comes close to the expectation of a value of unity for very long arms. The calculation however fails completely for $Z_a < 0.75$ if backbone friction is taken into account (blue and pink symbols) and the results are no longer valid. This makes the theory not universal for all lengths of short side arms even if it gives a rather good description for entangled ones [15, 57]. In the rheological experiments on the asymmetric stars (see Section 6.2) it is also found that the p^2 value loses most of its relevance for very short ($Z_a < 1$) side arms. This makes the failure of theoretical description of the parameter for these cases less important.

The analysis of the simulation results showed that the effective friction that is a added by the short unentangled side arm is even for these very short side chains significant and increases quadratic with the arm length. The short arm relaxation times follow as expected in first approximation the Rouse relaxation times behavior for chains that only have one free end. These relaxation times are also observed as independent of backbone length. The approach for obtain the hopping parameter from the calculated MSD data only obtains functional results as long as backbone friction is not taken into account. As a result this approach is not fully applicable for unentangled side arms.

6.2 RHEOLOGY

Rheological measurements have been performed on the different asymmetric PB star polymers and linear chains to study the influence of short unentangled side chains on the dynamic response to the strain γ. The theory to describe the asymmetrical star data is the model by Frischknecht *et al.* [15] and is described in Section 3.4.

In addition to the already shown symmetric polymer stars in Section 5.2 the storage and loss modulus of the Asym S-1.0 star and three linear PB chains of different lengths have been measured. The measurements are in part compared to data from already published stars [39] and two unpublished data sets for large asymmetric stars with short side chains with $Z_a = 0.3$ and 0.5 also provided by Zamponi *et al.* (see Table 2). The experimental data is shifted to 25°C room temperature. The theoretical models have been calculated using a Maple script with the following input variables.

The backbone arm length and the short side arm length, were taken from the synthesis and the plateau modulus G_0 and the entanglement time τ_e were fitted. The dilution exponent α was set to $4/3$, the entanglement mass $M_e = 1900$ g/mol as in the model for the symmetric stars. The final fit results can be found in Table 11. Note that the Asym L-0.5 have values that deviate strongly from the others probably due to problems during the measurement or the temperature matching. As the curves are basically only shifted, they can still be used to analyze the form of the dynamic response and the fit of the hopping parameter p^2.

Comparing the storage and loss modulus of symmetric and asymmetric stars shows if and how pronounced the polymers demonstrate the typical characteristic spectrum of branched systems. Therefore Figure 37 shows the measurements on the new short 3-arm small and Asym S-1.0 polymers.

The symmetric star has 3 arms of $Z = 5$ which is equal to the two long arms of the asymmetric star. The short arm of the asymmetric star is $Z_a = 1$. The Asym S-1.0 had to be adjusted in ω-direction to exactly match the Rouse

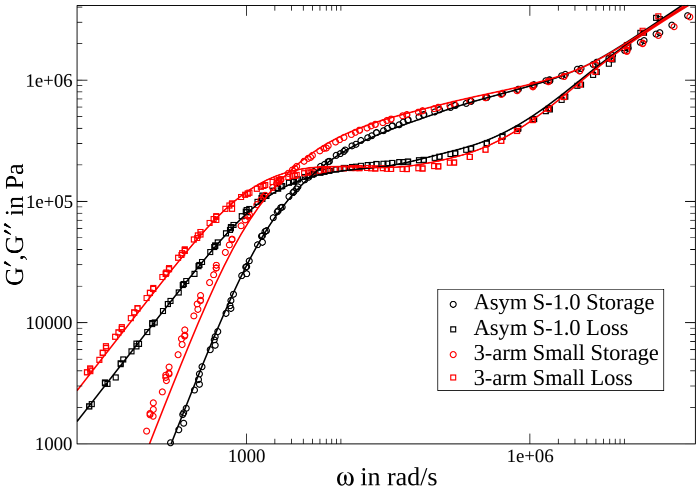

Figure 37: G'' loss- and G' storage-modulus measured for symmetric and asymmetric stars at reference temperature 25°C. Asym S-1.0 (black symbols) with $p^2 = 1/60$ and 3-arm small (red symbols). Fitted with the theory of Frischknecht *et al.* [15] lines.

Table 11: Rheology parameters for asymmetric polybutadiene stars. All stars have the same $\alpha = 4/3$, $p^2 = 1/60$ and M_e = 1900 g/mol.

sample:	τ_e in s	G_0 in Pa
Asym L-0.3	0.20×10^{-6}	0.95×10^{-6}
Asym L-0.5	0.90×10^{-6}	0.75×10^{-6}
Asym L-1.0	0.20×10^{-6}	1.0×10^{-6}
Asym S-1.0	0.30×10^{-6}	1.1×10^{-6}

region of the symmetric counterpart. The difference between the symmetric and asymmetric star is not as pronounced as for the much larger stars found by Zamponi *et al.* [39] but still easily observable. The asymmetric star shows a much weaker or less pronounced plateau region that is also over a smaller time regime than the plateau of the symmetric counterpart. The theoretical fit using the theory of Frischknecht *et al.* matches the data very well at all parts of the frequency spectrum, much better as for the larger stars in the already mentioned literature. The values for τ_e and G_0 are also comparable with the results from symmetric stars once adjusted for the shift to match the Rouse regime. The value of G_0 is close to the literature values for polybutadiene of 1.15×10^{-6} Pa [61].

Figure 38 shows the comparison of a linear polybutadiene chain with $Z = 6.3$ with the Asym S-1.0 star. The linear chain is significantly shorter than the backbone but nevertheless one can compare the form of the storage and loss modulus. The typical plateau or shoulder of branched polymers is barely visible in the asymmetric star and it looks quite similar to the linear chain.

The rheology of asymmetric stars was investigated by Frischknecht *et al.* [15] and it can be described dependent on the hopping parameter p^2 in their theory. For stars with a short side arm of only a few entanglements they found

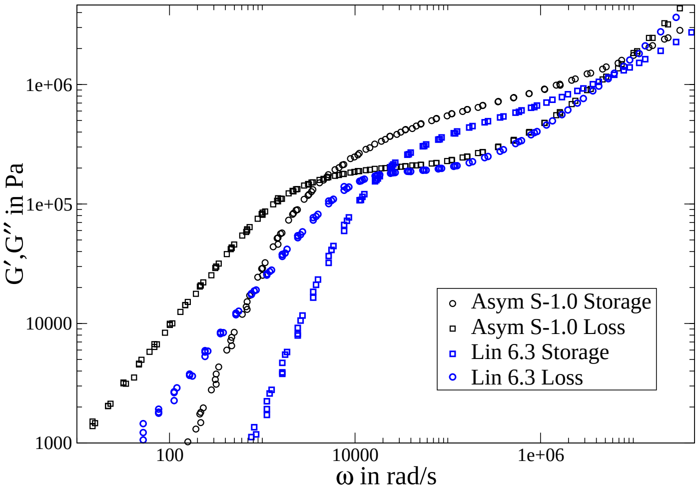

Figure 38: G'' loss- and G' storage-modulus measured for asymmetric stars (black symbols) and linear chain (blue symbols) ($Z = 6.3$) at reference temperature 25°C.

p^2 to be very low. Here now in rheological measurements of asymmetric stars with $Z_a < 1$ it shows a interesting behavior. Two different asymmetric stars with very small Z_a are shown in Figure 39. The theoretical model (Frischknecht) matching them is shown with different p^2 values between 1 and 1/60. The figures only show the data for the low ω region to highlight the differences between the different p^2 plots.

The difference between the two stars and the p^2 dependence of the matching theory is quite obvious. Changing this parameter in the theoretical model for the long asymmetric star Asym L-0.3 with very short unentangled side arm of only 0.3 M_e, it has almost no influence on the form of the plot. While a small value of $p^2 = 1/60$ achieves the best fit for the measured data, even going as far as changing it to 1 still generates adequate graphs that describe the data reasonably well. The plots for the different p^2 values are so similar that even with the zoomed Figure 39 they are barely distinguishable.

This is in strong contrast to the plots for the smaller star Asym S-1.0 with a still unentangled side arm of length $Z_a = 1$ or about 2 kg/mol. There again a small value of $p^2 = 1/40$ creates the best description, but once going higher than 1/10, the shift from the small p^2 graph becomes too large and the data for low frequencies are not described by the theory anymore. A very similar behavior to changes in p^2 could be observed for a large asymmetric star Asym L-1.0 (backbone length 54 kg/mol) with the same side arm of length 2 kg/mol. The theoretical model showed a strong dependence on p^2 very similar to the one shown in Figure 39 bottom graph. This leads to the assumption that p^2 is only strongly dependent on the length of the short side arm without a direct dependence on backbone length.

Testing the dependence on p^2 with different side arm length showed that for very short arms $Z_a < 1$, the hopping parameter becomes less important and can be chosen at any value smaller or equal to one with no changes to the

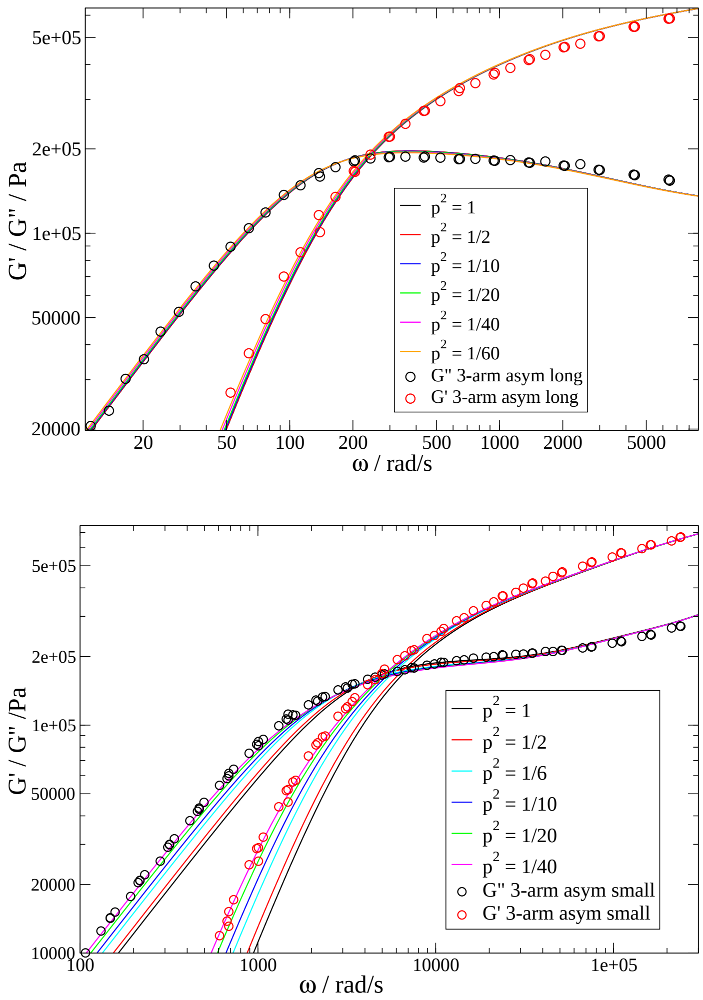

Figure 39: G'' Loss- and G' storage-modulus measured (symbols) for asymmetric star L-0.3 (top) and S-1.0 (bottom) with theoretical model (lines) shifted to 25°C. Theory plotted for different values of p^2 between 1 and $1/60$

Rouse regime and only minor changes in the transition to flow and the viscous frequency regime. However, if the short side arm is of length $Z_a = 1$, the parameter p^2 still has to be set to a small values of less than $1/10$ for the theory to describe the data. Comparing this to the p^2 values from the simulations it is interesting to note that for $Z_a < 1$ the description either produced very small values between $1/10$ and $1/100$ or failed to give applicable results once the backbone friction was included into the calculations. For $Z_a = 1$ the theoretical description was still valid and resulted in values of p^2 between $1/6$ for the undiluted tube including backbone friction and $1/35$ for the dilated tube without backbone friction included. These two values are within the validity window in Frischknecht theory for the asymmetric stars looking at Figure 39 as they give a reasonable description for the data.

As seen in Section 5.2, rheology also allows the measurement of the viscosity of polymers and this was also done for the asymmetric polymer stars and the three different linear PB chains. The results are shown in Table 12 and taken from Figure 41.

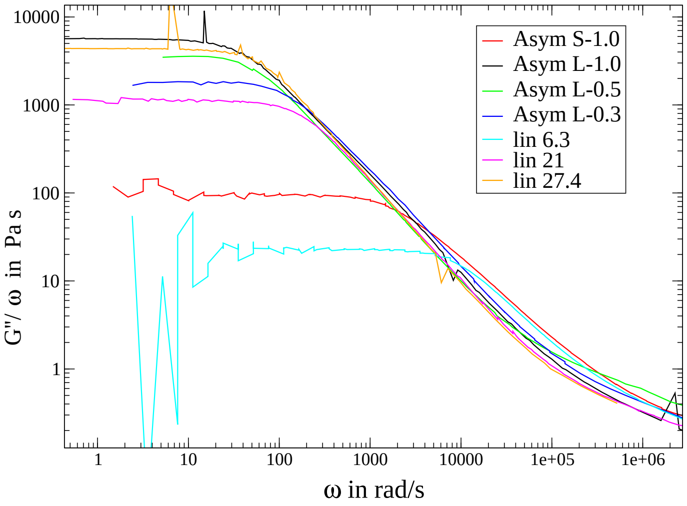

Figure 40: G''/ω for the asymmetric stars and linear chains. The viscosity can be read off the plateau part at low frequencies.

It is known from theory [30] that the melt viscosity η of linear polymers scales with the molecular weight and is described by the power law $\eta_0 \propto M^{3.4}$ and the measured linear chains confirm this as well which can be seen in Figure 41 where the red symbols represent the linear chains that roughly match the $Z^{3.4}$.

For the asymmetric stars there is no known scaling for the viscosity relation to either backbone length or side arm length. It is nevertheless not too surprising that they roughly follow a similar scaling as the linear chains. Their typical flow behavior is more similar to a linear chain of similar length as their backbone than a symmetric star (see again Figure 41 black symbols). A scaling factor cannot be obtained from the measured samples. The small side arm have obvious influence on the viscosity behavior but because the lengths of the arms are not consistent for all stars it is not possible to find a direct dependence. There is only a single star pair with the same exact side arm length that can directly be compared to each other, but this is not enough data to give a meaningful result for viscosity scaling of asymmetric stars. As the viscosity measurement is basically a measurement of the position of the low frequency part of G''/ω of the rheological data it has the same dependence on the accuracy of the data shift as the other results which explains the inaccuracy for the Asym L-0.5 star that should have a lower viscosity and the Asym L-0.3 that should have a higher one, to be more similar to each other, see earlier discussion.

The rheological experiments compared the short ($Z = 5$) asymmetric star with their symmetric counterpart and linear chain. The results show that unlike the experiments on much larger ($Z = 13$) [39] they behave much closer to linear chains than to stars. The viscosity scaling with backbone length is similar and the storage and loss modulus also are closer to those of linear chains in their general appearance. It was also observed that for very short ($Z_a = 0.5$) side arms the hopping parameter p^2 becomes quasi irrelevant for

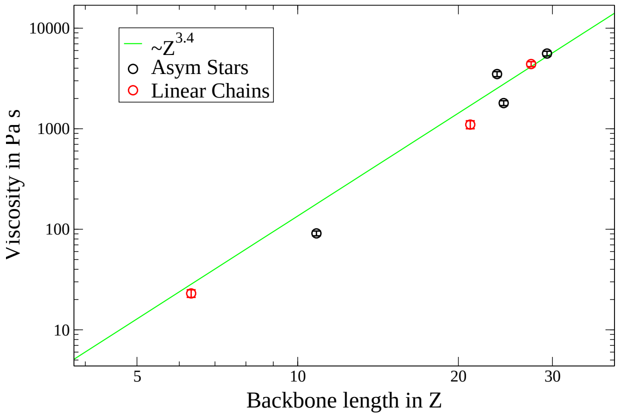

Figure 41: Viscosity of the linear chains and the asymmetric stars dependent on the backbone length in Z. Red symbols are the linear chains, black symbols are the different asymmetric stars and the green line is the theoretical scaling with length $\propto Z^{3.4}$[30].

Table 12: Viscosity for the different asymmetric PB stars and linear chains.

System	Viscosity η in Pa s	backbone length in kg/mol
Asym L-0.3	1800 ± 100	46.2
Asym L-0.5	3500 ± 200	44.9
Asym L-1.0	5600 ± 300	55.7
Asym S-1.0	91 ± 5	20.6
lin 6.3	23 ± 2	12
lin 21	1100 ± 100	40
lin 27.4	4400 ± 250	52

the theoretical description of the experimental data even though the theory is still sensitive to the parameter for $Z_a = 1$.

6.3 DYNAMIC STRUCTURE FACTOR

Neutron spin echo spectroscopy was performed to measure the dynamic structure factor, in this case for the asymmetric 3-arm polymer star with linear backbone of $Z_b = 10$ and a short side arm of $Z_a = 1$ with a protonated label of the same size as the symmetric 3- and 4-arm stars of 1 kg/mol on three arms stemming from the branch point. The measurements were made to times up to around 400 ns and at q values between $q = 0.05\,\text{Å}^{-1}$ and $0.115\,\text{Å}^{-1}$. The experiments were also performed at the same temperature at 509 K to compare the stars in their melt condition.

Figure 42 shows the normalized dynamic structure factor $S(q,t)/S(q)$ of the Asym S-1.0 star with its corresponding MD simulation data. The solid lines represent the structure factor gained from the MD simulations that has again been scaled to the experimental time and tube diameter (see Section 5.6.2).

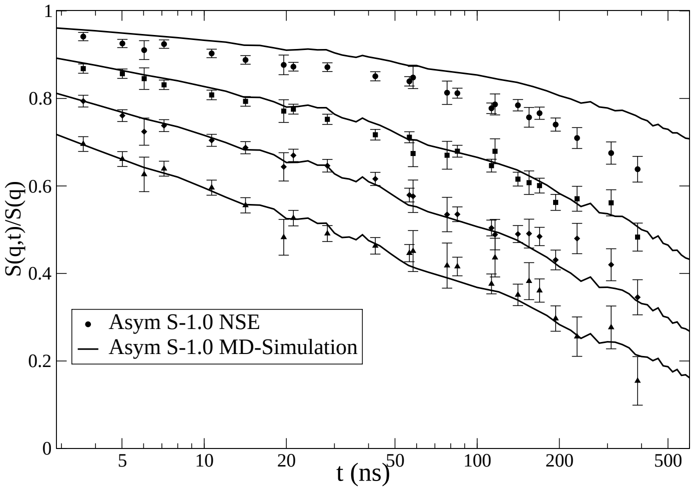

Figure 42: Dynamic structure factor measured with NSE spectroscopy (symbols) and calculated from MD simulations (solid lines) for the Asym S-1.0 star with backbone length $Z_b = 10$ and short side arm of $Z_a = 1$. The q values are $0.05\,\text{Å}^{-1}$, $0.077\,\text{Å}^{-1}$, $0.096\,\text{Å}^{-1}$ and $0.115\,\text{Å}^{-1}$ from top to bottom.

For the time scaling the same factor ($\gamma_t = 7/2100$ ns) has been used. In order to obtain better agreement for the larger q vales, the γ_q scaling factor was slightly adjusted to $\gamma_q = 47/8.75\,\text{Å}/\sigma = 5.4\,\text{Å}/\sigma$ instead of $5.6\,\text{Å}/\sigma$ (for the symmetric stars). This mapping gives good agreement of simulations and experiment for all q except the lowest one that, as already discussed in Section 5.6.2 shows a stronger decay in the experiments than the simulations (and theoretical descriptions) for all measured stars independent of their individual geometry.

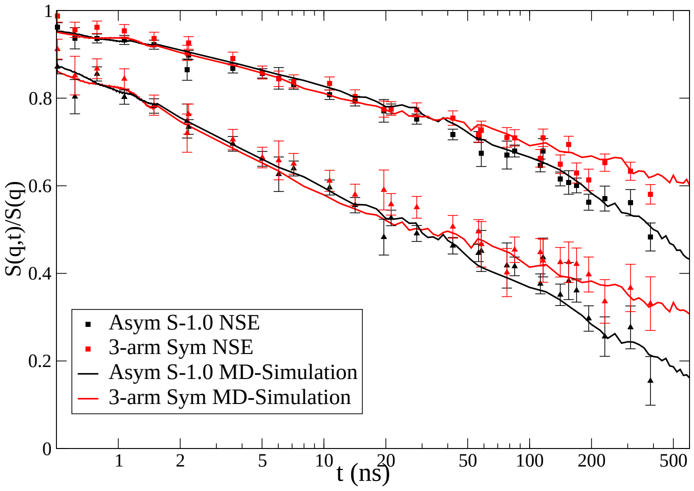

Figure 43: Dynamic structure factor comparison between 3-arm Sym small (red) and Asym S-1.0 (black) stars. Lines: MD simulation results, Symbols: NSE results. The q values are $0.077\,\text{Å}^{-1}$ and $0.115\,\text{Å}^{-1}$ from top to bottom.

In Figure 43 the direct comparison of the asymmetric star with the corresponding symmetric star is shown and for better visibility only two q values, $0.077\,\text{Å}^{-1}$ and $0.115\,\text{Å}^{-1}$ are plotted.

Comparing the two different systems of symmetric and asymmetric stars one can see that up to times of 20 to 40 ns both stars show almost identical decay. After that, the dynamic structure factor of the symmetric star levels off, whereas the one of the asymmetric star shows a stronger decay. This time window, where they start to diverge from each other is in agreement with the short arm relaxation time of $7400\,\tau_0 \mathrel{\hat{=}} 25$ ns that was obtained from the simulations in Section 6.1.4. This would be in agreement with the notion that once the short side arm of an asymmetric star has fully relaxed the BP can move along the tube of the backbone chain, whereas the BP in the symmetric case is more localized.

The $S(q/t)/S(q)$ to which the systems decay differ significantly by the time they reach the 500 ns which is the longest the NSE spectroscopy can reach. The symmetric star (both NSE and MD) at $q = 0.077\,\text{Å}^{-1}$ decay to roughly 0.6, whereas the asymmetric star with the same q decays to 0.45. Similar patterns can be observed for the other q values. This means that the branch point of the asymmetric star has a significant higher mobility than the one of the symmetric star of same "backbone length". This is a quite interesting result compared to previous measurements with symmetric and asymmetric 3-arm stars [39]. These measurements with much longer arms ($Z_a = 13$ which equals a backbone length of $Z_b = 26$ for the asymmetric star with a short side arm of one entanglement length) showed only a minor difference in the mobility of the two systems and the dynamic structure factor for both large stars were going into a plateau. An explanation for this would be that the influence of the tube survival probability is significantly stronger for smaller stars than for their larger counterparts. Further discussion can be found in Section 6.3.2

In order to describe the stronger decay and higher mobility of the asymmetric star several contributing factors are considered. The faster decay of the tube survival probability (see Section 5.5) and center of mass diffusion for the on-setting diffusion along the backbone tube that is not possible for the symmetric systems.

6.3.1 *Center of Mass Diffusion*

The increased mobility of the short asymmetric star might be partially explained by the contribution of the center of mass diffusion (CMD) that is happening at a much higher rate for small and especially asymmetric stars than it does for symmetric and larger asymmetric ones. To show the influence of CMD it was calculated from the simulation data and plotted together with the branch point mean square displacement in Figure 44 to compare the magnitude and importance of both. One can easily see in the plot, that for the largest part of the NSE time window the CMD is orders of magnitude lower than the MSD and has therefore a very little influence on the mobility of the system. At about 400 ns, which is roughly the extent of the experimental NSE time window, it is in all four cases still only about 1/3 of the MSD value. The numerical CMD values of the Asym S-1.0 star are roughly 50% higher than the corresponding 3-arm symmetric star of same arm length. The CMD generally shows an expected sub-diffusive behavior of

$$\left\langle r^2(t) \right\rangle_{\text{CMD}} = 6Dt^{\kappa} \tag{6.12}$$

at relevant NSE experimental times $t < 400$ ns, with D the diffusion coefficient and κ an exponent that is < 1 for sub-diffusion for the different simulated stars in the NSE time window, κ varies between 0.55 and 0.59.

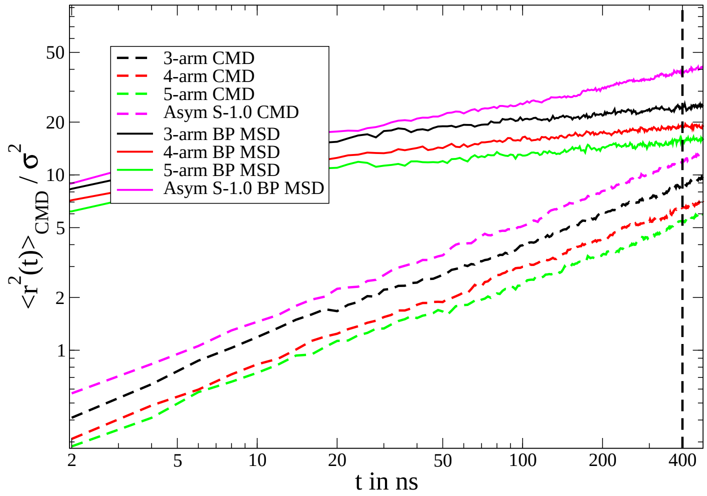

Figure 44: BP Mean Square Displacement and Center of Mass Diffusion of the simulated symmetric stars and the asymmetric S-1.0 star. 3-arm in black, 4-arm in red, 5-arm in green and Asym S-1.0 in magenta. The MSD of the BP is plotted as solid lines and the CMD is plotted as dashed lines. The NSE time window of 400 ns is marked with a vertical black dashed line.

At later times larger than 400 ns the diffusive behavior of the polymer changes, where for the NSE time window the exponent is more or less constant (see Figure 44), it increases at longer times which can be seen in Figure 45, where the linear chain and the corresponding 3-arm symmetric and asymmetric stars are shown with their CMD. The fits were done for times larger than 3500 ns. At these long times the CMD of the linear chain is basically no longer sub-diffusive as the exponent κ is almost equal to 1, paired with a very small diffusion coefficient relative to the values of sub-diffusive D. The 3-arm star only reaches an exponent κ of 0.50 for similar times. The fit for the CMD of the Asym S-1.0 results in values of $0.256t^{0.64}$ which are still far below the diffusive regime. This shows that a branched system will take significantly longer to reach normal diffusive behavior. This cannot be simulated within a reasonable time frame with the used methods.

The diffusion constant $D = 1/6 \cdot 0.034\,\sigma^2/$ ns of the linear chain was calculated by fitting at long times and converted to Å^2/ns by multiplying it by the squared scaling factor for the tube diameter 5.6^2. This results in $D = 0.178\,\text{Å}^2/\text{ns} = 1.78 \times 10^{-8}$ cm^2/s which is consistent with results from Pearson *et al.* [68] for linear Polyethylene chains. As normal diffusion is not reached for the star systems, it is not possible to compare the simulations with differently obtained diffusion coefficients for star systems from literature. The inclusion of the CMD in the description of the dynamic structure factor of the asymmetric star is shown in Section 6.3.2. When the diffusion is implemented as obtained from the CMD fits (even without inclusion of DTD), it overestimates the dynamics at longer times (outside of NSE window), therefore the diffusion coefficient was fitted where it was applied to the dynamic structure factor. For the symmetric stars the diffusion contribution should also be smaller as there is no reptation possible and including it in the Vilgis-Boué model that already includes DTD would not be reasonable as it is probably already contains part of the diffusion effect in the dilution theory.

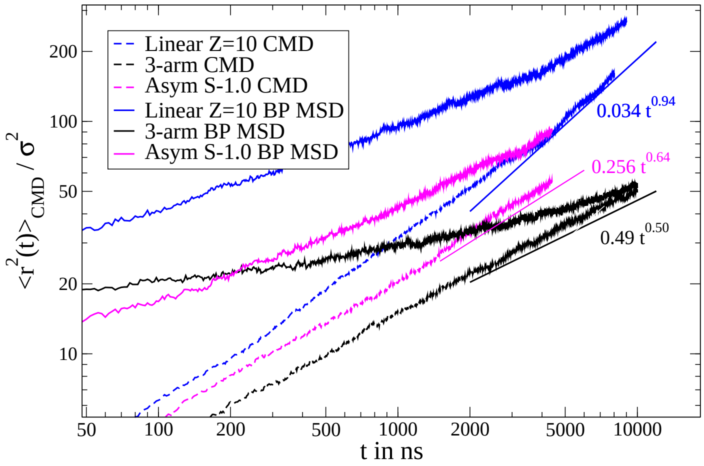

Figure 45: BP Mean Square Displacement and Center of Mass Diffusion of the simulated symmetric 3-arm star and the linear $Z = 10$ chain and the Asym S-1.0 star. 3-arm in black, Asym in magenta and the linear chain ($Z = 10$) in blue. The MSD of the BP is plotted as solid lines and the CMD is plotted as dashed lines. The fitted valus of the exponetns and $6 \cdot D$ for different systems are indicated with a small shift below the data to increase visibility.

6.3.2 *Theoretical description for dynamic structure factor*

The Vilgis and Boué theory that was modified to include the tube survival probability was used as a starting point to describe the behavior of the asymmetric polyethylene stars. For this the theory was adjusted to include the tube survival probability of the asymmetric star that was calculated in Section 5.5. It is the combination of the individual survival probabilities of the two long and the short arms weighted by their arm lengths and can be seen in Figure 24. To use the calculated tube dilution it was once again fitted with a KWW function with the resulting parameters $\tau_K = 5.9 \times 10^3$ and $\beta = 0.385$ which decays faster than the symmetric star. At the time scale of the NSE spectroscopy experiments (400 ns) the relaxation function of the symmetric 3-arm star has reached a value of 0.78, whereas the Asym S-1.0 star already decayed to 0.70.

The description of the asymmetric star with the modified Vilgis and Boué theory is shown in Figure 46. With the solid blue lines, using the same Rouse rate and tube diameter as the small symmetric 3-arm stars and the dashed blue line fitting these two values. The overall trend up to 100 or 200 ns more or less matches the experimental values but it fails at longer times, where the theory does not decay fast enough to describe the measured data. Fitting the two values does not significantly change or improve the results. The tube diameter d has to be lowered by 0.6 Å to adjust for the changed TSP. The change in Rouse rate, which is mainly responsible for the steepness of the decay at early times has to be increased (from $Wl^4 = 4.6 \times 10^4$ Å^{4}ns^{-1} to 5.6×10^4 Å^{4}ns^{-1}) from the 3-arm symmetric star to better match the data. This brings the value closer to the one for the linear chain as it is no longer reasonable to describe the added friction from the very short side arm with the $2/f$ relation as the constraint is less strict as for systems with longer arms.

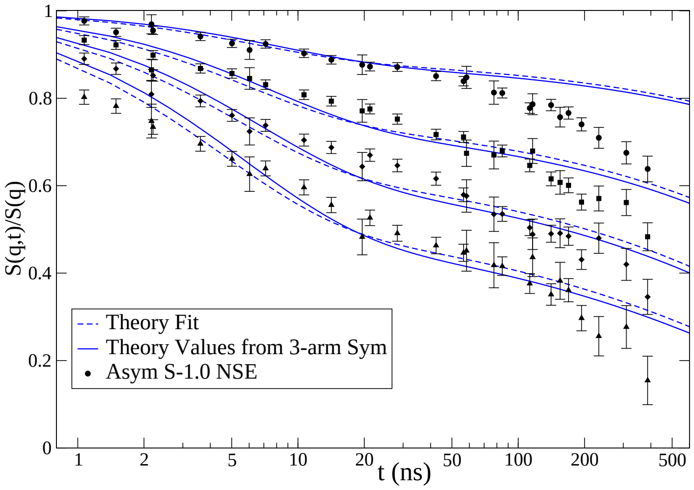

Figure 46: Dynamic structure factor of Asym S-1.0 star (black symbols). Solid blue line: Theory with Rouse rate $Wl^4 = 4.6 \times 10^4$ Å^{4}ns^{-1} and tube diameter $d = 35.4$ Å of 3-arm symmetric. Dashed blue line: Theory with fitted Rouse rate $Wl^4 = 5.6 \times 10^4$ Å^{4}ns^{-1} and $d = 34.8$ Å. The q values are 0.05 Å^{-1}, 0.077 Å^{-1}, 0.096 Å^{-1} and 0.115 Å^{-1} from top to bottom.

To better describe the data the effects of the center of mass diffusion of the polymers were integrated into the modified Vilgis and Boué theory. This sub-diffusive process is described in detail in Section 6.3.1. The CMD for the simulated system was calculated and fitted with $\left\langle r^2(t) \right\rangle = 6Dt^{\kappa}$ to obtain the diffusion exponent κ for the inclusion of the sub-diffusion in the dynamic structure factor

$$S(q,t) = \exp\left(-q^2Dt^{\kappa}\right) \cdot S_{\text{modified V+B}}(q,t). \tag{6.13}$$

The diffusion exponent for the Asym S-1.0 star was found to be 0.578 for times up to 400 ns. The diffusion coefficient D from fitting the simulated CMD was about a factor of four larger than the one obtained by fitting to the experimental $S(q,t)/S(q)$. The values obtained from fitting to the experimental results should nevertheless be sufficient to describe the additional decay of the asymmetric stars.

The effect of simply including the CMD without changing any other parameter is shown in Figure 47. The difference between the blue and the green theoretical curve is as expected significant enough to create a much better description of the strong decay at later times. The matching of theory and experiments worsens for times between 30 and 100 ns, where the theory lies below the data.

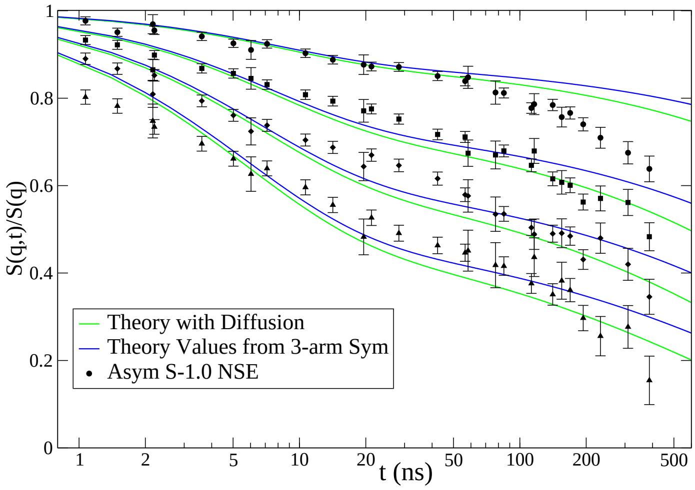

Figure 47: Dynamic structure factor of Asym S-1.0 star (black symbols). Solid green line: Theory (with Rouse rate $Wl^4 = 4.6 \times 10^4\,\text{Å}^4\text{ns}^{-1}$ and tube diameter $d = 35.4\,\text{Å}$) including sub diffusion with a fitted diffusion coefficient of $D = 0.5\,\text{Å}^2\text{ns}^{-1}$. Solid blue line: Theory as before without diffusion.

To obtain a better description of the data with the theory the Rouse rate Wl^4 and the tube diameter d were fitted. This again lets the Rouse rate that is now at $6.0 \times 10^4\,\text{Å}^4\text{ns}^{-1}$ get closer the the one of the linear chain. The tube diameter also reduces slightly by around 1.1 Å. The difference between fitted values and using the values for the symmetric star can be seen in Figure 48, where both are plotted. The match for the fitted theoretical description (solid red line) is significantly better and describes the data with the exception of the lowest q value well. At intermediate times, the theory is slightly lower than the NSE data.

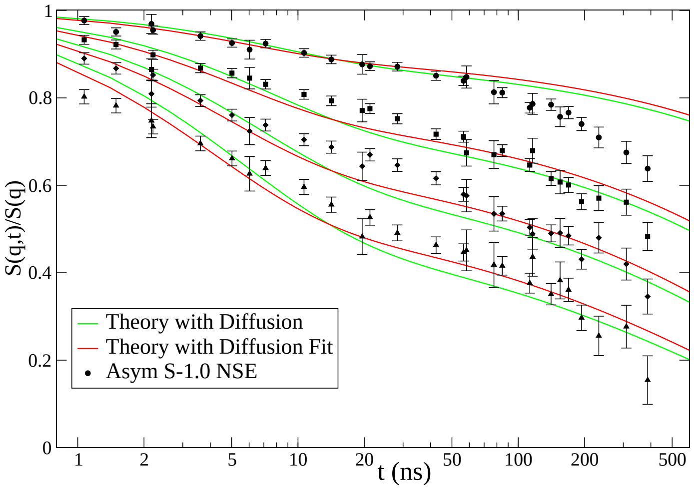

Figure 48: Dynamic structure factor of Asym S-1.0 star (black symbols). Solid green line: Theory with ("old") Rouse rate $Wl^4 = 4.6 \times 10^4$ Å^{4}ns^{-1} and $d = 35.4$ Å and a diffusion coefficient of 0.5 Å^{2}ns^{-1}. Solid red line: Theory with fitted $Wl^4 = 6.0 \times 10^4$ Å^{4}ns^{-1} and fitted $d = 34.3$ Å and a diffusion coefficient of 0.5 Å^{2}ns^{-1}.

As the MD simulations give the possibility to reach much larger times than standard dynamic structure factor measurements with NSE, it is interesting to see if the same theoretical descriptions also work for the simulation results. The Figure 49 shows the NSE data compared to the simulations $S(q,t)/S(q)$ and the modified Vilgis and Boué theory without diffusion (blue dashed line) and with CMD (solid red line) respectively. The observed time window is now between 2 and 2000 ns. The fit with the same variables as the 3-arm symmetric star starts to fail to describe the MD data for times as short as 200 ns.

Now using the theory that incorporates CMD and a fit of the Rouse rate Wl^4 and the tube diameter d, one can see in Figure 49 that at least for times matching the NSE window up to 400 ns the match is still good. Only at longer times the simulation decay quite a bit faster than the theory. The diffusion coefficient was fitted and resulted in 0.5 Å^{2}ns^{-1} as the factor gained from the simulations was a factor of four too large as explained in the earlier section. The real CMD is not constant over time but changes both the diffusion constant D and the diffusion exponent κ over time as has been shown in Section 6.3.1. But this change happens only at later times ($\approx$ 1000 ns for the asymmetric star) than where the theory starts to deviate from the simulation dynamic structure factor.

With the modified Vilgis and Boué theory model with the inclusion of center of mass diffusion it is possible to obtain a theoretical description of the dynamic structure factor for the measured center labeled asymmetric polymer star for the NSE time window. It generally underestimates the mobility of the stars at longer times that are accessible with MD simulations and other

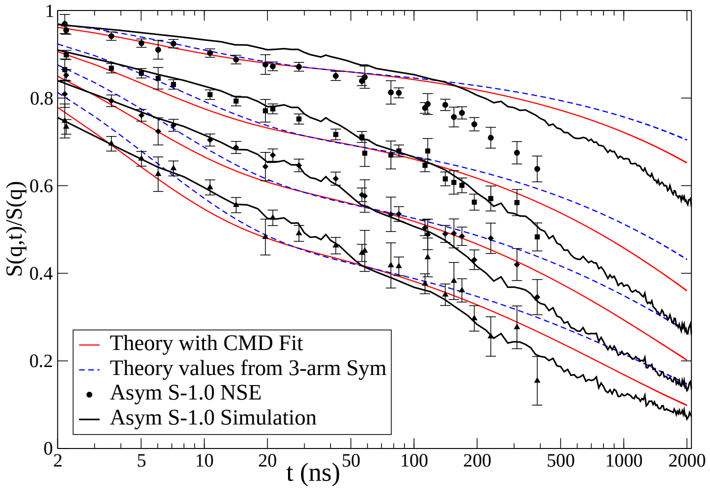

Figure 49: Dynamic structure factor from NSE and MD simulation of Asym S-1.0 star (black symbols and black solid lines). Dashed blue line: Theory with Rouse rate $Wl^4 = 4.6 \times 10^4\,\text{Å}^4\text{ns}^{-1}$ and tube diameter $d = 35.4\,\text{Å}$ of 3-arm symmetric without CMD. Solid red line: Theory with fitted Rouse rate $Wl^4 = 6.0 \times 10^4\,\text{Å}^4\text{ns}^{-1}$ and tube diameter $d = 34.3\,\text{Å}$ and a diffusion coefficient of $0.5\,\text{Å}^2\text{ns}^{-1}$.

alternatives should be considered to describe these type of systems.

One possibility to describe the system would be to split the dynamic process into two time regimes, where the time until the short side arm is fully relaxed can be described by the model of Vilgis and Boué and the later times by the motion of a linear chain. The motion for a linear chain is described by DeGennes [41] or Likhtman *et al.* [36] (which includes contour length fluctuations). This method has the disadvantage that is it designed for fully labeled chains and not for center labeled ones that are the topic of this work. Therefore the the model of Fatkullin and Kimmich will be used in Section 6.3.3 to try to describe the dynamic structure factor of the asymmetric stars.

6.3.3 *Alternative description of scattering data*

A different approach to describe the dynamic structure factor of the asymmetric star would be to divide the process into two different time sections. The first would be for times $t < \tau_{\text{relax}}$, where the short side arm is still not fully relaxed and the polymer more closely resembles its symmetric counterpart in its mobility. During this time frame the same model as for the symmetric system (modified Vilgis and Boué model) with just the replaced function for the tube survival probability would be used. After the relaxation time τ_{relax} of the short side arm the star acts more similar to a linear chain within a tube confinement that allows the movement in the tube direction explaining the increase in mobility after that time window.

A possible way to describe this would be to adapt the theory of Fatkullin and Kimmich [69] that describes the self correlation of segments moving within a tube. So far the observed dynamics was described by using the coherent dynamic structure factor eq. 3.9, but for small label and small enough q this is here not completely true anymore, as one does observe the non-correlated scattering of labeled parts, which is the self-correlation of the label or the incoherent scattering function eq. 3.10.

Fatkullin and Kimmich have calculated the dynamic structure factor for the self-motion along the tube under consideration of non-gaussianity effects. The resulting self-correlation term is therefore

$$S_{\mathrm{FK}}(q, t > \tau_{\mathrm{relax}}) = \exp\left(\frac{q^4 d^2}{216} \cdot \langle r^2(t)\rangle\right) \mathrm{erfc}\left(\frac{q^2 d}{6\sqrt{2}}\sqrt{\frac{\langle r^2(t)\rangle}{3}}\right), \quad (6.14)$$

where "erfc" is the error function and the mean square segment diffusion is

$$\langle r^2(t)\rangle = 2\sqrt{\frac{1}{\pi} W l^4 t}. \quad (6.15)$$

This is only valid for times longer than the entanglement time τ_e (no tube restriction before) but as it is not used up to the relaxation time of the short arm which is much longer, this does not pose a problem. Combining the modified Vilgis and Boué model with the theory of Fatkullin and Kimmich one gets

$$S_{\mathrm{combined}}(q,t) = \begin{cases} S_{\mathrm{modified\ V+B}}(q,t) & \text{for } t < \tau_{\mathrm{relax}} \\ S_{\mathrm{FK}}(q,t) & \text{for } t > \tau_{\mathrm{relax}} \end{cases}. \quad (6.16)$$

To obtain a smooth transition from the modified Vilgis and Boué model to the description of Fatkullin and Kimmich, the self correlation function at times larger then τ_{relax} is renormalized to the value of $S_{\mathrm{modified\ V+B}}$ at τ_{relax}. This modification lifts the values for later times. This method was already applied for the example of center labeled linear chains in Ref. [39]. Applying this theory to the Asym S-1.0 star with the parameters for the symmetric 3-arm star and with the fitted values is shown in the Figures 50.

Once the tube diameter and the Rouse rate are fitted, the match for the NSE results is good. The smallest q shows the already expected mismatch for later times where the experimental data are lower than the theoretical description. In the case of the highest $q = 0.115\,\text{Å}^{-1}$ the theory matches quite well up to a time of around 200 ns, only at longer times the data shows a stronger decay.

Comparing the simulation to the same theory, the findings are similar (see Figure: 51) The match for $q = 0.077\,\text{Å}^{-1}$ is up to the NSE time window still quite good but the lowest theoretical q is too low over the complete time window. For the higher q and times larger than 200 ns the theory does not describe the faster relaxation in the simulation results. An explanation for this mismatch could be the fact that in order to have a continuous transition between the two theories the $S_{\mathrm{FK}}(q,t)$ had to be brought up to higher values to match the $S_{\mathrm{modified\ V+B}}(q,t)$ at the time τ_{relax}. This means that at later times the Fatkullin and Kimmich theory would actually be already much closer to zero and flatten out for that reason. This makes this combination of theories not a very good candidate to describe very long times for the simulation data.

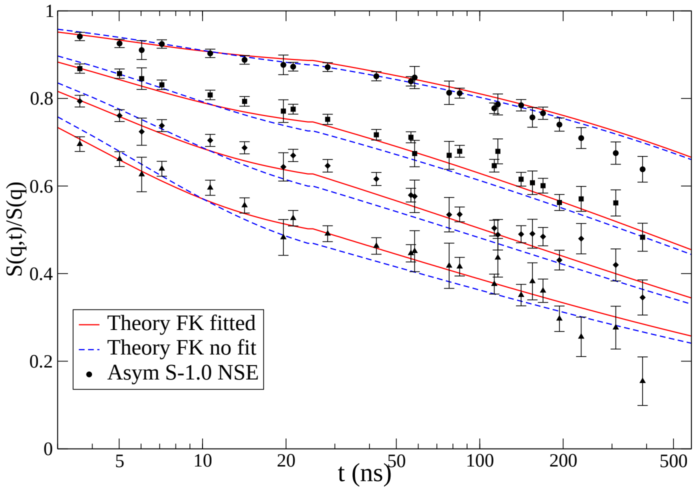

Figure 50: Dynamic structure factor from NSE measurements of Asym S-1.0 star (black symbols). Dashed blue line: Theory with ("old") Rouse rate $Wl^4 = 4.6 \times 10^4\ \text{Å}^4\text{ns}^{-1}$ and $d = 35.4\,\text{Å}$. Solid red line: Theory with fitted $Wl^4 = 6.0 \times 10^4\ \text{Å}^4\text{ns}^{-1}$ and fitted $d = 34.3\,\text{Å}$

Figure 51 also shows the dynamic structure factor including center of mass diffusion

$$S_{\text{combined+CMD}}(q,t) = S_{\text{combined}}(q,t) \cdot \exp\left(-q^2 D t^{\kappa}\right) \tag{6.17}$$

with the same diffusion coefficient and exponent as used in the earlier calculations (green lines). The resulting theoretical description creates a better match for the large q values at long times but completely fails to describe the intermediate time scales and the low q values.

The analysis of the dynamic structure factor and its comparison with MD simulations and theoretical description was more complicated than the one for symmetric star. The matching of simulations and experiments are of good quality and confirm the results from other sections, that the asymmetric stars have a much higher BP mobility than their symmetric counterparts. Many different mechanics such as the center of mass diffusion of the polymers, and diffusion along the tube can play a roll in the dynamics of the branch point. This was tested in this chapter by combining them with the modified Vilgis and Boué model and the theory of Fatkullin and Kimmich. A good description of the NSE time window was achieved using modified V + B together with diffusion but for the longer simulated times further testing has to be done to find a satisfactory theory.

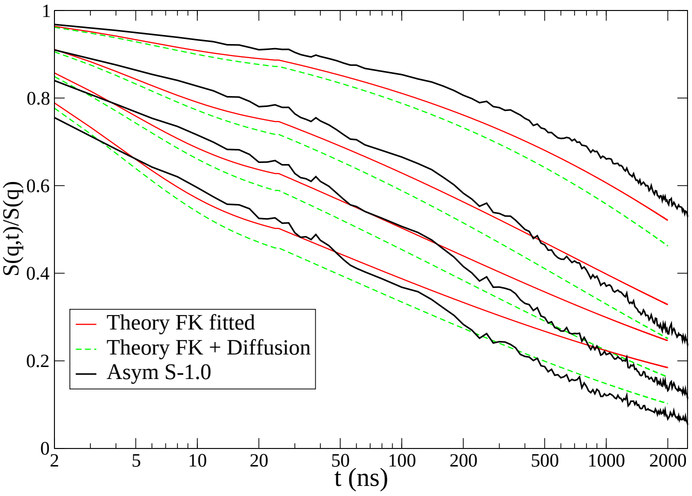

Figure 51: Dynamic structure factor from MD simulations of Asym S-1.0 star (black lines). Solid red line: Theory with fitted $Wl^4 = 6.0 \times 10^4\,\text{Å}^4\text{ns}^{-1}$ and fitted $d = 34.3\,\text{Å}$. Dashed green line: same theory as red but including CMD for asymmetric star.

7

CONCLUSION AND SUMMARY

This work is a systematic study on the influence of arm length, number of arms and asymmetry on the mobility of the branch point in star polymers. To investigate the complex dynamic processes on a molecular length-scale, NSE spectroscopy measurements have been performed. They have been combined with MD simulations, which extend the observable time frame and allow to analyze additional polymer structures. Additional macroscopic characterization by rheology has also been performed. All systems examined showed good agreement between simulations and experimental results. Key insights have been found for some of the following highlighted points.

Branch point confinement and early tube dilution
From the simulated systems the fluctuations of the branch point around its mean position was determined. The early tube dilution, and with it the so-called "diving modes", where the BP can explore the tube of individual arms were found for the 3-arm stars as expected from previous works. This effect was however strongly hindered for stars with number of arms four and larger. The space in which the BP moves is strongly restricted for these functionalities and a much stronger confinement is observed. It was also found, analyzing simulations results for the dynamics of segments along the arms, that the influence of the branch point on the mobility of different segments along the arms has quite a long reach, with an effect still visible for segments up to three entanglements from the BP, however severely reduced and no longer distinguishable by functionality at these distances.

Functionality dependence
The influence of functionality f (3,4 and 5), the number of arms, on the BP dynamics of symmetric stars was studied in simulations and experiments for the first time. The mean square displacement (MSD), the dynamic structure factor and the directly observed mobility (using MD) of the branch point was examined. The main results are, that the increase in functionality creates a signifcantly stronger confinement for the BP. The slow-down of the dynamics follows the theoretical dependence of $2/f$ [40] for the MSD of large stars. As expected, the rheological results showed very small influence of the functionality as they are mainly dependent on the chain and arm lengths of the investigated polymers. The analysis of the MSD from simulations showed that, once early tube dilution and branch point friction are accounted for, there is still a dependence on the functionality. This is revealed in the different time exponents describing the movement of the BP.

Dynamic tube dilution (DTD)
The effect of dynamic tube dilution is shown to be much stronger for smaller, still entangled stars, than for their larger counterparts with similar geometry, both symmetric and asymmetric. This could directly be observed by the

experiments on the polymer flow (rheology) and NSE spectroscopy on BP dynamic as well as MD simulations support this finding. By modifying the model of Vilgis and Boué [16] for cross-linked networks to include DTD and tube parameter renormalization a good description for the dynamic structure factor (from NSE) of the symmetric star polymers was found. The theoretical description only falls short at very long times that far exceed the NSE time window as seen in the MD simulations. One of the driving factors of DTD is the amount of unrelaxed material relating to the tube survival probability, in a polymer system where the DTD is proportional to it. Simulations revealed, that they do show a significant functionality dependence in their MSD but not in their tube survival probability. The failure of the DTD model to describe the branch point relaxation at longer times for higher functionality suggest that the model might need to be adjusted to include a functionality dependence.

Influence of unentangled short side arms

Experiments and simulations on 3-arm asymmetric polymer stars (with unentangled short side arm ($Z_a \leqslant 1$) and long entangled backbone) were analyzed concerning the effect of different short arm lengths and backbone lengths. The following results were found: Short unentangled side arms increase the effective friction of the star scaling quadratically with their arm length. This is consistent with the Rouse theory for tethered arms. The short side arms have to fully relax to allow reptation along the tube. Therefore longer, entangled side arms increase the friction even more. Calculating the hopping parameter p^2 using the current theoretical models fails for unentangled short side arms. Rheological experiments showed, that the actual influence of this parameter is significantly reduced for systems with these type of short side chains. NSE measurements revealed that once the short arm has relaxed, the BP can move along the tube of the longer mildly entangled arm (similar like linear chains) in agreement with Rheology. Finding a theoretical description for the dynamic structure factor of asymmetric star from NSE and simulations showed to be quite challenging. The different theoretical approaches incorporate the subdiffusive center of mass motion for the asymmetric stars, resulted in a good description for the NSE time window. But they all fail to describe the dynamics the long time scales beyond the NSE window that are accessible with MD simulations.

This investigations has found some new and partially unexpected characteristics for the dynamic of branched polymer systems and their branch point. Further research should be done on the following topics to find the needed adjustments for the theoretical models.

- Functionality dependence even when corrected for ETD and friction that is not explained by DTD
- DTD theory most likely needs to incorporate functionality dependence
- Theoretical explanation for hopping parameter p^2 quasi irrelevancy for unentangled side arms of polymers
- No satisfactory model for the dynamic structure factor for asymmetric star polymers at long times yet

The combination of experimental methods and computer simulations has shown to be a great path to investigate these complex polymer systems. Branched polymers show very unique dynamic behavior and are a interesting field of study with various parts that still have to be explored further.

A

APPENDIX A

A.1 RANDOM PHASE APPROXIMATION

Calculating the static structure factor for polymer melts consisting of two polymer types (A and B) which is the equivalent to the experimentally labeled and unlabeled. For these polymers the local density fields $\rho^A(\vec{r})$, $\rho^B(\vec{r})$ and their Fourier transformations are needed. These are given by

$$\rho^A_{\vec{q}} = \sum_{\omega,l\in A} \exp(i\vec{q}\cdot\vec{r}^{\omega}_{l}), \quad \rho^B_{\vec{q}} = \sum_{\omega,l\in B} \exp(i\vec{q}\cdot\vec{r}^{\omega}_{l}). \tag{A.1}$$

The sums are over they individual polymer sorts A and B with l the vector of a segment on the chain ω. If individual chains contain both species (A and B) the two density variables become correlated. If not, they are just sums over large numbers of independent variables and are therefore Gaussian. The density variables $\rho^A_{\vec{q}}$ and $\rho^B_{\vec{q}}$ are distributed as

$$\Phi_0(\rho^A_{\vec{q}},\rho^B_{\vec{q}}) \sim \exp\left[-\frac{1}{2}\sum_{\vec{q}}\left(\rho^A_{-\vec{q}}\rho^B_{-\vec{q}}\right) M^{-1}_{\vec{q}} \begin{pmatrix}\rho^A_{\vec{q}}\\ \rho^B_{\vec{q}}\end{pmatrix}\right]. \tag{A.2}$$

This represents the concentration fluctuations of the density fields and it is related to the entropy of the system. $M_{\vec{q}}$ is the matrix for the correlation functions in absence of interactions

$$M_{\vec{q}} = \begin{pmatrix} S_0^{AA}(q) & S_0^{AB}(q)\\ S_0^{BA}(q) & S_0^{BB}(q)\end{pmatrix}. \tag{A.3}$$

With each matrix element given as (example of AB)

$$S_0^{AB}(q) = \left\langle \rho^A_{\vec{q}}\rho^B_{-\vec{q}}\right\rangle_0 = n_c s_0^{AB}(q) = \left\langle \sum_{l\in A}\sum_{l'\in B} \exp\left(i\vec{q}\cdot(\vec{r}_l - \vec{r}_{l'})\right)\right\rangle_0 . \tag{A.4}$$

n_c giving the total number of chains in the system and the s_0^{XX} the single chain structure factor. Taking constant monomer denisty into account and the static structure factor for a two component chain blend with S_0^{XX} as the correlations functions becomes eq.2.11.

All correlation terms for the f-arm star are listed in Table 13. It also shows the correlation terms for a asymmetric 3-arm star, where two arms are the same length and composed of the protonated part $H\alpha$ and the deuterated part $D\alpha$. The third arm can be of different length with $H\beta$ and $D\beta$ the lengths of

Table 13: S_0 for HH, DD and HD single chain correlation functions.

Correlator	f-arm symmetric star	3-arm asymmetric star
$S_0^{HH} = n_c \cdot$	$f \cdot J_H + f(f-1) \cdot H_H^2$	$2 \cdot J_{H\alpha} + J_{H\beta} + 4 \cdot H_{H\alpha} H_{H\beta}$ $+ 2 \cdot H_{H\alpha}^2$
$S_0^{DD} = n_c \cdot$	$f \cdot J_D + f(f-1) \cdot G_H^2 H_H^2$	$2 \cdot J_{D\alpha} + J_{D\beta} + 2 \cdot G_{H\alpha}^2 H_{D\alpha}^2$ $+ 4 \cdot G_{H\alpha} G_{H\beta} H_{D\alpha} H_{D\beta}$
$S_0^{HD} = n_c \cdot$	$f \cdot H_H H_D (1 + (f-1) \cdot G_H)$	$2 \cdot H_{D\alpha} H_{D\alpha} + 2 \cdot H_{H\alpha} H_{D\alpha} G_{H\alpha}$ $+ 2 \cdot H_{D\alpha} H_{D\beta} G_{D\alpha} + H_{D\beta} H_{H\beta}$ $+ 2 \cdot H_{D\beta} H_{H\alpha} G_{H\beta}$

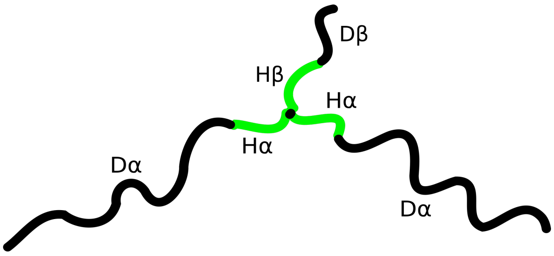

Figure 52: Schematic representation of asymmetric polymer with deuterated parts $D\alpha$ and $D\beta$ in black and protonated parts $H\alpha$ and $H\beta$ in green.

the segments. For better visual presentation the example of the asymmetrical 3-arm star is shown in Figure 52.

To generate these correlators one has to count the number of possible interactions between the different segments. As an example for the 3-arm asymmetric star: There are two "self-terms" for $D\alpha$ as there are two outer deuterated segments in the star ($2 \cdot J$). There are two "coterm" plus "propagator" factors that are needed for the connection between the two $D\alpha$ segments ($2 \cdot G^2 H^2$). There is only one "self-term" for the $D\beta$ segments of the asymmetric arm ($1 \cdot J$). There are four possibilities for "coterm" plus "propagator" between the asymmetric outer segment $D\beta$ and the regular outer segments $D\alpha$ ($4 \cdot GGHH$). This has to be repeated for the corresponding inner segments interactions and the cross term interactions between the labeled inner segments and the non-labeled outer segments. These correlators are put into equation 2.11 to calculate the incompressable static structure factor.

For the calculations the following three expressions [27] are needed

$$G = \exp(-F_\alpha^2) \tag{A.5a}$$

$$H = N_\alpha \frac{1}{F_\alpha^2} \left(1 - \exp(-F_\alpha^2)\right] \tag{A.5b}$$

$$J = N_\alpha^2 j_D(F_\alpha^2). \tag{A.5c}$$

They are called the propagators (G), coterms (H) and self-terms (J) with $F_\alpha^2 = q^2 b^2 N_\alpha / 6$ as the normalized wave vector and $j_D(F_\alpha^2)$ the Debey structure factor $j_D(x) = \frac{2}{x^2}(\exp(-x) - 1 + x)$. Depending on the part of the polymer, α will be H or D for protonated and deuterated polymers. Each of the three terms in eq. A.5 stands for a interaction in a copolymer depending on what part is looked at. As an example a 3-arm symmetric star is used that is labeled with a protonated part around the branch point. The interactions between protonated parts do not need any "connecting" parts so for these correlations only the "propagator" and the "self-term" are needed. For the interactions between the deuterated parts the "self-term" and additionally also the connecting "coterm" is used. For the correlations between the deuterated and protonated elements both the "propagator" (in this case two different ones) and the "coterm" are used without any self-correlations.

BIBLIOGRAPHY

[1] M. Doi and S.F. Edwards. *The Theory of Polymer Dynamics*. International series of monographs on physics. Clarendon Press, 1988. URL: https://books.google.de/books?id=dMzGyWs3GKcC.

[2] T. C. B. McLeish. Tube theory of entangled polymer dynamics. *Advances in Physics*, 51:1379–1527, 2002. doi:10.1080/00018730210153216.

[3] Michael Rubinstein and Ralph H Colby. *Polymer physics*, volume 23. Oxford University Press New York, 2003.

[4] Kurt Kremer and Gary S Grest. Dynamics of entangled linear polymer melts: A molecular-dynamics simulation. *The Journal of Chemical Physics*, 92(8):5057–5086, 1990.

[5] Evelyne Van Ruymbeke, Christian Bailly, Roland Keunings, and D Vlassopoulos. A general methodology to predict the linear rheology of branched polymers. *Macromolecules*, 39(18):6248–6259, 2006.

[6] RG Larson. Combinatorial rheology of branched polymer melts. *Macromolecules*, 34(13):4556–4571, 2001.

[7] Chinmay Das, Nathanael J. Inkson, Daniel J. Read, Mark A. Kelmanson, and Tom C. B. McLeish. Computational linear rheology of general branch-on-branch polymers. *Journal of Rheology*, 50(2):207–234, 2006. URL: http://link.aip.org/link/?JOR/50/207/1, doi:10.1122/1.2167487.

[8] Xue Chen, Chunxia Costeux, and Ronald G Larson. Characterization and prediction of long-chain branching in commercial polyethylenes by a combination of rheology and modeling methods. *Journal of Rheology*, 54(6):1185–1205, 2010.

[9] Daniel J Read. From reactor to rheology in industrial polymers. *Journal of Polymer Science Part B: Polymer Physics*, 53(2):123–141, 2015.

[10] John M Dealy and Ronald G Larson. Structure and rheology of molten polymers. *Hanser, Munich*, pages 30–39, 2006.

[11] Lewis J Fetters, Andrea D Kiss, Dale S Pearson, Gunther F Quack, and F Jerome Vitus. Rheological behavior of star-shaped polymers. *Macromolecules*, 26(4):647–654, 1993.

[12] Alexandros Chremos and Jack F Douglas. Communication: When does a branched polymer become a particle?, 2015.

[13] S T Milner and T. C. B. McLeish. Parameter-Free Theory for Stress Relaxation in Star Polymer Melts. *Macromolecules*, 30:2159–2166, 1997.

[14] S T Milner and T. C. B. McLeish. Arm-length dependence of stress relaxation in star polymer melts. *Macromolecules*, 31(21):7479–7482, 1998.

[15] Amalie L Frischknecht, Scott T Milner, Andrew Pryke, and Ron N Young. Rheology of Three-Arm Asymmetric Star Polymer Melts. *Macromolecules*, 35:4801–4820, 2002.

[16] T.A. Vilgis and F.J. Boué. Brownian motion of chains and crosslinks in a permanently linked network: The dynamic form factor. *Journal of Polymer Science Part B: Polymer Physics*, 26(11):2291–2302, 1988.

[17] G Marrucci. Relaxation by reptation and tube enlargement: A model for polydisperse polymers. *Journal of Polymer Science Part B: Polymer Physics*, 23(1):159–177, 1985.

[18] TCB McLeish. Why, and when, does dynamic tube dilation work for stars? *Journal of Rheology*, 47(1):177–198, 2003.

[19] Stefan Holler, Angel J Moreno, Michaela Zamponi, Petra Bacová, Lutz Willner, Hermis Iatrou, Peter Falus, and Dieter Richter. The role of the functionality in the branch point motion in symmetric star polymers: A combined study by simulations and neutron spin echo. *Macromolecules*, 51(1):242–253, 2018. URL: `https://doi.org/10.1021/acs.macromol.7b01579`, `doi:10.1021/acs.macromol.7b01579`.

[20] Lewis J Fetters, David J Lohse, Scott T Milner, and William W Graessley. Packing length influence in linear polymer melts on the entanglement, critical, and reptation molecular weights. *Macromolecules*, 32(20):6847–6851, 1999.

[21] PG De Gennes. Theory of x-ray scattering by liquid macromolecules with heavy atom labels. *Journal de Physique*, 31(2-3):235–238, 1970.

[22] SF Edwards. The theory of polymer solutions at intermediate concentration. *Proceedings of the Physical Society*, 88(2):265, 1966.

[23] Sergei Panyukov and Yitzhak Rabin. Statistical physics of polymer gels. *Physics Reports*, 269(1-2):1–131, 1996.

[24] Sergei Panyukov and Yitzhak Rabin. Polymer gels: frozen inhomogeneities and density fluctuations. *Macromolecules*, 29(24):7960–7975, 1996.

[25] MG Brereton and TA Vilgis. The random phase approximation for polymer melts with quenched degrees of freedom. *Journal de Physique I*, 2(5):581–598, 1992.

[26] DJ Read. Calculation of scattering from stretched copolymers using the tube model: incorporation of the effect of elastic inhomogeneities. *Macromolecules*, 37(13):5065–5092, 2004.

[27] DJ Read. Mean field theory for phase separation during polycondensation reactions and calculation of structure factors for copolymers of arbitrary architecture. *Macromolecules*, 31(3):899–911, 1998.

[28] Prince E Rouse Jr. A theory of the linear viscoelastic properties of dilute solutions of coiling polymers. *The Journal of Chemical Physics*, 21(7):1272–1280, 1953.

[29] Guy C Berry and Thomas G Fox. The viscosity of polymers and their concentrated solutions. In *Fortschritte der Hochpolymeren-Forschung*, pages 261–357. Springer, 1968.

[30] Ralph H Colby, Lewis J Fetters, and William W Graessley. The melt viscosity-molecular weight relationship for linear polymers. *Macromolecules*, 20(9):2226–2237, 1987.

[31] Michael Rubinstein and Ralph H Colby. Self-consistent theory of polydisperse entangled polymers: Linear viscoelasticity of binary blends. *The Journal of chemical physics*, 89(8):5291–5306, 1988.

[32] Qiang Zhou and Ronald G Larson. Direct calculation of the tube potential confining entangled polymers. *Macromolecules*, 39(19):6737–6743, 2006.

[33] Alexei E Likhtman and Tom CB McLeish. Quantitative theory for linear dynamics of linear entangled polymers. *Macromolecules*, 35(16):6332–6343, 2002.

[34] Masao Doi. Explanation for the 3.4 power law of viscosity of polymeric liquids on the basis of the tube model. *Journal of Polymer Science Part C-Polymer Letters*, 19(5):265–273, 1981.

[35] ST Milner and TCB McLeish. Reptation and contour-length fluctuations in melts of linear polymers. *Physical Review Letters*, 81(3):725, 1998.

[36] A Wischnewski, M Monkenbusch, L Willner, D Richter, AE Likhtman, TCB McLeish, and B Farago. Molecular observation of contour-length fluctuations limiting topological confinement in polymer melts. *Physical review letters*, 88(5):058301, 2002.

[37] Petra Bacova, Laurence G D Hawke, Daniel J Read, and Angel J Moreno. Dynamics of Branched Polymers : A Combined Study by Molecular Dynamics Simulations and Tube Theory. *Macromolecules*, 46:4633–4650, 2013.

[38] Jacob Klein. Dynamics of Entangled Linear, Branched, and Cyclic Polymers. *Macromolecules*, 118(33):105–118, 1986.

[39] Michaela Zamponi, Wim Pyckhout-Hintzen, Andreas Wischnewski, Michael Monkenbusch, Lutz Willner, György Kali, and Dieter Richten. Molecular observation of branch point motion in star polymer melts. *Macromolecules*, 43:518–524, 2010. `doi:10.1021/ma9017185`.

[40] M Warner. The dynamics of particular points on a polymer chain. *Journal of Physics C: Solid State Physics*, 14(33):4985, 1981. URL: `http://stacks.iop.org/0022-3719/14/i=33/a=008`.

[41] PG De Gennes. Coherent scattering by one reptating chain. *Journal de Physique*, 42(5):735–740, 1981.

[42] R Oeser, B Ewen, D Richter, and B Farago. Dynamic fluctuations of crosslinks in a rubber: A neutron-spin-echo study. *Physical Review Letters*, 60(11):1041, 1988.

[43] Masao Doi and SF Edwards. Dynamics of concentrated polymer systems. part 2.—molecular motion under flow. *Journal of the Chemical Society, Faraday Transactions 2: Molecular and Chemical Physics*, 74:1802–1817, 1978.

[44] Pavlos S Stephanou, Chunggi Baig, Georgia Tsolou, Vlasis G Mavrantzas, and Martin Kröger. Quantifying chain reptation in entangled polymer melts: Topological and dynamical mapping of atomistic simulation results onto the tube model. *The Journal of chemical physics*, 132(12):124904, 2010.

[45] Varley F Sears. Neutron scattering lengths and cross sections. *Neutron news*, 3(3):26–37, 1992.

[46] Gordon Leslie Squires. *Introduction to the theory of thermal neutron scattering*. Cambridge university press, 2012.

[47] Crespo and Kreischer. Nmi3, 2012. URL: `http://nmi3.eu/neutron-research/techniques-for-/structural-research/large-scale-structures.html`.

[48] A Radulescu, V Pipich, H Frielinghaus, and M-S Appavou. Kws-2, the high intensity/wide q-range small-angle neutron diffractometer for soft-matter and biology at frm ii. In *Journal of Physics: Conference Series*, volume 351, page 012026. IOP Publishing, 2012.

[49] Reiner Zorn. Inelastic neutron scattering. *Lecture Notes of the JCNS Laboratory Course Neutron Scattering*, page 11, 2017.

[50] Mezei F. *Neutron Spin Echo: Proceedings of a Laue-Langevin Institut Workshop Grenoble, October 15-16, 1979 (Lecture Notes in Physics)*. Springer, 1980.

[51] P. Sunthar. *Polymer Rheology*, pages 171–191. Springer New York, New York, NY, 2010. URL: `https://doi.org/10.1007/978-1-4419-6494-6_8`, `doi:10.1007/978-1-4419-6494-6_8`.

[52] John D Ferry. *Viscoelastic properties of polymers*. John Wiley & Sons, 1980.

[53] Nikos Hadjichristidis, Hermis Iatrou, Stergios Pispas, and Marinos Pitsikalis. Anionic polymerization: high vacuum techniques. *Journal of Polymer Science Part A: Polymer Chemistry*, 38(18):3211–3234, 2000.

[54] Mathias Pütz, Kurt Kremer, and Gary S Grest. What is the entanglement length in a polymer melt? *EPL (Europhysics Letters)*, 49(6):735, 2000.

[55] Rolf Auhl, Ralf Everaers, Gary S Grest, Kurt Kremer, and Steven J Plimpton. Equilibration of long chain polymer melts in computer simulations. *The Journal of chemical physics*, 119(24):12718–12728, 2003.

[56] Berk Hess, Carsten Kutzner, David Van Der Spoel, and Erik Lindahl. Gromacs 4: algorithms for highly efficient, load-balanced, and scalable molecular simulation. *Journal of Chemical Theory and Computation*, 4(3):435–447, 2008.

[57] Petra Bačová, Helen Lentzakis, Daniel J. Read, Angel J. Moreno, Dimitris Vlassopoulos, and Chinmay Das. Branch-point motion in architecturally complex polymers: Estimation of hopping parameters from computer simulations and experiments. *Macromolecules*, 47:3362–3377, 2014. `doi:10.1021/ma5003936`.

[58] Mariapaola Staropoli, Andreas Raba, Claas H Hövelmann, Margarita Krutyeva, Jürgen Allgaier, Marie-Sousai Appavou, Uwe Keiderling, Florian J Stadler, Wim Pyckhout-Hintzen, Andreas Wischnewski, et al. Hydrogen bonding in a reversible comb polymer architecture: A microscopic and macroscopic investigation. *Macromolecules*, 49(15):5692–5703, 2016.

[59] Ludwik Leibler and Henri Benoit. Theory of correlations in partly labelled homopolymer melts. *Polymer*, 22(2):195–201, 1981.

[60] E Straube, V Urban, W Pyckhout-Hintzen, and D Richter. Sans investigations of topological constraints and microscopic deformations in rubber-elastic networks. *Macromolecules*, 27(26):7681–7688, 1994.

[61] L. J. Fetters, D. J. Lohse, and R. H. Colby. *Chain Dimensions and Entanglement Spacings*, pages 447–454. Springer New York, New York, NY, 2007. URL: `https://doi.org/10.1007/978-0-387-69002-5_25`, `doi:10.1007/978-0-387-69002-5_25`.

[62] NJ Inkson, RS Graham, TCB McLeish, DJ Groves, and CM Fernyhough. Viscoelasticity of monodisperse comb polymer melts. *Macromolecules*, 39(12):4217–4227, 2006.

[63] Qiang Zhou and Ronald G Larson. Direct molecular dynamics simulation of branch point motion in asymmetric star polymer melts. *Macromolecules*, 40(9):3443–3449, 2007.

[64] Ralf Everaers, Sathish K. Sukumaran, Gary S. Grest, Carsten Svaneborg, Arvind Sivasubramanian, and Kurt Kremer. Rheology and microscopic topology of entangled polymeric liquids. *Science*, 303(5659):823–826, 2004.

[65] Laurence George Demosthenis Hawke. *Dynamics of branched polymers: motion, scattering and rheology.* University of Leeds, 2013.

[66] D Richter, B Farago, R Butera, LJ Fetters, JS Huang, and Bernd Ewen. On the origins of entanglement constraints. *Macromolecules*, 26(4):795–804, 1993.

[67] Samuel Glasstone. *Textbook of physical chemistry.* Macmillan, 1951.

[68] DS Pearson, G Ver Strate, E Von Meerwall, and FC Schilling. Viscosity and self-diffusion coefficient of linear polyethylene. *Macromolecules*, 20(5):1133–1141, 1987.

[69] Nail Fatkullin and Rainer Kimmich. Theory of field-gradient nmr diffusometry of polymer segment displacements in the tube-reptation model. *Physical Review E*, 52(3):3273, 1995.

B

PUBLICATIONS AND CONFERENCES

B.1 PUBLICATIONS

Stefan Holler, Angel J Moreno, Michaela Zamponi, Petra Bacová, Lutz Willner, Hermis Iatrou, Peter Falus, and Dieter Richter. The role of the functionality in the branch point motion in symmetric star polymers: A combined study by simulations and neutron spin echo. *Macromolecules*, 51(1):242–253, 2018. URL: `https://doi.org/10.1021/acs.macromol.7b01579`, `doi:10.1021/acs.macromol.7b01579`

B.2 CONFERENCE TALKS

Branch-point motion in asymmetric star polymers
Stefan Holler, Angel J Moreno and Michaela Zamponi
SoftComp 2015 in Ancona, Italy, `https://eu-softcomp.net`

MD Simulations of Star Polymers - a look at Branch Point Motion to Investigate Dynamic Tube Dilution and the Role of Functionality
Stefan Holler, Angel J Moreno, Michaela Zamponi, Lutz Willner, Hermins Iatrou, Peter Falus and Dieter Richter
SoftComp 2016 in Ancona, Italy, `https://eu-softcomp.net`

Branch Point Motion in Asymmetric Star Polymers Investigated by Molecular Dynamics Simulations
Stefan Holler, Angel J Moreno Michaela Zamponi and Dieter Richter
DPG Tagung 2016 in Regensburg, Germany, `https://www.dpg-physik.de/veranstaltungen/tagungen/tagung_2016.html`

Looking at Branch Point Motion of Star Polymers using MD Simulations and NSE Spectroscopy
Stefan Holler, Angel J Moreno Michaela Zamponi, Lutz Willner, Hermins Iatrou, Peter Falus and Dieter Richter
SoftComp 2017 in Venice, Italy, `https://eu-softcomp.net`

Looking at Branch Point Motion of Star Polymers using MD Simulations and NSE Spectroscopy
Stefan Holler, Angel J Moreno Michaela Zamponi, Lutz Willner, Hermins Iatrou, Peter Falus and Dieter Richter
8th International Discussion Meeting on Relaxations in Complex Systems 2017 in Wisla, Poland, `http://www.idmrcs8.us.edu.pl/`

B.3 CONFERENCE POSTERS

MD Simulations of Star Polymers - a look at Branch Point Motion to Investigate Dynamic Tube Dilution and the Role of Functionality
Stefan Holler, Angel J Moreno, Michaela Zamponi and Dieter Richter
Workshop: "From Matter to Materials and Life" at Desy 2016 in Hamburg, Germany, `https://indico.desy.de/indico/event/15714/`

MD Simulations of Star Polymers - a look at Branch Point Motion to Investigate Dynamic Tube Dilution and the Role of Functionality
Stefan Holler, Angel J Moreno, Michaela Zamponi and Dieter Richter
4th International Soft Matter Conference 2016 in Grenoble, France, `https://www.ismc2016.org/`